DISSERTATION

submitted to the

COMBINED FACULTY OF NATURAL SCIENCES AND MATHEMATICS

of

HEIDELBERG UNIVERSITY, GERMANY

for the degree of

DOCTOR OF NATURAL SCIENCES

Put forward by

László Varga

born in: Győr, Hungary

Oral examination: 15.07.2021

Proton capture measurements on stored ions for the γ-process nucleosynthesis

Referees:

Apl. Prof. Dr. Yuri A. Litvinov

Priv.-Doz. Dr. Wolfgang Quint

Zusammenfassung

Die Wirkungsquerschnitte von Protoneneinfang-Reaktionen sind extrem wichtige Parameter für die Modellierung explosiver Nukleosynthese, insbesondere für die nur schlecht verstandene Produktion der seltenen p-Kerne. Ermöglicht durch die einzigartigen Bedingungen am Experimentierspeicherring (ESR) bei der GSI, wurde 2009 die sogenannte Protoneneinfang-Kampagne gestartet, deren Fokus auf der Untersuchung von (p, γ)-Reaktionen in heißen, explosiven Sternszenarien liegt.
In dieser Dissertation wird das neueste Experiment der Kampagne, durchgeführt im März 2020, analysiert und im Detail diskutiert. Unter Verwendung eines stabilen, sowie zum ersten Mal auch eines radioaktiven Ionenstrahls, konnten die (p, γ)- und (p, n)-Reaktionsquerschnitte bei 10 MeV/u für die Kerne ^{124}Xe und ^{118}Te erfolgreich gemessen werden.
Zusätzlich wurde ein neuartiges experimentelles Konzept zur Verbesserung der Messsensitivität entwickelt. Mit Hilfe des stabilen ^{124}Xe-Ionenstrahls wird gezeigt, dass die Anwendung dieser neuen Technik Messungen bei maximaler Sensitivität für Protonen-induzierte Reaktionen in inverser Kinematik erlaubt.

Abstract

The cross sections of proton-capture reactions are extremely important to model explosive nucleosynthesis, in particular for the poorly understood production of the rare p-nuclei. Taking advantage of the unique possibilities at the Experimental Storage Ring (ESR) at GSI, the so-called proton-capture campaign has been started in 2009 focusing on the study of (p, γ) reactions for hot, explosive stellar scenarios.
In this thesis, the recent experiment of the campaign, performed in March 2020, is analyzed and discussed in detail. The (p, γ) and (p, n) reaction cross-sections have been successfully measured at 10 MeV/u using a stable ^{124}Xe ion beam and for the first time also using a radioactive ion beam, namely ^{118}Te with 6 days half-life.
In addition, a novel experimental scheme to improve the sensitivity of the method has been developed. Using the stable ^{124}Xe beam it is demonstrated that the application of this new technique enables measurement at maximum sensitivity for proton-induced reactions in inverse kinematics.

"A tehetség a nemzeté, a szorgalom az egyéné."
Károly Takács - Hungarian Olympic champion

Contents

Preface **v**

1 Motivation for capture reaction studies **1**

1.1 Theoretical background 1

1.1.1 Astrophysical reaction rate 1

1.1.2 Statistical model of nuclear reactions 4

1.2 Solar abundances 6

1.3 Synthesis of the vast majority of the stable isotopes 7

1.3.1 The rapid neutron capture process 9

1.3.2 The slow neutron capture process 9

1.4 Synthesis of the neutron-deficient stable isotopes 10

1.4.1 The *p*-nuclei 10

1.4.2 γ-process 11

1.4.3 Rapid proton capture processes 12

1.4.4 ν-process 13

1.4.5 Nucleosynthesis networks 13

1.4.6 Challenges for experiments 16

2 Proton-capture campaign at GSI **19**

2.1 GSI Helmholtzzentrum für Schwerionenforschung 19

2.1.1 Production of highly charged ions - UNILAC 19

2.1.2 Acceleration of highly charged ions - SIS18 20

2.1.3 Transfer of long-lived, easy-access ions to ESR 21

2.1.4 Production of exotic nuclei - FRS 22

2.1.5 The Experimental Storage Ring 23

2.1.6 CRYRING@ESR 26

2.1.7 The upcoming FAIR facility 26

2.2 Experimental method 28

2.2.1 Suitability of the ESR for (p,γ) reaction measurements 29
2.2.2 Identification of the (p,γ) events 29
2.2.3 Measurement at astrophysical energies 32
2.2.4 K-REC normalization technique 33
2.3 Former proton-capture experiments at the ESR 35
2.3.1 The ^{96}Ru experiment 35
2.3.2 The ^{124}Xe experiment 37

3 Ion optical simulations of in-ring reactions 39
3.1 The MOCADI code 39
3.2 Modeling the spatial response of the DSSSD 41
3.2.1 The DSSSD spectra 41
3.2.2 Rutherford scattering 44
3.2.3 Position calibration of the DSSSD 45
3.2.4 Background subtraction 45
3.2.5 The (p,γ) peak 47
3.2.6 The (p,n) peak 48
3.3 The ERASE technique 53
3.3.1 Methodology 53
3.3.2 Requirements on the ERASE design 55
3.3.3 Complete background removal 58

4 Energy calibration and reconstruction of DSSSD events 61
4.1 Event types on the DSSSD 61
4.2 Gain matching 64
4.3 Applicability of an energy threshold for the single-strip events 68
4.4 Extension of the energy reconstruction 70

5 The E127 experiment 75
5.1 Experimental steps 75
5.2 Data acquisition system 77
5.3 Calibration of the HPGe detectors 79
5.3.1 Energy scale calibration 79
5.3.2 Efficiency calibration 80
5.4 Luminosity measurement 83
5.5 Analysis of the DSSSD spectra 86
5.5.1 The ^{124}Xe(p,γ) reaction 86

5.5.2 Test of the ERASE technique 88
5.5.3 The ^{118}Te(p,γ) reaction 92
5.5.4 The (p,n) reaction 94

6 Conclusion and outlook **99**
6.1 Ion identification with the DSSSD 99
6.2 Combined results of the ^{124}Xe(p,x) reactions for E_{CM} = 5.47 - 10.06 MeV 100
6.3 First proton capture measurement on stored radioactive ions 102
6.4 Maximized sensitivity for proton-capture 102
6.5 Outlook: The E127b experiment 103
6.6 Outlook: Nuclear astrophysics studies at CRYRING@ESR 104

Appendix A MOCADI code of ^{124}Xe(p,γ)^{125}Cs reaction **105**

Appendix B Technical drawings of the scraping system **109**

Publications **115**

Bibliography **117**

Preface

Nuclear astrophysics has maybe one of the biggest impact on the evolution of humanity among all other subjects. Almost all the types of the various chemical elements and their isotopes, the building blocks of our body and of the world surrounding us, are synthesized in monumental forges of nature during the life cycle of stars. Without these elements life surely could not exist in such form as we know it. In addition, it never ceases to amaze me, how fine tuned the whole chain of reactions responsible for the nucleosynthesis is. Some astonishing examples are the exact strength of the strong nuclear force [1], [2], [3] and the weak force [4], the mass difference of the two lightest quarks [4], [5], or the existence of the so-called Hoyle state in the carbon-12 nucleus [6]. Science, which attempts to describe the mechanism behind the production of the elements, is the result of a balanced marriage between nuclear physics and astrophysics. Both fields are equally important. Nuclear physics provides the background to trace the possible reactions between nuclei and their reaction rates. And astrophysics fills these reactions with importance by describing stellar and their inherent conditions. Nuclear astrophysics is usually founded on an interplay of theoretical models and experimental results. Some theories are highly uncertain and require experimental constrains. This is the point where the experimental physicists can intervene. The reactions with the highest influence in the models need to be identified and measured, while replicating the astrophysical conditions as precisely as possible. At the forefront of research, this requires continuous improvement of the equipment and experimental techniques in order to investigate yet unreachable nuclear reactions and properties.

One of the biggest experimental challenges nowadays in the realm of nuclear astrophysics is to address reactions on radioactive nuclei. The elements produced in explosive nucleosynthesis can be extremely sensitive to such reactions, as for example the *rp*- or the γ-process [7] which spread deeply into the regions of unstable nuclei far from the valley of stability. However, to perform measurements on radioactive targets with short half-lives is in most cases impossible with the traditional experi-

mental methods. To overcome this challenge, heavy ion storage rings provide a great opportunity. They can accumulate and store ions under well-defined conditions utilizing the excellent vacuum withing the ring and provide high luminosities for the measurements in inverse kinematics by recycling the beam. In addition, when it is coupled to a radioactive ion beam facility the reaction studies can be carried out even on unstable highly-charged heavy ions. This method gives access to nuclei which are hardly possible to prepare in form of a solid target. One of such facility in the world is located in Darmstadt, Germany, namely the GSI Helmholtzzentrum für Schwerionenforschung, where I have accomplished my PhD project.

In the framework of the proton-capture campaign of my team, the ASTRUm group at GSI, the unique feature of the Experimental Storage Ring (ESR) facility at GSI has been employed to address astrophysically relevant reactions. In 2009, as a proof-of-concept experiment, the cross section of ^{96}Ru(p,γ) has been successfully investigated [8]. Later, in 2016 the study of the ^{124}Xe(p,γ) reaction has been performed with decelerated fully-ionized $^{124}Xe^{54+}$ ions [9]. Using a Double Sided Silicon Strip Detector (DSSSD), introduced directly into the Ultra High Vacuum environment of the storage ring, the ^{125}Cs proton-capture reaction products have been successfully detected on the high energy tail of the Gamow-window for hot, explosive scenarios. In March 2020, a further step in the experimental campaign of the ASTRUm group a precision study of the proton-capture has been carried out using a highly-charged radioactive ion beam. The cross section of the ^{118}Te(p,γ)^{119}I and ^{118}Te(p,n)^{118}I reactions were directly measured under nearly background-free conditions by introducing a novel technique. By combining an active ion scraping with an offline energy selection on the detected ions, the sensitivity of the identification for proton-capture products increases dramatically.

This proof-of-principle measurement of the proton-capture on highly charged, radioactive ions in combination with the novel background suppression technique opens the pathway for future experiments to study the radioactive regime of the explosive nucleosynthesis. This is an important step to fully understand the production of the neutron-deficit stable isotopes with the lowest abundances, i.e. the origin of the p-nuclei.

Chapter 1

Motivation for capture reaction studies

1.1 Theoretical background

Before going into detail in regards of the concrete capture reactions that occur in stellar environment, a brief theoretical foundation should be given to the expressions used in the following chapters.

1.1.1 Astrophysical reaction rate

One of the most important concepts in nuclear physics is the cross section. It is a quantitative measure for the probability that during an interaction the reaction of interest will occur.

One can write the number of reactions that happen per unit time when projectile p nuclei with velocity v interact with T target nuclei

$$\frac{N_R}{t} = \frac{N_p/t \cdot N_T}{A_{eff}} \cdot \sigma = L \cdot \sigma \tag{1.1}$$

The N_p/t denotes the number of incoming projectile nuclei per unit time, N_T the number of target nuclei and A_{eff} is the effective geometrical overlap between projectile and target. This equation can be used to be expressed via the luminosity (L), which characterizes the ability of a facility how much of the required collisions it can achieve. In Eq. 1.1 the current per unit area of p can be written as

$$\frac{N_p}{A_{eff} \cdot t} = n_p v \tag{1.2}$$

expressing n_p, the current density of p. With the help of this term the astrophysical reaction rate (r_{pT}), can be expressed [10–13], while taking the average assuming

thermal equilibrium

$$r_{pT} = \frac{1}{1+\delta_{pT}} n_p n_T \langle \sigma(v)\ v \rangle. \tag{1.3}$$

Here, the kronekker-delta symbol δ_{pT} prevents the double counting when p and T are undistinguishable. In a given stellar environment, when massive non-interacting particles move freely, they can be described as an ideal gas. Therefore, the velocity, thus the energy, is defined by the temperature (T) and follows the Maxwell-Boltzmann statistic (ϕ_{MB}), which can be expressed for a single particle as

$$\phi_{MB}^{m_1}(v_1)\ d^3\overrightarrow{v_1} = \Big(\frac{m_1}{2\pi kT}\Big)^{3/2} \exp\Big\{ -\frac{m_1}{2kT}(v_{1x}^2 + v_{1y}^2 + v_{1z}^2)\Big\}\ dv_{1x} dv_{1y} dv_{1z}. \tag{1.4}$$

Here, m_1 is the mass of the particle, $\overrightarrow{v_1}$ is its velocity vector with components v_{1x}, v_{1y}, v_{1z} and k is the Boltzmann constant. The averaged term from Eq. 1.3 for two interacting particles in the stellar plasma can be expressed with the general variables of the center of mass system such as the relative velocity $\overrightarrow{v}$ between the interacting particles and reduced mass $\mu = \frac{m_1 m_2}{m_1+m_2}$

$$\langle \sigma(v)\ v \rangle = \int_0^\infty \phi_{MB}^{\mu}(v)\sigma(v) v\ d^3\overrightarrow{v} = 4\pi \int_0^\infty v^2 \phi_{MB}^{\mu}(v)\sigma(v) v\ dv. \tag{1.5}$$

Eq. 1.5 can be further simplified by introducing an infinitesimal phase-space volume of the relative velocity as $d^3\overrightarrow{v} = 4\pi v^2 dv$. However, during experiments and the calculations it is more favorable to express the equations in terms of the central-mass-energy instead of the relative velocity. This can be, however, trivially done by writing the kinetic energy relation $E = \frac{1}{2}\mu v^2$ and its derivative $v dv = \frac{1}{\mu} dE$ into Eq. 1.5

$$\langle \sigma(v)\ v \rangle = \Big(\frac{8}{\pi\mu}\Big)^{1/2} \frac{1}{(kT)^{3/2}} \int_0^\infty E\ \exp(-E/kT)\sigma(E)\ dE \quad [14] \tag{1.6}$$

The quantity $\langle \sigma(v)\ v \rangle$ is called the stellar reactivity. Inside the integral the $E\exp(-E/kT)$ factor refers to the energy distribution of the particles at a given stellar temperature obeying the Maxwell-Boltmann statistic. In case of photons for example, the energy distribution of the particles would be according to the Planck-statistic. The other factor in the integral is the reaction cross section ($\sigma(E)$). It is important to highlight that the cross section is a stellar quantity. Differently from a general laboratory measurement scenario, the nuclear excited states can be thermally populated, contributing to the effective cross section of the reaction. This stellar effect is discussed in Chapter 1.4.6.

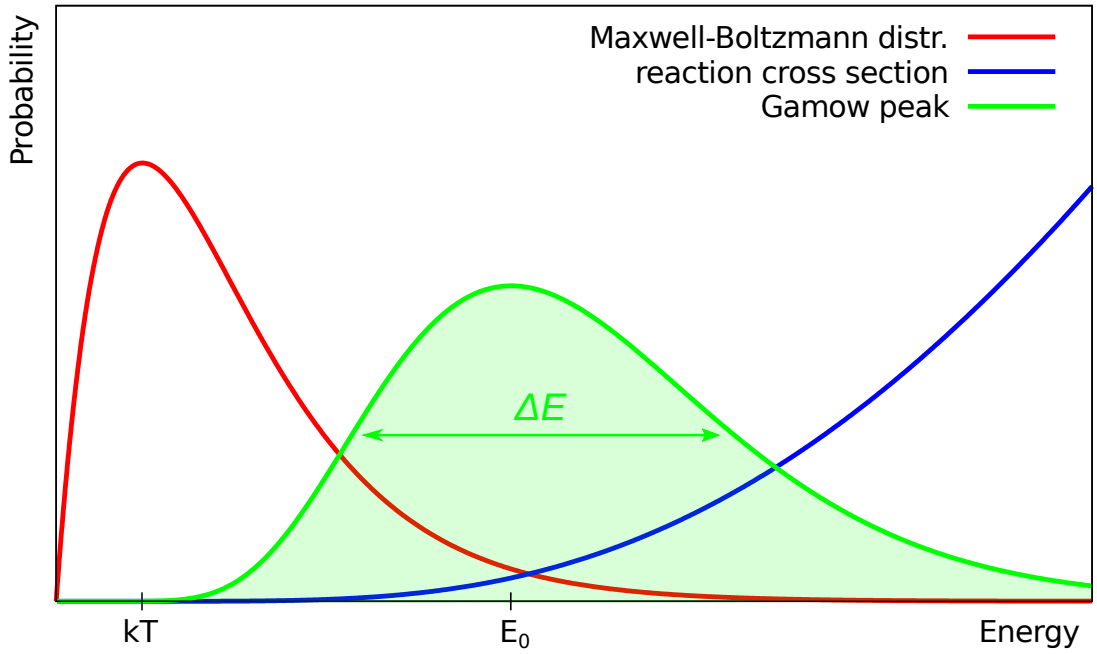

Figure 1.1: The energy range, for which the integral in the definition of the stellar reaction rate (Eq. 1.6) gives the largest contribution, is called the Gamow-window. The peak-shape is the result of the multiplication of two, typically counteracting tendencies, the energy-distribution of the particles in the stellar plasma at a certain temperature and the reaction cross section. This example shows the case of charged particles, when the energy distribution of the particles follows Maxwell-Boltzmann statistic and the cross section in this region is dominated by the quantum-tunneling through the Coulomb barrier.

The limits of the integral in Eq. 1.6 go from $E = 0$ to $E = +\infty$. However, the major contribution comes from the area where the product of $\phi(E) \cdot \sigma(E)$ has maximum, referred to as the Gamow-peak. The region around the Gamow-peak, where the reaction cross section is important to know, is called the Gamow-window [15], see Figure 1.1. In case of charged particles the reaction cross section at low energies is dominated by the height of the Coulomb barrier. The penetrability of the Coulomb barrier can be written as

$$penetrability = \exp(-bE^{-1/2}) \quad [10] \tag{1.7}$$

where $b = \frac{\pi e^2}{\hbar}(2\mu)^{1/2}\ z_1 z_2$, z_1 and z_2 are the charges of the interacting particles, e denotes the electron charge and $\hbar = \frac{h}{2\pi}$ is the Planck constant. By using Eq. 1.7 a relation can be given between the cross section and the astrophysical S-factor

$$\sigma(E) = \frac{1}{E}\exp(-bE^{-1/2})\ S(E). \tag{1.8}$$

The E^{-1} term in Eq. 1.8 represents the general energy dependency of the cross section and the exponent describes the penetration through the Coulomb-barrier. The remaining $S(E)$ quantity accounts for the purely nuclear cross section of the reaction. The cross sections are typically measured at higher energies and then the S-factor is useful to extrapolate measured cross sections to lower energy regime relevant for the astrophysical processes.

1.1.2 Statistical model of nuclear reactions

As shown in the preceding section, to determine stellar reaction rates the cross section of the reaction of interest is required at the energies of astrophysical relevance, see Eq. 1.3 and Eq. 1.6. The theory of reaction mechanism differentiates two main categories. In case of direct reactions the initial and final states of the reaction are directly connected, the time scale of the process is of the order of 10^{-22} s. In case of resonant reactions, first a compound system is formed between target and projectile which than decays into a certain reaction channel. The timescale of resonant reactions is $\sim 10^{-18}$ s or more.
For medium- and heavy-mass nuclei at astrophysical energies the compound mechanism mostly dominates. The corresponding energy windows include compound nucleus (CN) excitation energies with such high nuclear level densities (NLD) that the individual resonances cannot be separated, the average resonance width becomes larger than the average level spacing, i.e. $\langle\Gamma\rangle > 1/\rho$. Instead of taking into account a large number of unknown resonances, a statistical approach can be carried out using averaged resonance properties.
Motivated by the vast difference between the time scales of direct and compound reactions, the statistical model of the compound reactions was first developed by Bohr, generally referred as factorization or independence hypothesis [16]. The model implies that the projectile forms a compound system with the target nucleus, shares its energy among all nucleons, and finally the compound nucleus decays independently of the formation of the compound nucleus. Therefore, the reaction cross section can be factorized into two terms

$$\sigma_{HF}^{Aa\to Bb} = \sigma_{form}^{Aa}\beta_{dec} = \sigma_{form}^{Aa}\frac{\langle\Gamma^{Bb}\rangle}{\langle\Gamma_{tot}\rangle} = \sigma_{form}^{Aa}\frac{\hat{T}^{Bb}}{\hat{T}_{tot}} \tag{1.9}$$

where, σ_{form}^{Aa} denotes the cross section of the formation and β_{dec} is the branching ratio, which expresses the probability for decay to the observed channel Bb. The

branching ratio can be expressed by averaged resonance widths or, by employing the $\hat{T}^{Bb} = 2\pi\langle\hat{\Gamma}^{Bb}\rangle$ relation, also with the so-called transmission coefficients.
Two applications of Eq. 1.9 are widely used. In the Weisskopf-Ewing model [17], only energy, charge and mass conservations are taken into account, while the Hauser-Feshbach model [18] incorporates the conservation of angular momentum and parity as well. Employing the Hauser-Feshbach (HF) formalism, the HF cross section of the A^{μ}(a,b)B reaction can be expressed as

$$\sigma^{\mu}_{HF} = \frac{\pi}{k^2_{\mu}} \frac{1+\delta_{Aa}}{g_{\mu} g_a} \sum_{J,\pi} g_J \frac{T^{\mu}_J \hat{T}^{Bb}_J}{\sum_c \hat{T}^c_J} W^{Aa \to Bb}. \tag{1.10}$$

Here, index μ marks the initial state in the target nucleus A, k_{μ} is the wave number, g denotes statistical factors. While T^{μ} transmission coefficient only describes the transition from states at the compound energy into state μ in the target nucleus, $\hat{T}$ includes all transitions allowed by energetics and quantum selection rules. $\hat{T}_{tot} = \sum_c \hat{T}^c_J$ is the total decay transmission coefficient, which sums over all possible decay channels c leading to the same compound nucleus including $A + a$ and $B + b$. The quantities $W^{Aa \to Bb}$ are the width fluctuation coefficients, which describe non-statistical correlations between the widths in the channels $A+a$ and $B+b$. However, other than in the vicinity of channel openings these coefficients can be well approximated as unity [19, 20].
The transmission coefficients are dependent on the energy, parity and spin of the state μ in the target nucleus and the populated state in the compound system

$$T^{\mu} = T^{\mu}(E^{\mu}, J^{\mu}, \pi^{\mu}, E, J, \pi). \tag{1.11}$$

Reaction cross sections can be calculated by using various HF codes, such as TALYS [21], NON-SMOKER [22], SMARAGD [23]. The statistical models implemented in the codes require the input of a number of different nuclear properties. Such properties are, for instance, optical model potentials describing the interactions between particles and nuclei (eg. proton-width, neutron-width), the masses of all nuclei involved in the reaction, γ-strength function describing the interaction with photons, discrete state information and nuclear level densities, properties of ground and excited states (spin, parity, excitation energy of low-lying discrete levels), etc. The determination of these parameters are often only theoretically possible especially far from stability due to the challenging requirements for the corresponding experiments. An overview on the main difficulties is given in Chapter 1.4.6.
Nevertheless, the input parameters of the nuclear models are not equally important

to determine the cross sections. Sensitivity study of a given HF cross section can reveal the most important parameters for a certain energy range. The sensitivity $\tilde{s}$ is often defined as a measure of a change in the cross section $f_\sigma = \sigma_{new}/\sigma_{old}$ as the result of a change in the transmission coefficient by the factor $f_\omega = T'/T$ [24]

$$\tilde{s} = \begin{cases} \frac{f_\sigma - 1}{f_\omega - 1} & \text{if } f_\sigma > 1,\ f_\omega > 1 \text{ or } f_\sigma < 1,\ f_\omega < 1 \\ \frac{1 - f_\sigma}{(f_\omega - 1) f_\sigma} & \text{if } f_\sigma > 1,\ f_\omega < 1 \text{ or } f_\sigma < 1,\ f_\omega > 1 \end{cases} \tag{1.12}$$

In this expression, $\tilde{s} = 0$ when no change occurs meaning that a change of T does not influence the cross section and $\tilde{s} = 1$, when the cross section changes by the same factor as the transmission coefficient.

1.2 Solar abundances

The isotopical abundance in the solar system is remarkably diverse. This is not so surprising if we consider various nucleosynthesis mechanisms and astrophysical sites responsible for the creation of these elements. On Figure 1.2 the relative solar abundances normalized to 10^6 Si atoms are shown. The observed solar abundances provide hints for the stellar history as well as for the entire Galactical chemical evolution.

The dataset, presented in Figure 1.2 is the result of presolar grain (meteorite) investigations combined with photospheric data [25]. The meteorite samples originate only from four CI Chondrite meteorite falls. These CI Chondrites are a special type of meteorites. The chondrite parent bodies are accumulated from solar nebular condensates, which then later undergo mineralogical alterations by thermal metamorphism and also by aqueous alteration. Nevertheless, this alteration happens within a closed chemical system preserving the overall relative elemental abundances [25]. The solar elemental abundances are obtained from spectroscopic investigations of the Sun photosphere. One should note, however, that the precision differs vastly for the different abundance values within the dataset. Many data are updated recently, some elements were investigated 30 years ago, and for other elements no photospheric investigation exists due to the lack of observable spectral lines. Some elemental abundance are derived from solar helioseizmology (like He) or from coronal sources (Ne, Ar) such as solar winds or solar flares. The abundances obtained from meteorite samples and from solar photospheric line investigations are in agreement within 15% for most of the elements.

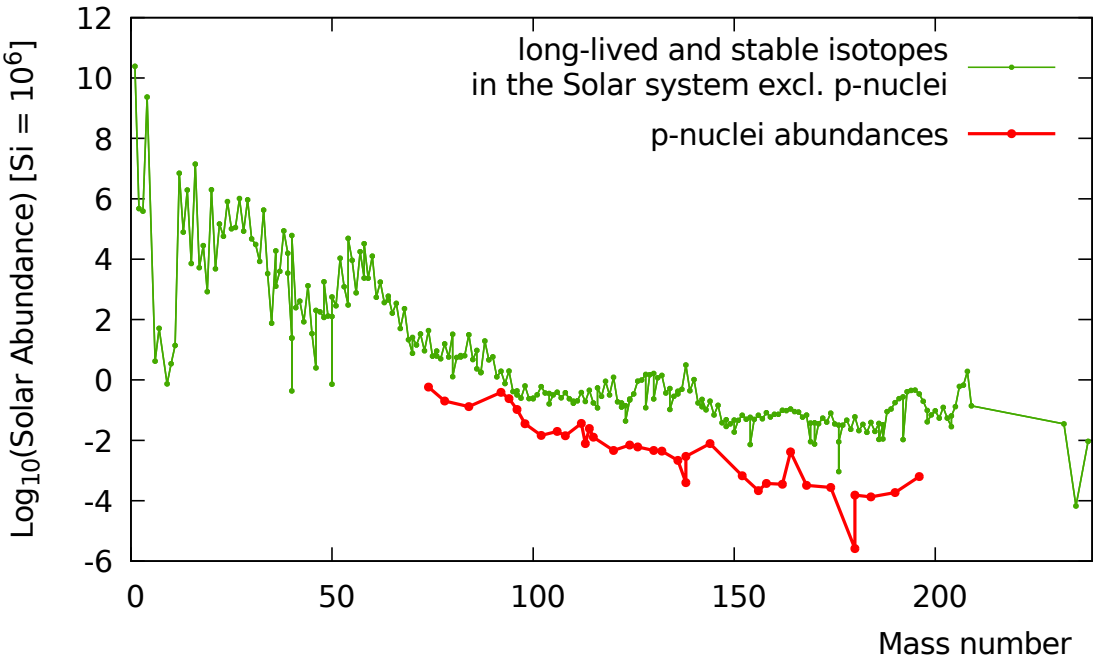

Figure 1.2: The isotopical abundance in the Solar system is remarkably diverse. Many processes contribute in various astrophysical sites leaving their footprints on the abundance vs. mass number plot. After the iron region ($A \gtrsim 56$) the vast majority of the isotopes are produced through neutron-capture based nucleosynthesis. However, roughly 35 nuclei with low abundances are shielded from such nucleosynthesis processes. These are the so called p-nuclei. p-process is the collective term for various mechanisms responsible for p-nuclei creation. The dataset is taken from [25].

1.3 Synthesis of the vast majority of the stable isotopes

The description of the exact abundances of the chemical elements including their isotopes is one of the most important tasks of nuclear astrophysics. Nuclear properties shape the abundance curve, see Figure 1.2, which can be seen for example on the sawtooth shape of the curve caused by the pairing correlations in nuclei, or on the high abundance peak in the iron region indicating the maximal nuclear binding energies per nucleon, or on the s- and r-process peaks reflecting neutron shell closures. The first few, lightest elements have been created directly in the Big Bang nucleosynthesis [26], see Figure 1.3. Then the synthesis of the elements up to the iron cluster is the result of consecutive fusion of the primordial seed nuclei establishing an onion layer structure inside massive stars [27]. The abundances of these elements are decreasing with increasing mass number implying the effect of the rising Coulomb

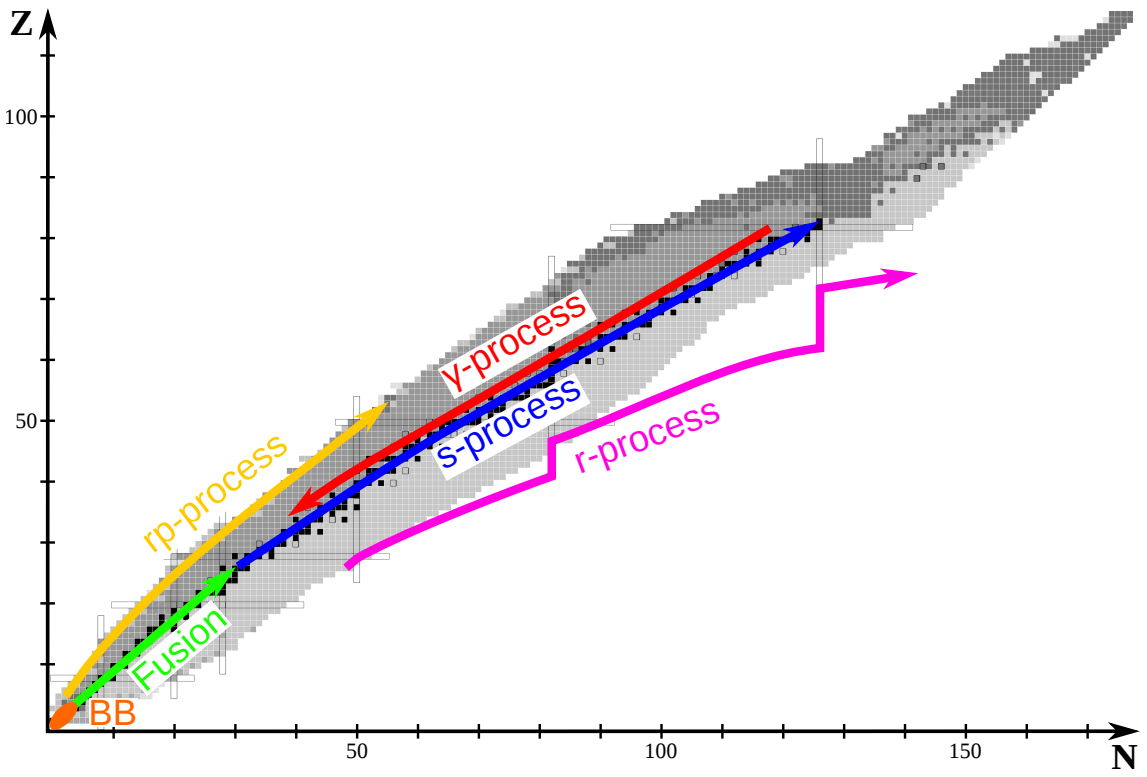

Figure 1.3: Pathways of different nucleosynthesis processes are schematically visualized on the nuclear chart. The two main processes responsible for p-nuclei creation are the rp- and the γ-processes. The rp-process is a fast sequence of (p,γ) reactions and β^+ decays building up the isotopes until its termination in a closed SnSbTe cycle. On the contrary, the reaction path of the γ-process points to the opposite direction, it consists of photo-disintegrations of previously produced heavy seed nuclei, mainly (γ,n), (γ,p) and (γ,α) reactions. The half lives of the isotopes on the nuclear chart are according to the [30] database, black and framed squares = stable and long-lived nuclei, gray squares = nuclei with known half-life. The process paths are illustrated in [31].

repulsion between the heavier nuclei.

After reaching the maximum binding energy per nucleon in the Fe-Ni region, see Figure 1.2, the fusion of the charged nuclei consumes energy instead of generating it. The production of the heavy elements beyond the iron region is dominated by neutron-capture nucleosynthesis processes [27–29]. The double-peak structures around the neutron magic numbers in the solar abundance distribution indicate two main, distinct production mechanisms. These are the slow neutron capture process (s-process) and the rapid neutron capture process (r-process) [27].

1.3.1 The rapid neutron capture process

The rapid neutron-capture process accounts for the 50% of the heavy elements up to bismuth and all of thorium and uranium [32], and in general responsible for the creation of the most neutron-rich isotopes of the trans-iron elements. It is a primary process producing 27 so-called r-only nuclei exclusively [14].
The term *rapid* refers to the rate of the neutron-capture, its time scale believed to be in order of seconds. Between two captures there is no time before to undergo radioactive decay. This leads to a rapid reaction sequence, which can, depending on the exact conditions, get in the vicinity of the neutron dripline, the limit for bound, neutron-rich nuclei. The path of the r-process is strongly influenced by the shell structure of involved nuclei, leading to so-called waiting points at the neutron magic numbers. The resulting abundance peaks near at mass number 82, 130 and 196, see Figure 1.2, are caused by β^- decays along isobaric chains back to stability of matter accumulation at waiting points [27].
The possible astrophysical sites for the r-process must have intense free neutron densities suggesting explosive scenarios. Such locations are currently still actively researched [33], but the traditionally associated site is a core collapse supernova [27]. The recent gravitational wave detection of two merging neutron stars [34] subsequently followed by the detection of the signatures of freshly created n-capture elements in the spectra of the emerged kilonova [35], [36] shows that the neutron-star mergers are a major r-process site. This scenario was hypothesized already in existing theoretical models [37–39]. Nonetheless, it is not yet known whether the r-process abundances in the solar system can be associated to only one or multiple astrophysical sites.

1.3.2 The slow neutron capture process

Contrary to the r-process, the slow neutron capture process does not require explosive scenarios to proceed. However, the s-process is a secondary process seeded by iron nuclei left from a previous generation of stars. In the s-process a seed nucleus captures a neutron. If the newly created isotope is stable then the neutron capture sequence continues forming the heavier isotope of the same element. But if the newly formed isotope is radioactive, a competition arises between beta decay and neutron capture resulting to branching points. However, the timescales of the neutron capture are about 0.1 to 10 years depending on the exact site conditions keeping the reaction path wander close to the valley of stability [27]. The complete evolution of

the s-process requires time scales in the range of thousands of years. The termination point of the s-process is the heaviest quasi stable nucleus, ^{209}Bi. After its next n-capture the resulting nucleus decays back via alpha emission creating an end cycle to the process.
The s-process is one of the most studied nucleosynthesis mechanism. The majority of the n-captures proceeds on stable target nuclei, thereby, many of these reactions could already be accessed in the laboratory. Nowadays the so-called branch points of the s-process are in focus which involve measurements on unstable nuclei.
The s-process can be divided into two sections. The main s-process appears in the helium burning shell of asymptotic giant branch (AGB) stars [40]. It relies on the ^{13}C(α,n)^{16}O reaction as neutron source producing the heavy elements beyond Sr and Y. However, the process alone cannot reproduce the abundances for mass numbers below 90, a complementary *weak* s-process component is required as well. The *weak* s-process acts in massive stars ($M > 8M\odot$) and synthesizes the elements between iron and strontium. The process is driven by the neutrons primarily from the ^{22}Ne(α,n)^{25}Mg reaction at the end of the convective He-core burning and in the subsequent convective C-shell burning [41].

1.4 Synthesis of the neutron-deficient stable isotopes

1.4.1 The p-nuclei

The neutron-capture processes are not able to produce all existing stable isotopes [27, 28]. There are around 35 so-called p-nuclei, stable isotopes from ^{74}Se to ^{196}Hg on the neutron-deficient side of the valley of stability which are bypassed by neutron capture mechanisms. They are the least abundant stable nuclei in nature, about a factor 10-1000 less as compared to other stable isotopes of the same element [29].
The exact list of p-nuclei is still under active discussion, contributions from other processes in case of a few isotopes cannot be completely excluded, as the s-process contribution for ^{152}Gd, ^{164}Er [42], or the r-process contribution for ^{113}In, ^{115}Sn [43].
Historically, the p-nuclei were also called excluded isotopes, since they are shielded from neutron-capture processes by other stable or unstable nuclei from r- or s-process. To create p-nuclei, new mechanisms had to be introduced, bundled under the generic name p-process. A straightforward approach for the p-process could be a sequence of proton captures on a heavy seed nuclei as it was originally suggested in [27], [28], and

in [44]. While one could identify scenarios with the right seed distribution, e.g. from a prior *s*-process, it turned out, that such charged particle reactions cannot be realized efficiently in such scenarios [45] especially on heavy nuclei due to their large Coulomb barrier. A higher temperature environment alone can also not help to increase the proton content of the seed nuclei since photodisintegration starts to compete with fusion removing protons faster from the nucleus than they can be captured.

1.4.2 γ-process

Photodisintegration of a preexisting heavy seed distribution, or shortly the γ-process, is responsible for synthesizing the heavy *p*-nuclei ($A >\sim 100$). The astrophysical sites for this reaction need a hot photon environment with temperatures reaching 2-3 GK. Such environment can arise in the shock front of a Type II super novae (SN) explosion for about a second [46,47] or in the deflagration flame of a Type Ia SN detonation [48]. Pre-explosive scenarios, like the O-Ne burning zone of massive stars, are also proposed to be plausible sites for the γ-process [49,50]. In addition, supercritical accretion disks associated with jets in SN explosion provide an interesting prospect to accommodate the γ-process [51].

Considering the success of the galactical chemical evolution studies in the last 10 years it became clear that beside the Type II supernovae the most promising site for the γ-process to appear is the Type Ia thermonuclear supernovae. However, historically the type II supernovae explosions are the best studied scenario [44] and will be introduce in the following as a showcase for the γ-process. Along the shock wave of the type II SN explosion, the temperature and density of different shells rises swiftly in the onion-structured pre-SN star, resulting to peak temperatures between $1.7 < T_9 < 3.3$ in its Ne/O layer [52]. The seed isotope, synthesized priorly, is likely to be destroyed by a sequence of photodisintegrations, namely in (γ,n) reactions, thereby shifting the distribution of the seed abundances to the neutron-deficient side of the stable isotopes. For higher plasma temperatures the shift is more prominent, the (γ,n) reactions penetrate further into the radioactive nuclides [46, 53]. Nevertheless, photoinduced neutron emission loses its effectiveness while moving away from the valley of stability. Not counting the strong odd-even staggering for neutron emission, the neutron separation energy increases on average when the nucleus becomes more neutron-deficient. When the (γ, n) reaction eventually becomes inferior to the competing (γ, α), (γ, p) reactions, the reaction chain reaches a deflection point. Thereby, the reaction flow is deflected towards lower atomic numbers. For higher mass numbers ($N \gtrsim 82$), (γ, α) deflection points are predominant, while for the lower mass regions

the (γ, p) deflections dominate due to reaction Q-values and Coulomb-barriers [53]. If the two competing reaction rates are comparable, the deflection points can be labeled as branching points, analogously as in the *s*-process. The reaction path is also significantly influenced by the nuclear properties such as shell closures. Once the shock front passes the Ne/O layers, temperature and density drop exponentially and the reaction flux runs dry. Nevertheless, if the temperature and density conditions are maintained long enough, the γ-process path can eventually terminate in the iron peak region.

1.4.3 Rapid proton capture processes

Although the high Coulomb-barrier limits the mechanism of proton-capture on heavy nuclei significantly, as mentioned in Chapter 1.3.2, the reaction might contribute to some extent to the creation of the lightest *p*-nuclei. When the proton densities are high enough in the stellar plasma, 10^{28} protons/cm^3 with associated temperatures of $\sim$2 GK, a rapid sequence of *p*-capture can be realized orders of magnitudes faster than β-decays [54]. This process is called the rapid proton capture process or shortly *rp*-process.

The reaction path follows a series of fast (p, γ) reactions until no further capture is possible either because the proton dripline is reached or because of photodisintegration. When this happens the reaction flow arrives at a so-called "waiting point" and it has to wait until the relatively slow β^+-decay sets in. The life-times at the waiting points along the reaction path define the characteristic time for the whole process. The *rp*-process likely terminates in a closed SnSbTe cycle preventing the synthesis of elements heavier than Te. The reaction path runs into an α-decaying region of the nuclear chart and loops back into itself [55]. A possible site for the *rp*-process is the surface of a neutron star in a binary system, where thermonuclear burning of hydrogen accreted from a less evolved companion star at highly degenerate conditions is realized accompanied by a thermonuclear runaway known as Type I Xray burst [56–62].

It is important to highlight that the *rp*-process has many variants complemented with mainly neutron captures, depending on the conditions present for the reactions. One of such variants is the so called *proton-poor rp*-process or (α, p) process. In this case the temperature is higher than 3GK and proton concentrations is much lower than in the conventional *rp*-process [63].

Another interesting variant is the so called *proton-poor neutron-boosted rp*-process [64]. To bypass the waiting points (n,p) reactions provide a faster alternative than the

β^+-decay. Thereby, the time required for the *rp*-process to complete can be reduced significantly, to the order of seconds. [44]. The reaction path lies much further away from the proton-drip line than in the classical *rp*-process. The process can happen if the free neutron density reaches $N_n \sim 10^{19}\,cm^{-3}$. Co-acting processes can help to obtain free neutrons to accelerate the proton captures. This can happen for example when a massive $\bar{\nu}$ flux occurs in a supernovae which converts protons into neutrons and positrons by $\bar{\nu}$-captures. This co-acting mechanism is called the νp-process [65] and contributes to the creation of several light *p*-nuclei including ^{92,94}Mo and ^{96,98}Ru. Despite the various types of the *rp*-process are able to synthesize low-mass elements, it is still not yet completely understood which mechanism can release the reaction products into the interstellar medium. Thereby, the contribution of the *rp*-process to the solar abundances is still under discussion.

1.4.4 ν-process

In this section, an exotic nucleosynthesis process will be introduced which can be assigned to the two most rarest isotopes in nature, ^{138}La and ^{180}Ta. Both are *p*-nuclei, however, neither the γ-process nor the *rp*-process can be associated with their synthesis, but the ν-process [66]. When the core of a massive star collapses into a neutron star, the outcoming neutrino flux reaches such levels, that despite the small cross section, a significant degree of nuclear transmutations is initiated. Neutrinos excite heavy elements leading to the release of single neutrons, protons or alpha-particles. This emission of particles and their inverse reactions significantly modify nucleosynthesis network calculations. As an outcome, the abundance of many rare isotopes including many odd-Z nuclei are boosted. ^{138}La and ^{180}Ta are created when the neutrino burst from the SN explosion in a massive star reaches the Ne shell of the pre-SN star.

1.4.5 Nucleosynthesis networks

For the near future it remains impossible to establish experimental conditions on Earth to reproduce on a large scale the isotope production in a core collapse supernova or in a type I Xray burst. The only remaining option to study such extreme astrophysical scenarios is to create computer simulations for an entire reaction network, see Figure 1.4. In case of the γ-process taking place in type II SN explosions, multilayer treatment of the stellar interior needs to be employed to reproduce either only a specific layer [29] or the entire volume of the supernovae [49]. The simulations

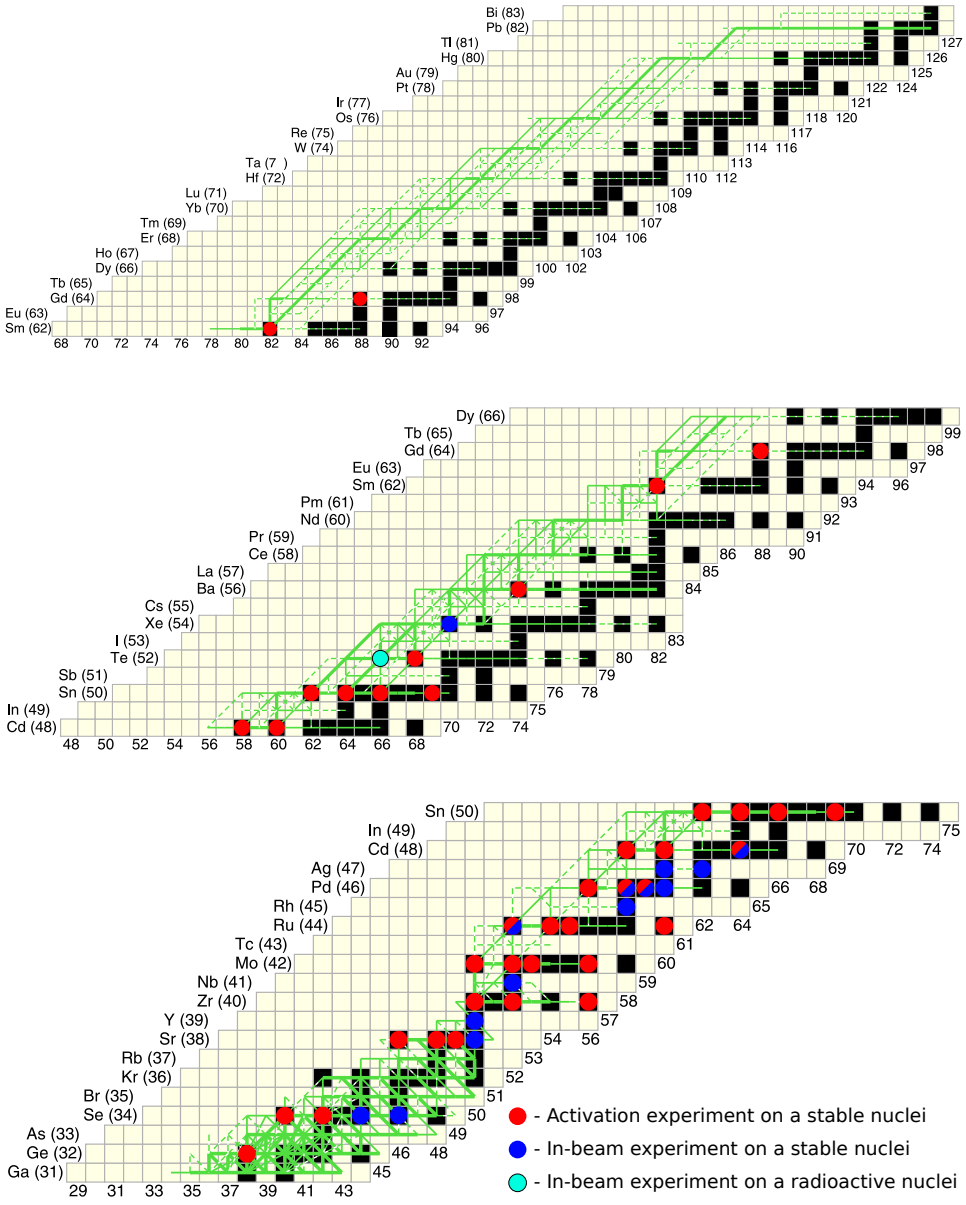

Figure 1.4: Simulation of the integrated reaction flux of a Type II SN explosion in the Ne/O layer with $T_{max} = 2,96\,GK$ for a $25M_{\odot}$ supernova model [29]. The width of the lines represents the strength of the reaction flow, in steps of factor 10. The reaction path extends deeply into the radioactive realm on the neutron-deficient side of the nuclear chart especially for nuclei with high mass number. The majority of the (p,γ) or its inverse reaction measurements, carried out with astrophysical motivation, are indicated where the initial nucleus is marked with a circle [8,9,67–97]. Activation and in-beam experiments are represented with red and blue colors, respectively. So far, all p-capture measurements were carried out only on a stable nuclei. The first (p,γ) measurement for the γ-process taken on an unstable nuclei, namely the ^{118}Te(p,γ)^{119}I reaction measurement, was carried out in this work and indicated with a cyan-colored circle.

are often carried out for different initial masses of the pre-explosive star, and then the calculated isotopic abundances are averaged together based on the occurrences of such pre-explosive stars. Note, that simulations require massive computational power, e.g., to include the correct hydrodynamical treatment of convective regions and isotope mixing in the models.

Extensive reaction network calculations include more than 1000 nuclei linked together by more than 10000 nuclear reactions. On Figure 1.5, the result of network calculations averaged for Type II supernova explosion models with different initial masses from $13M_{\odot}$ to $25M_{\odot}$ [52] is shown. The so-called normalized overproduction factors, denoted with $\langle F \rangle / F_0$, for p-nucleus are plotted as a function of the mass number. The results obtained for individual model stars are schematized by vertical bars. The contribution of the simulated process to the p-nuclei yields can be quantified by these overproduction factors, defined as a normalized ratio between the simulated abundance and the observed solar abundance for a certain nucleus. The solar p-nuclei abundances for higher mass numbers can be reproduced within a factor of 3. However, poorly reproduced abundances, such as the ^{92,94}Mo - ^{96,98}Ru region called as Ru-Mo anomaly, hint the inclusion of other processes in the p-nuclei production. Nevertheless, to draw precise conclusions, nuclear physics inputs to the model calculations need to be improved. Due to the lack of experimental data, the astrophysical models must strongly rely on the theoretical predictions of nuclear parameters leading to huge uncertainties in the resulting abundance values. The masses of the involved nuclei, thus the reaction Q-values as well as the half-lives are in general well known for the γ-process. However, apart from a handful cases there is no experimental data available for the cross sections of capture or of their inverse reactions even for stable isotopes. For p-capture reactions in the context of the γ-process so far there is no single experiment carried out on an unstable nucleus. The first (p, γ) reaction measured on a radioactive nuclei is presented in this work. The current situation regarding p-capture experiments with astrophysical motivation in the context of the γ-process is shown on Figure 1.4.

In case of nuclei with high level densities the Hauser-Feshbach model can be applied for cross section predictions. It is a statistical model based on particle potentials, level densities, γ-widths and mass tables. The required nuclear physics inputs can be obtained from experiments. Taking into account the huge number of laboratory measurements needed to cover the entire nucleosynthesis network, the focus should rather be on specific reactions. Not all reactions are equally important, the so-called key reactions influence the final p-abundances the most. Once these key reactions have

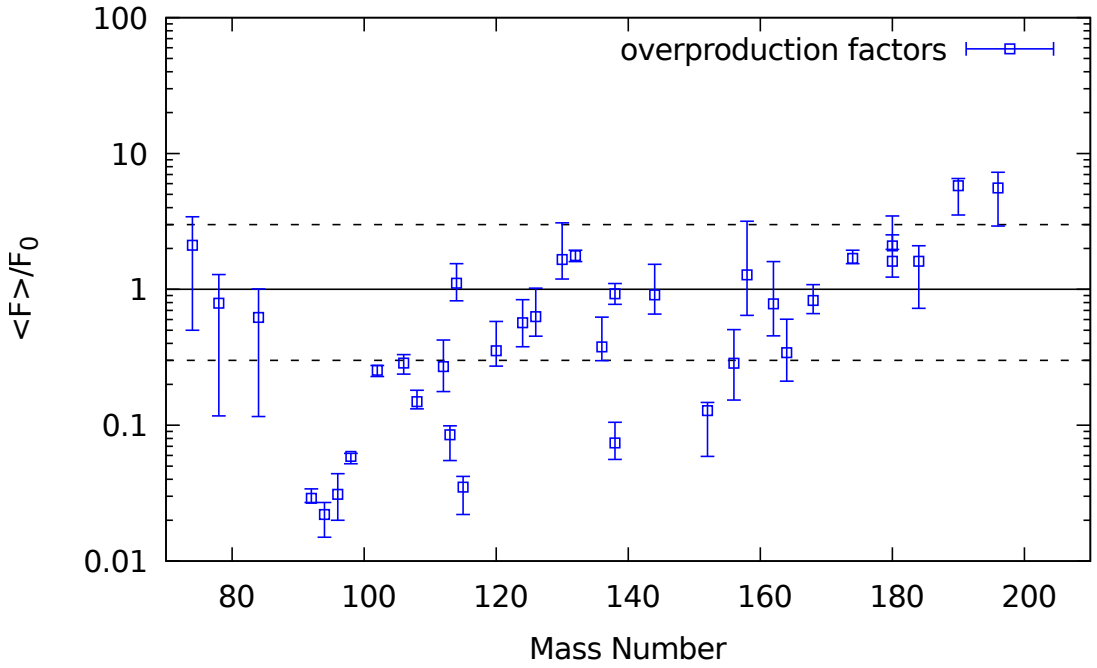

Figure 1.5: Extensive reaction network simulations include thousands of nuclei linked together by tens of thousands of reactions in order to model the γ-process of stellar nucleosynthesis. The normalized overproduction factors are plotted for p-nuclei as the result of averaged Type II supernova explosion models with different initial masses from $13M_{\odot}$ to $25M_{\odot}$ [52]. The spreads of results obtained for different model stars are schematized by vertical bars.

been identified based on sensitivity studies, they can be addressed by experiments ideally at energies present in stellar plasma, that is in the Gamow-window.

1.4.6 Challenges for experiments

The uncertainties in the nuclear physics input for the γ-process models can highly influence the network calculations. Hence it is utmost important to provide experimental data on the reaction cross sections at energies relevant for astrophysics. The nucleosynthesis network consists of a large amount of reactions, but so far only a handful of cases have been addressed experimentally. Figure 1.4 shows all isotopes, for which the (p,γ) cross sections have been studied at relevant energies until 2020. All of these measurements were carried out on stable nuclei in the light/intermediate mass region [8, 9, 67–97]. The limited number of measurements can be understood by taking into account all difficulties, such an experiment has to face. The most important ones are addressed in the following [11].

Small cross sections

The magnitude of cross sections for capture reactions is typically modest, ranging from milibarn to microbarn, just above to the Gamow-window and rapidly decreases with decreasing energy leading to low count rates for direct detection. On the one hand, this can be compensated by efficient detection techniques for the resultant particle. On the other hand, an excellent background suppression is required to increase the sensitivity. Often the cross section can only be measured at higher energies, where the rate of the reaction is higher. Thereby, the HF model parameters can be constrained and then be used for cross section predictions at relevant lower energies.

Reactions on unstable nuclei

The reaction network of almost all processes responsible for p-nuclei creation extends deeply into the region of unstable nuclei. Therefore, cross section measurements of capture or of their inverse reactions performed on unstable isotopes are inevitable. Nevertheless, the availability of sample materials is limited and traditional methods like the activation technique are not applicable for target nuclei with short half-lives. For capture reaction measurements performed on radioactive isotopes, rare ion-beam facilities, like the GSI Helmholtz Center for Heavy Ion Research [98], provide unrivaled opportunities.

Stellar quantities

In the stellar plasma, where the nucleosynthesis reactions are realized in nature, low-lying excited states of nuclei are thermally populated. Therefore, many reactions take place not only on nuclei in the ground state ($g.s.$) but also on exited states. This effect is called stellar enhancement and gives a significant contribution to the stellar reaction rate by altering the effective cross section of the reaction as compared to rates measured in laboratory. However, experiments performed on $g.s.$ nuclei still can provide parts of the stellar rate and can be compared to theoretical predictions.

Sensitivities

While the ultimate goal is to constrain the network calculations directly by experiment, it is also of high importance to constrain the nuclear theory which is heavily used in calculations. The main inputs are particle potentials, γ-strength functions, nuclear level densities, masses and half-lives. The reaction cross section depends on these inputs to various degrees at different interaction energies. In order to distinguish individual contributions, measurements in a wide range of energies are needed.

Therefore, the experimental setup should ideally allow flexibility regarding the interaction energy.

To overcome the experimental difficulties arising for astro-nuclear reaction measurements, storage rings coupled to a radioactive beam facility provide unrivaled opportunities. In the following chapter, one of the few storage ring facilities worldwide, the GSI facility complex, will be introduced in detail, focusing on its high-energy radioactive beam branch coupled to the Experimental Storage Ring at GSI.

Chapter 2

Proton-capture campaign at GSI

2.1 GSI Helmholtzzentrum für Schwerionenforschung

GSI Helmholtzzentrum für Schwerionenforschung in Darmstadt, Germany, or shortly GSI, is a leading research facility with more than 50 years of history dedicated to heavy ion research. It consists of a series of accelerators connected to a high-energy radioactive ion beam facility delivering exotic beams to various experimental areas. This unique structure provides an enormous research potential to study nuclear reactions, such as e.g. the p-process nucleosynthesis, efficiently using exotic-ion beams motivated by the astrophysical interests. Fully stripped ions can be stored at low energy effectively replicating the kinetic conditions in stellar plasmas.
The focus of this chapter is on the infrastructure of GSI needed to realize nuclear reaction studies on exotic nuclei. The introduction follows the path of the heavy ions starting from their production, through their preparation, until the experimental area.

2.1.1 Production of highly charged ions - UNILAC

The stable ions of interest start their journey at the beginning of the UNIversal Linear ACcelerator (UNILAC), which serves as the injector for the heavy-ion facility at GSI [99]. UNILAC along its about 120 m length can accelerate all ion species from hydrogen to uranium to roughly 20 % of the velocity of light with the repetition frequency of up to 50 Hz. The beam parameters, such as ion species, energy, intensity, and beam target area, can be varied rapidly allowing to run multiple experiments quasi-simultaneously.
There are three ion injectors of UNILAC, Terminal South, Terminal North, and the

Figure 2.1: Aerial view of the GSI research facility in May 2020. Courtesy: GSI Helmholtzzentrum für Schwerionenforschung GmbH, D. Fehrenz

High Charge State Injector, equipped with various ion sources. The sources can handle a great variety of ions from hydrogen up to uranium produced out of gaseous and solid materials with high ion beam currents. Bunches of ions are accelerated with the UNILAC. To increase the charge state, a dedicated gas stripper is employed. Eventually, the maximal velocities can reach 14.3 MeV/u, 13.5 MeV/u and 17.7 MeV/u for beams consisting of $^{130}Xe^{21+}$, $^{238}Xe^{28+}$ and $^{20}Ne^{7+}$, respectively [100]. At the last section of UNILAC, the beam can be sent to local low-energy experimental areas or can be transferred to load the heavy-ion synchrotron (SIS18) through the transfer channel (TK).

2.1.2 Acceleration of highly charged ions - SIS18

Ions coming from the UNILAC are injected at 11.4 MeV/u to the heavy-ion synchrotron of GSI (SIS18) as a of 100 µs bunch [102]. The duration of this process holds for 20 revolutions in the synchrotron leading to a so called multi-turn injection. Then, the ions are accelerated twice at each turn by two RF cavities while keeping them on a circular path by dipole magnets. The ions can be accelerated up to energies equivalent to maximal magnetic rigidity of 18 Tm, which corresponds to energies of roughly 2 GeV/u for $^{20}Ne^{10+}$ and 1 GeV/u for $^{238}U^{73+}$ [103]. To increase the beam intensity in a single acceleration cycle, a multi-multi injection can be applied. In this mode, the beam from a multi-injection is cooled by electrons, thereby reducing the

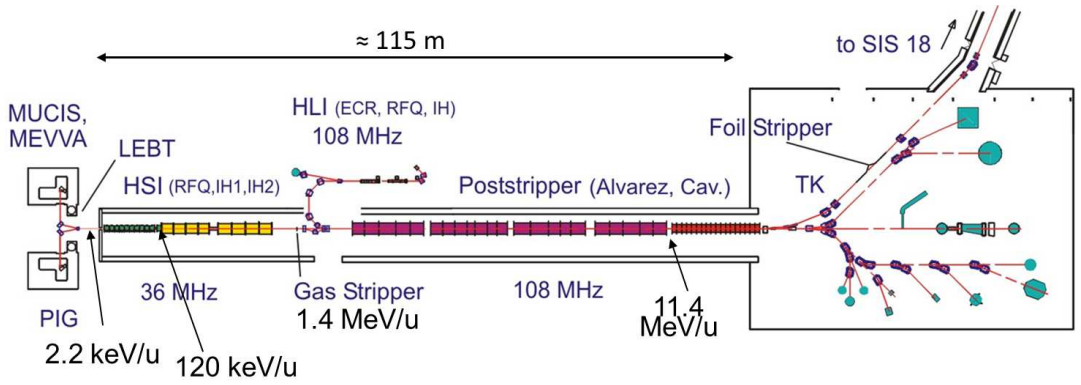

Figure 2.2: The structure drawing of the UNILAC linear accelerator at GSI [101]. A large variety of stable ions from hydrogen to uranium can be produced and transferred to the low-energy experimental area or injected to SIS18 for further acceleration and transmission.

beam-emittance. The freed phase space can be filled by a new multi-injection. Such process can be repeated several times.
After reaching the final energy, there are two ways for beam extraction. To direct the beam into the Experimental Storage Ring the so-called fast extraction needs to be applied. In this case, the fast kicker magnets kick out up to four particle bunches from the SIS preserving the phase relation between bunches. In the case of $^{124}Xe^{48+}$ ions, the nominal intensity per cycle was $2 \cdot 10^9$ ions at max. repetition rate of 1 Hz [104]. The other method is the so-called slow extraction or resonant extraction. It can provide a quasi continuous beam for several seconds used for various experimental studies.

2.1.3 Transfer of long-lived, easy-access ions to ESR

Ions with long half-lives, which are easily accessible at the ion sources like stable noble gases or even ^{238}U, can be transferred directly from SIS18 into the ESR through a transfer beam line. The beam line is equipped with an exchangeable stripper foil. At sufficiently high energies the foil strips away the majority of the remaining electrons off the ions [105]. The stripping is most efficient when the velocity of the projectile is the same classical orbital velocity of the electron required to be removed. In the first order approximation this velocity can be estimated by using the Bohr criteria [106]. The desired charged state like completely bare, hydrogen-like, helium-like etc., of the beam can be selected at the ESR by tuning the optical settings in such way, that

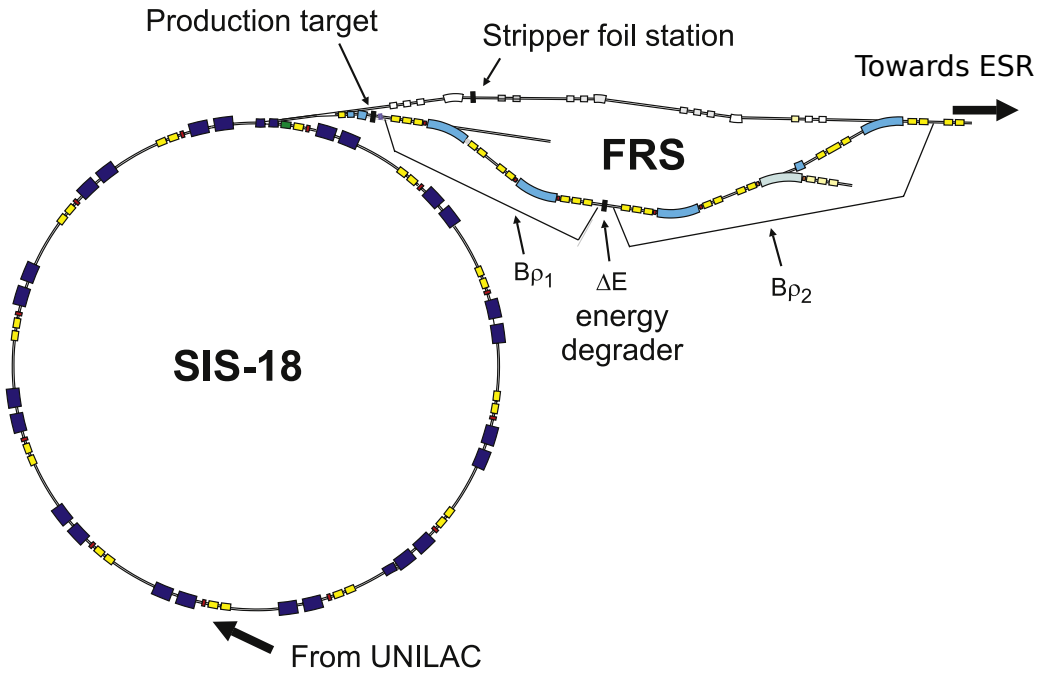

Figure 2.3: Illustration of the SIS18-FRS system at GSI [107]. At SIS18 the heavy ions injected from UNILAC can be further accelerated and transferred to ESR either via a transfer beam-line or through the high-resolution magnetic spectrometer of GSI, the FRS. The latter uses the in-flight separation technique based on the $B\rho$-ΔE-$B\rho$ separation method to supply exotic beams.

other charge states are out of the injection acceptance of the ring.

2.1.4 Production of exotic nuclei - FRS

The so-called in-flight separation technique allows one to study most exotic nuclei [108]. The flight time between production from the target to the ring is in the range of a few 100 ns to 1 µs. Separation of ions of interest is done in flight.
After the interaction between the primary beam and the production target, secondary nuclei have characteristic charge state distributions. At energies relevant for this work, only a few electrons remain bound to the nucleus. To discriminate for isobaric contaminants in the same atomic charge state a $B\rho$-ΔE-$B\rho$ separation technique [109] has been developed. The magnetic rigidity, $B\rho$, is tuned by the dipole magnets at the initial and final sections realizing the electromagnetic separation. The ΔE term refers to the energy loss which is realized by using a degrader. When ions penetrate through

material they suffer energy loss, which is with good approximation proportional to Z^2, where Z is the atomic number of the projectile [110]. Relatively thin beryllium targets are typically used with thicknesses of 1–8 g/cm^2. As a result of the separation technique, mono-isotopic beams can be produced and delivered to experiment.
At GSI the high-resolution magnetic spectrometer is the so called FRagment Separator (FRS) [111]. Among other purposes, it connects the SIS18 ring accelerator with the ESR as illustrated on Figure 2.3. At the beginning of the FRS a production target is placed. Various targets made from numerous materials with variety of thicknesses to optimize the production of the secondary ions are available. This is followed by a combination of magnetic dipoles deflecting the fragments and magnetic quadrupoles focusing the fragment beam. In the middle section, S2, the energy degrader is shown which reduces the energy of the fragments selectively by their nuclear charge. By applying once again electromagnetic separation in the final section an isotopically pure beam can exit the fragment separator.

2.1.5 The Experimental Storage Ring

The ESR is one of the main workhorses of GSI. It allows to slow down and store charged particles arranged into a high-quality bunched beam. Six dipole magnets keep the stored ions on a quasi-circular trajectory and allow to recycle the exotic beam, which means a boost of the luminosity for in-ring measurements. Quadrupole and sextuple magnets are ensuring beam focusing and second-order ion-optic corrections. The ESR is capable to operate at up to 10 Tm maximum magnetic rigidity providing a large acceptance for the injected beam.
One remarkable feature of ESR is its beam cooling technique. Cooling in this context means the improvement of the properties of an injected “hot” beam such as transversal size, velocity spread and angular divergence and hence, the reduction of its emittance. Utilizing a proper active cooling scheme the beam emittance can be reduced by several orders of magnitudes. The techniques used at the ESR comprise stochastic cooling and electron cooling which provides flexible and fast beam cooling for all ions in the energy range below 400 MeV/u.
The RF cavities enable beam deceleration giving access to low energy ions down to few MeV/u for a wide range of nuclei even after their in-flight production at high energy [113]. This unique feature allows to replicate the stellar conditions in a storage ring, thereby, to carry out experiments important for astrophysics. The ring operates at ultra-high vacuum (UHV) of about 10^{-11} mbar, which is essential for storing highly-charged ions over extended periods of time especially at low energies. This

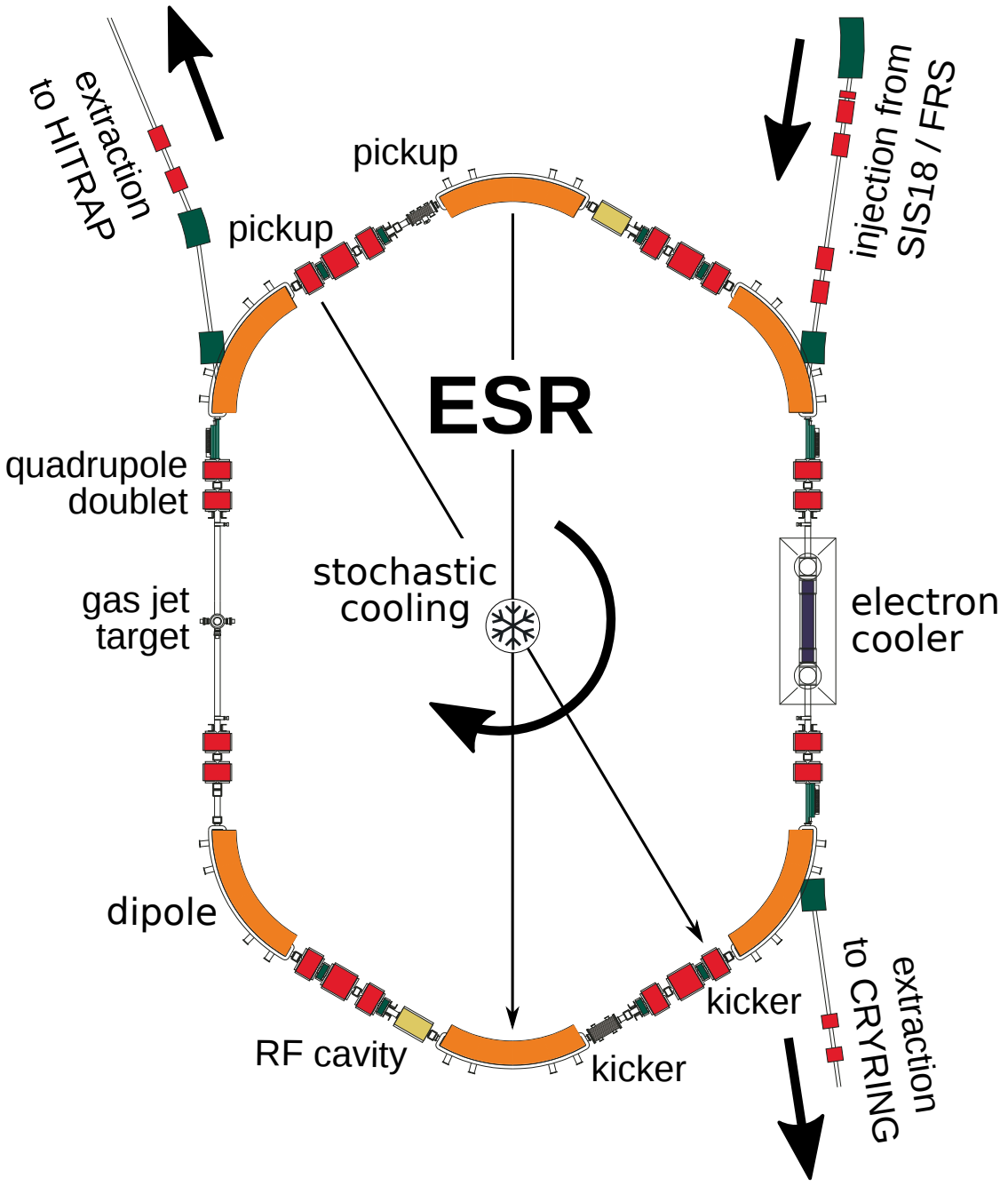

Figure 2.4: Schematic view of the Experimental Storage Ring [107, 112]. The heavy ion-beams are injected from SIS18 and can be either stored in the ESR, or transferred further to CRYRING or HITRAP. The ring is equipped with stochastic and electron cooling systems, with RF-cavities which can bunch, accelerate or decelerate the beam, with an internal gas target and with many ports allowing the placement of particle detectors. The rest gas pressure inside the ring reaches 10^{-11}mbar.

requires the usage of low-outgassing materials within the ring and a bake-out at $\sim$ 350 ^{o}C in standard circumstances or for a minimal bake-out temperature near 150 ^{o}C for a longer period of time.

Stochastic cooling
Stored ions oscillate along the reference orbit in the ring, which is called betatron oscillation. The spatial deviation caused by this oscillation is measured by "pick-up" plates on the one side of the ESR and the signal is sent to the kicker device. The kicker magnet is placed in a fixed position of the ring such that this spatial deviation is converted into an angular mismatch, which can be corrected in the same turn. At the ESR stochastic cooling can be realized at 400 MeV/u beam velocity defined by the distance between the pick-up and the kicker [114]. The time required for stochastic cooling at the ESR is typically in order of seconds. Since the revolution frequency of the beam is at around 1 MHz, this means a 2$\times$ a few million kicks during a cooling period. Eventually, the momentum spread can be reduced to approximately $\Delta p/p \sim 10^{-3}$.

Electron cooling
The relative momentum spread of the stored ions can be further decreased by applying the electron cooling technique. Electrons from a cathode are accelerated to relativistic energies (up to 500 kV). This beam of electrons with velocity equal to the ions but with small energy spread overlaps with the ion beam for a section of two and a half meters length. In the moving frame of the ions, it appears as mixing of the ions with a cold gas of electrons. Due Coulomb interactions between the ions and the cold electrons the kinetic energies exchange leading to the reduction in the energy and angular spread of the ions in the laboratory frame. Whereas the ions pass through the electron cooler at each turn, they remain stored in the ring but the electrons are constantly renewed. By employing electron cooling in combination with stochastic pre-cooling a momentum spread in order of 10^{-7} can be achieved.

The stored, cooled, high-quality heavy ion-beam can be used for in-ring reaction measurements. For such experiments, an internal gas target is installed at the ESR, see Figure 2.4. The target is thin such that only a single interaction can safely be considered for one passage. The target material is usually lighter mass than the ions orbiting in the ring, resulting in reactions in inverse kinematics. Large variety of gases can be used to realize in-ring reaction, such as H_2, d, ^{3}He, ^{4}He, Ar, Xe, etc.

The density of the target can reach about 10^{14} atoms/cm^2 for H_2 target. Until this density the electron cooler is able to compensate for the energy loss of the beam at the target.
The other possibility is to extract the beam at low energies towards HITRAP [115,116] or towards the other storage ring currently in use at GSI, CRYRING [117, 118].

2.1.6 CRYRING@ESR

CRYRING [117, 118] is the first storage ring installation in the FAIR project. It is coupled downstream of ESR extending the reaction studies on cooled, highly-charged stable or even exotic nuclei to lower energies. Due the extreme-high vacuum (10^{-12} mbar) of CRYRING, it is envisioned that the beam can be stored at energies down to tens of keV/u with beam lifetimes up to minutes for ions even with the highest charge states. Utilizing its electron cooler and internal gas target, CRYRING is a sensitive measurement tool to investigate low-energy nuclear reactions and preform delicate spectroscopy in the atomic realm for ionization, recombination, excitation, and resonant scattering. It can also operate standalone, owing to its independent injector beam-line. The first successful ion beam storage was demonstrated in autumn 2017 [119]. In addition, in the framework of FAIR Phase-0 program [120], the first beam transfer and storage of ions from ESR was achieved in the end of 2019.

2.1.7 The upcoming FAIR facility

The Facility for Antiproton and Ion Research (FAIR) will be a next-generation accelerator facility representing a global flagship for fundamental and applied sciences for the coming decades. It provides unprecedented research potential in various fields, including hadron, nuclear, atomic physics, and nuclear astrophysics as well as applied sciences like materials research, plasma physics and radiation biophysics with applications towards ion therapy and space science [124]. It is currently under construction at the campus of GSI, its Phase 0 activities are already in realization [120].

In Figure 2.5 the existing GSI facility and the planned FAIR complex is shown. Heavy ions from the UNILAC or protons produced at p-LINAC can supply the core device of FAIR, the heavy-ion super conducting double-ring synchrotrons, SIS100 and SIS300. From these accelerator rings beams at high energies with unprecedented high intensities and quality can be transferred to several experimental areas for fore-front research. The four main scientific pillars of FAIR are

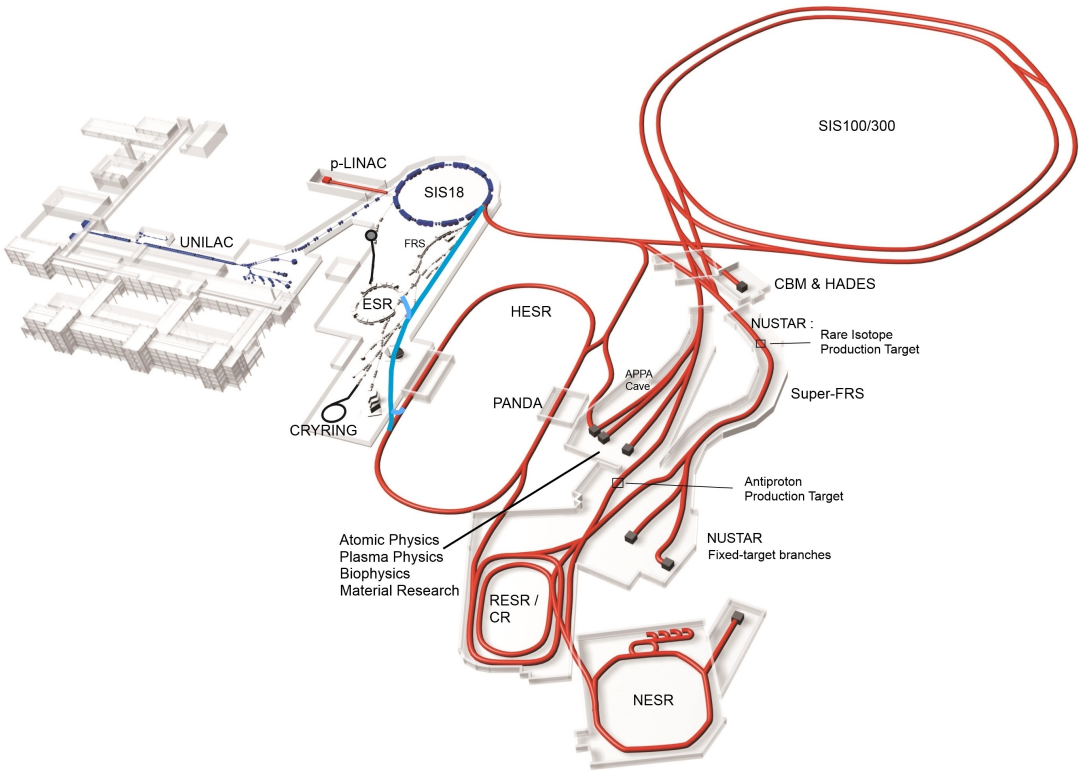

Figure 2.5: The conceptional design of the full version of FAIR next-generation accelerator facility coupled to GSI [121]. FAIR is currently under constraction. In the first stage, the *Modularized Start Version* will be built [122, 123] including the superconducting synchrotron SIS100, transfer channels and the Super-FRS, the cooler storage rings HESR and CR, and all detectors for the four research pilars of FAIR (APPA, CBM & HADES, NUSTAR, PANDA).

- APPA [125] - Atomic and Plasma Physics and Applications such as medical and material sciences
- CBM and HADES [126] - Compressed Baryonic Matter realized in relativistic nucleus-nucleus collision experiments
- NUSTAR [127] - Nuclear Structure, Astrophysics and Reactions by utilizing the radioactive beam facility, the Super-FRS
- PANDA [128] - AntiProton ANnihilation in Darmstadt with its hadron physics detector system.

The Modularized Start Version (MSV) [122, 123] of FAIR will consist the superconducting synchrotron SIS100 supplied by the UNILAC and SIS18, the transfer

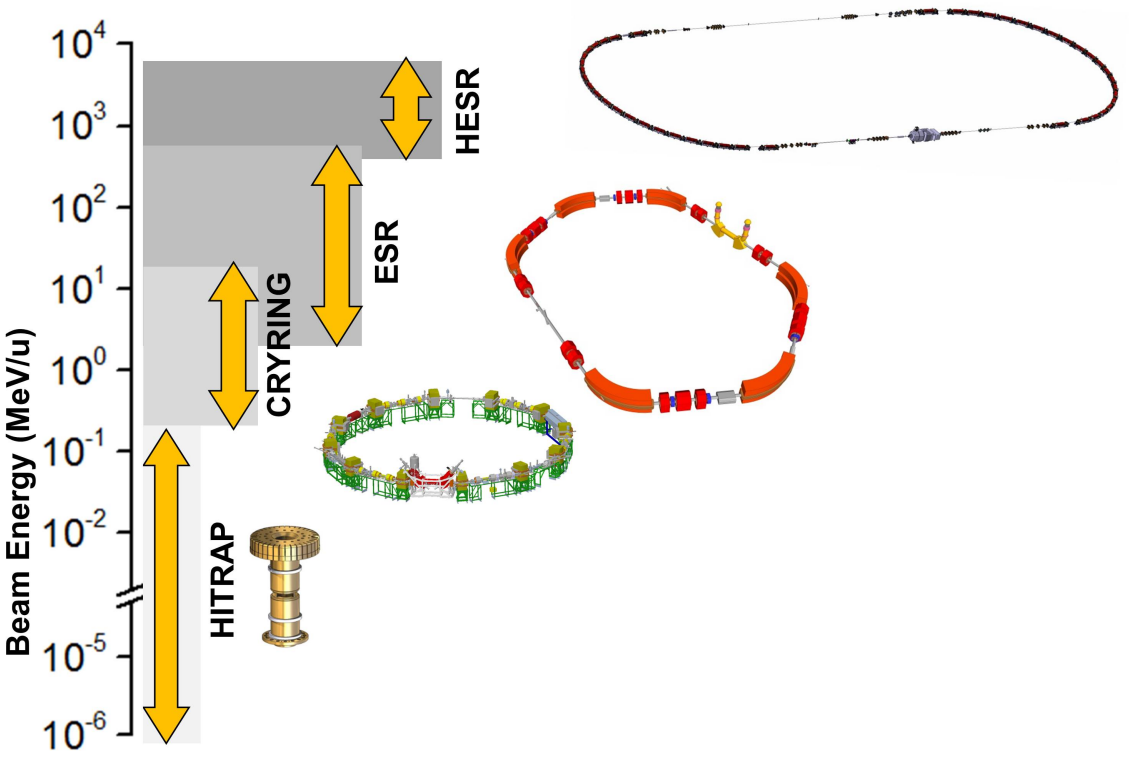

Figure 2.6: The future HESR at the FAIR facility in combination with the HITRAP ion-trap, and with the two storage rings at GSI, the CRYRING and ESR, will uniquely cover continuously a more than 10 orders of magnitude kinetic beam-energy range for even highly charged ions from hydrogen up to uranium. Credit to [121]

channels and the Super-FRS, the two cooler-storage rings HESR and CR, and all detectors for the four flag research groups at FAIR. Thereby uniquely, GSI and FAIR facilities together, utilizing the HITRAP ion-trap, and the CRYRING, ESR, HESR storage rings, can cover continuously a more than 10 orders of magnitude kinetic beam-energy range between 10^{-6} MeV/u - 10^{4} MeV/u for highly charged ions from hydrogen up to uranium.

2.2 Experimental method

Storage rings when coupled to a radioactive beam facility provide unrivaled opportunities to study the p-process nucleosynthesis. The setup of the Experimental Storage Ring (ESR) at GSI allows efficient capture reaction measurements even for exotic nuclei. Uniquely in the world, beams can be fully stripped and stored at low, few

MeV/u energies down to 3 MeV/u well suited for astrophysically motivated studies. So far three proton-capture experiments were carried out at the ESR. In this chapter, first, the experimental method will be introduced, then, the two former, stable beam experiments will be shortly described. The recent, radioactive-beam experiment constitutes the central part of this work and will be discussed in detail in the later chapters.

2.2.1 Suitability of the ESR for (p,γ) reaction measurements

The capture reactions at the ESR are carried out in inverse kinematics. As a projectile, fully stripped, heavy-ion species of astrophysical interest can be selected. As target, a large variety of gases are available including molecular hydrogen enabling proton-induced reaction studies. One of the most significant exit channels at low center-of-mass energies is the (p,γ) channel. The (p,γ) is one of the key reaction in the nucleosynthesis network of the p-process, thereby, having a high importance for the p-nuclei production.
It should be mentioned, that as a target gas He is available as well raising the interest towards (α,γ) reactions, which have also large impact in the p-process nucleosynthesis. However, for heavy ions such as $^{124}Xe^{54+}$, due to the kinematics, the cone of the (α,γ) products increases rapidly in the spatial directions. This leads to unwanted collisions with the walls of the beam pipe making any measurement highly complicated if not impossible.

2.2.2 Identification of the (p,γ) events

The dipole magnet downstream the target section of the ESR ensures a magnetic separation between the emitted ions of the nuclear reactions and the stored beam, see Figure 2.7. The bending radius ρ of ions inside a homogeneous, constant magnetic field B can be described by a simple formula derived from the Lorentz and Centripetal forces

$$B\rho = p/q \tag{2.1}$$

where p denotes the momentum of the ions with charge state q. After (p,γ) reaction, the momentum of the ions remains roughly unchanged, while their charge increases by one. This results in a decreased bending radius. Therefore, the (p,γ) reaction products travel on the inner trajectories within the dipole with respect to the beam. Since the momentum taken by emitted photons can be neglected, as compared to the beam energy, the (p,γ) events form a narrow cluster on the detector. In case of a

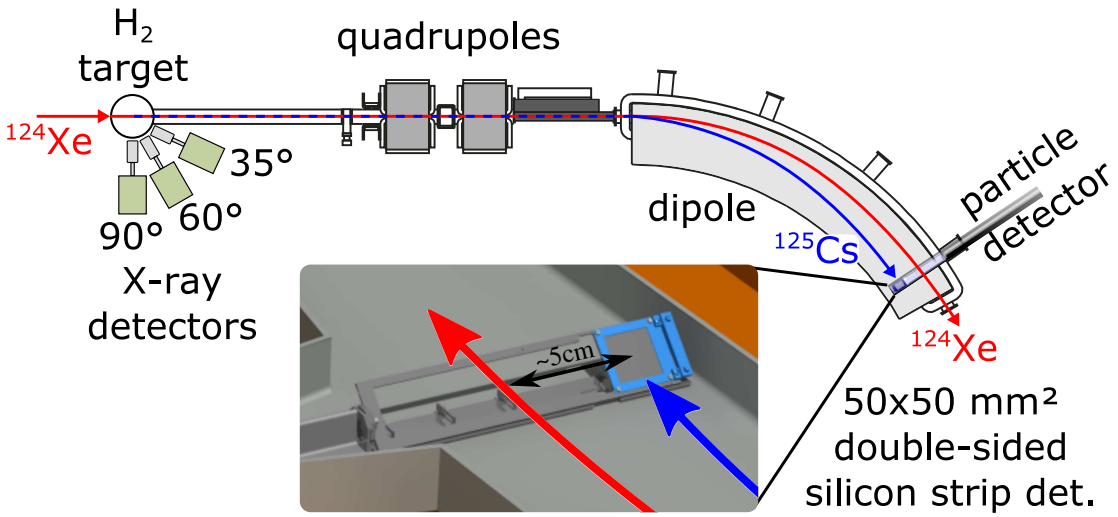

Figure 2.7: The arrangement of the ^{124}Xe experimental setup at the ESR [8]. The Double-Sided Silicon Strip Detector (DSSSD) is placed at the end of the first dipole after the gas jet target. The position allows the separation of the (p,γ) reaction products from the beam by about 5 cm. The stored beam can pass undistrubed through the detector support structure. Three Xray detectors surround the target to measure the co-acting K-REC process. The well understood cross section of this atomic process is used to reduce drastically the uncertainties of the (p,γ) measurement which originates from the poorly known luminosity. The detailed description can be found in text.

different reaction channel, (p,n) reaction, the charge of the ions also increases by one as well resulting to trajectories on the inner orbits. However, the trajectory of the lighter (p,n) ions bends more than for (p,γ) ions, while the size of the (p,n) reaction cone increases due to the larger recoil by the emitted neutron.

It is important to note, that the separation of the (p,γ) products works only, if the beam is fully stripped. If an ion in the beam loses an electron, its charge changes by $\Delta q = +1$, while their momentum remains roughly constant leading to trajectories comparable to the (p,γ) ions. Moreover, electron-loss is an atomic process with typically orders of magnitudes higher cross section than the nuclear (p,γ) process. Therefore, using, e.g., a H-like beam would cause a massive background on the detector underneath the (p,γ) events, thereby, decreasing the sensitivity tremendously for the identification of the (p,γ) events. In case of electron captures, however, analogously to the (p,γ) reaction, the trajectory of the products always bends towards the outer orbits with respect to the beam.

To simulate the trajectories of the ions within the ring, the MOCADI code is a pow-

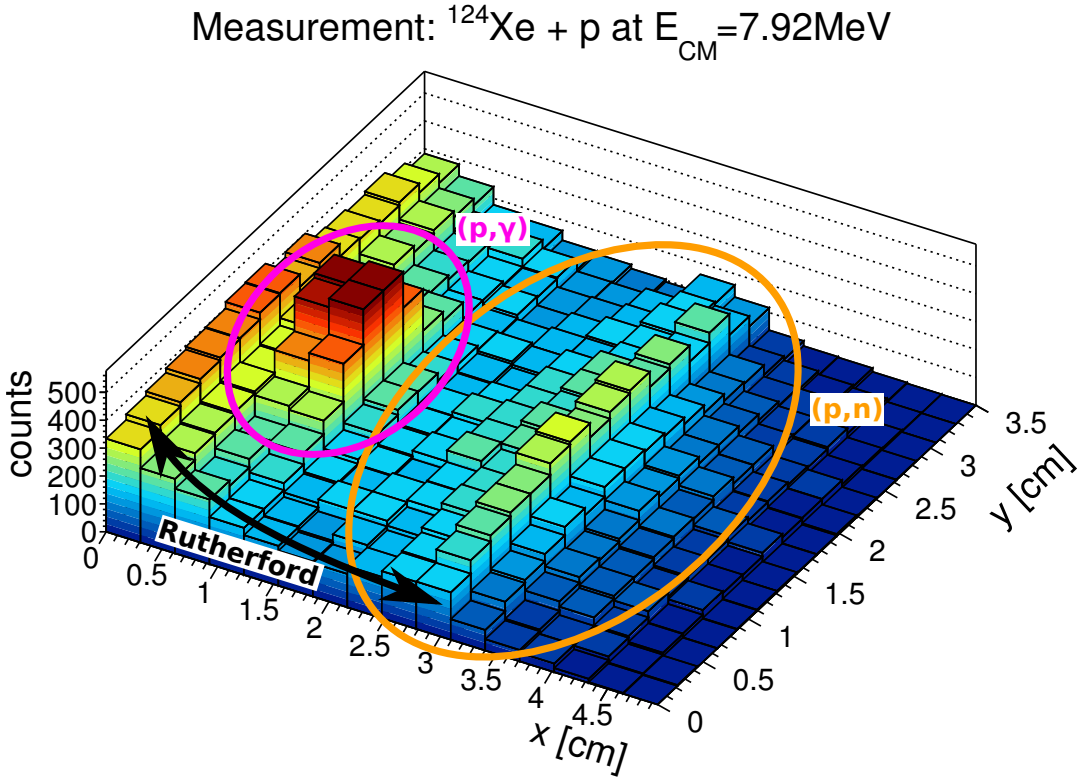

Figure 2.8: An example spectrum of the DSSSD for the ^{124}Xe dataset. The number of valid hits are plotted as the function of the radial axis (x-axis) with respect to the ring and of the vertical axis (y-axis). The units are given in cm, the strips are 300 µm wide with roughly 9.4 µm separation in between. The (p, γ) and the (p, n) products form dominant clusters on the top of the Rutherford background. The beam is located roughly 1.5 cm away from the first x strip in the negative direction. The detector is tilted by 45°. Therefore, the nearly circular (p, γ) distribution looks contracted with a factor of $\sqrt{2}$ along the y-axis. The spectrum can be well reproduced with the MOCADI simulation.

erful tool [129]. It uses a Monte Carlo approach and includes ion optics of the ring as well as the dynamics of the reactions in inverse kinematics.

In order to capture the nuclear reaction products of interest efficiently, the inner orbits must be covered while leaving the circulating beam to pass undisturbed. Accordingly, a particle detector is installed in a position where the separation exceeds 5 cm between the beam and the (p, γ) products. The detector is a double sided silicon strip detector (DSSSD) consisting of a Micron Semiconductor Ltd W1-type DSSSD manufactured by [130]. It is surrounded by a few centimeter thick PCB board for the read out. The square shaped detection area with edge length of 49.5 mm is segmented

into 16 strips on both sides arranged perpendicularly. The thickness of the detector is 500 µm. Therefore, e.g., ^{124}Xe ions with energy less than about 38 MeV/u are completely stopped within the detector volume [131, 132]. The deposited energy can be well resolved with the silicon detector opening the possibility to improve particle identification.
In Figure 2.8 an example spectrum of the silicon strip detector is shown. The (p, γ) products form a narrow cluster on the tail of the Rutherford scattering distribution. The setup is positioned in such a way inside the dipole, that the (p, γ) peak is centered on the DSSSD and all ^{125}Cs ions are safely detected. Therefore, all (p, γ) events can be identified and counted with high precision. When it is energetically allowed, part of the (p, n) reaction products is recorded with the DSSSD as well, see Figure 2.8. The measured particle distributions can be well reproduced using the MOCADI simulation tool [129].

2.2.3 Measurement at astrophysical energies

The ESR operates at 10^{-11} mbar restgas pressure achieved by the usage of mechanical pre-pumping, ion getter pumps and a special heating procedure called bake-out. To prevent any pollution, all non-UHV detectors, located inside the ring, must be enclosed into so-called detector-pockets. Such pockets are made of stainless steel and have a thin entrance window (between 25 µm and 100 µm in thickness) in front of the detection surface. However, to reach the detector the ions must travel through this layer of material implying an unwanted upper limit for the beam energy. The minimal required energy was measured for ^{96}Ru ions to be about 9 MeV. In order to fit into the Gamow-window with an upper border typically around 5 MeV/u, the proton-capture products should not suffer from any major or fatal energy loss before reaching the detector surface. For this reason, the application of an in-vacuum detector is unavoidable.
Therefore, in the latest two experiments a modified, UHV-compatible double sided silicon strip detector (DSSSD) was employed. The UHV compatibility of the detector relies on two major features. On the one hand, the bake-ability of the device above 100 °C is ensured by a ceramic PCB board and by the special heat-resistant glue-based bonds at its cable outlet. On the other hand, the low out-gassing rate of the detector is guaranteed by the usage of exclusively UHV-proof materials.

2.2.4 K-REC normalization technique

To obtain the luminosity in the "classical" way in a storage ring, the amount of ions within the beam, the revolution frequency, the target density and the effective overlap between target and the beam must be precisely known. However, especially the latter quantity one can only roughly estimate leading to large uncertainties. To avoid the need for luminosity determination in the cross section calculations, a measurement relative to a well-understood, co-acting process can be carried out. During the proton-capture campaign the K-REC process was selected for normalization. This process occurs when an electron from the target molecule is captured to the K-shell of the projectile ions while a photon is simultaneously emitted.
The number of (p,γ) counts on the Si detector $N_{(p,\gamma)}$ can be expressed with the reaction cross section $\sigma_{(p,\gamma)}$ and with the luminosity integrated over time L_{int} as

$$\sigma_{(p,\gamma)} \cdot L_{\text{int}} = N_{(p,\gamma)}. \tag{2.2}$$

Analogously a second equation can be written for the co-acting K-REC process at the target as

$$\sigma_K \cdot L_{\text{int}} = N_K. \tag{2.3}$$

The K-REC process can be well described by theory, which allows us to replace σ_K with a theoretical estimate σ_K^{theory}. Using the combination of Eq. 2.2 and Eq. 2.3, the poorly-known luminosity can be eliminated from the cross section determination of the (p,γ) reaction

$$\sigma_{(p,\gamma)} = N_{(p,\gamma)} \frac{\sigma_K^{\text{theory}}}{N_K} = N_{(p,\gamma)} \frac{\epsilon_K \Delta\Omega}{N_K} \frac{d\sigma_K^{\text{theory}}}{d\Omega}. \tag{2.4}$$

As it is visible from Equation 2.4, the luminosity is eliminated by measuring the number of K-REC events N_K simultaneously and by using σ_K^{theory}. The formula can be further expanded with the inclusion of the K-REC measurement method.
An X-ray measurement setup is placed around the target consisting of germanium detectors in order to record emitted photons. The number of K-REC photons can be determined by subtracting the counts from the K-REC peak in the measured spectrum after background removal. On the right side of Eq. 2.4 the term with ϵ_K represents the detection efficiency of a single detector and $\Delta\Omega$ denotes the solid angle covered by the X-ray detector. All these terms can be precisely determined and will be discussed in more detail in the context of the recent experiment, see Chapter 5.4. The last term in Equation 2.4 involves the theoretical description of the K-REC

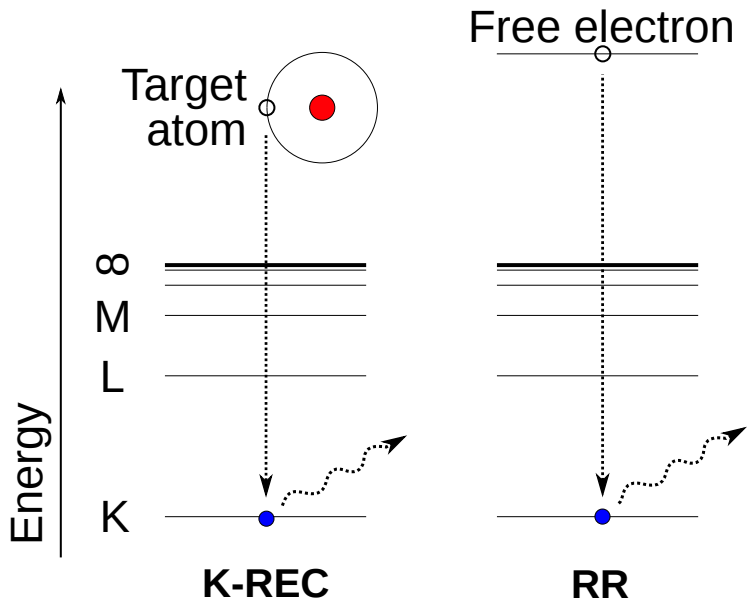

Figure 2.9: The cross section of the (p, γ) reaction is normalized to the K-REC process which occurs when the bound target electron is captured by the projectile into its empty K electron shell while simultaneously emitting a characteristic X-ray quantum. The process can be well-approximated as a modified radiative recombination process (RR), thereby, the theoretical uncertainties are kept in the range of 1 %. [133]

process. K-REC is a dominant mechanism for ion-atom collisions and occurs when the bare projectile ion captures a bound e^- from the target atom into the K-shell with a subsequent γ emission, see Figure 2.9. The weakly bound target electron can be handled with good approximation as quasi-free electron, thereby, the capture can be described as a slightly modified radiative recombination (RR). This is a well-understood approach and the process can be precisely calculated with an uncertainty in the range of $\sim$ 1 % [133].

The K-REC normalization method is a powerful tool to eliminate the uncertainty arising from the inaccurately known luminosity during an in-ring measurement. However, recently it was also demonstrated that the cross section can be determined with uncertainty in the order of 10-20 % by using the Si detector alone [134]. The method is based on the independent luminosity determination from the Rutherford scattering background on the DSSSD.

2.3 Former proton-capture experiments at the ESR

2.3.1 The ^{96}Ru experiment

The pioneering experiment to measure the proton-capture in inverse kinematics using a storage ring took place in 2009. The experiment was carried out with stable, bare ^{96}Ru ions at the ESR. In addition to the proof-of-concept aspect, the experiment had significant scientific importance. While the abundances for about 60 % of the p-nuclei can be reproduced within a factor 3, the production of ^{94,96}Mo - ^{96,98}Ru region in the γ-process is massively underestimated with a factor 20-50 [52].
Stable ^{96}Ru ions were accelerated in the UNILAC, than transferred and further accelerated in SIS18 to 100 MeV/u. The remaining bound electrons were fully stripped off in the transfer channel, see Figure 2.3 and the ions were injected into the ESR. Then, ^{96}Ru^{44+} ions were decelerated to 9 MeV/u, 10 MeV/u and 11 MeV/u by the RF cavities while simultaneously ramping the magnetic field of the dipole magnets. Utilizing the electron cooler of the ESR the momentum spread of the beam was reduced to $\Delta p/p \sim 10^{-3}$ and the diameter to 5 mm. In the storage phase, $5 \cdot 10^6$ ^{96}Ru^{44+} ions remained available with beam life time of several hundred seconds. Within the storage phase, windowless gas jet target was switched on providing hydrogen microdroplets of high density [135]. Assuming 400 kHz revolution frequency along with 10^{13} cm^{-2} effective target density, average luminosity of about $2 \cdot 10^{25}$ cm^{-2}s^{-1} was achieved [8]. Three independent detector systems were established to identify the outgoing particles from the interaction zone between the beam and the target.

In order to detect products of the nuclear reactions, two double sided silicon strip detectors (DSSSD) were installed behind the first dipole after the target. Each DSSSD had an active area of 4.95×4.95 cm^2 segmented into 16 strips on each side arranged perpendicularly. The DSSSDs were placed into a case, a detector pocket separated by a 25 µm stainless steel window from the high-precision vacuum of the ESR. The two detectors were arranged adjacently orthogonal to the beam axis to cover a larger spatial range. Due to the PCB boards surrounding the active detection surface, the setup has an inactive gap of $\sim$ 21.5 mm between the DSSSDs. However, setup was movable along the radial axis with respect to the ring, thereby, a continuous spectrum could be achieved by combining measurements taken at different positions. The enlarged detection area allowed one to catch all ^{97}Rh^{45+} ions, the products of the ^{96}Ru^{44+}(p,γ) reaction and other channels like (p, α), (p, n) partly as well. It should be noted, that the stainless steel window in front of the DSSSDs acted as a barrier

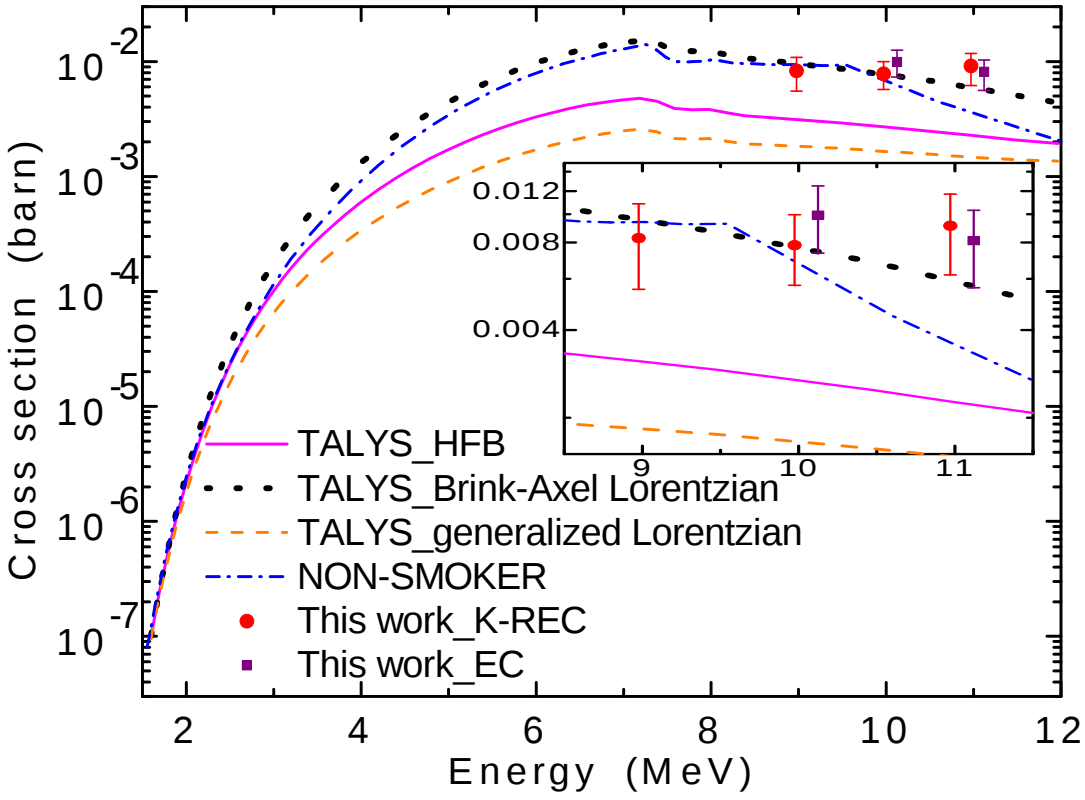

Figure 2.10: The cross section of the ^{96}Ru(p,γ)^{97}Rh reaction was successfully measured at 11 MeV, 10 MeV and 9 MeV center-of-mass energies [8]. The results are normalized to the K-REC normalization method at all energies using the X-ray dataset, and at 11 MeV, 10 MeV using the MWPC data as well. Both independent methods are in good agreement.

preventing ions below 9 MeV/u to reach the detector surface.

In addition to the detection of the nuclear reaction products, the co-acting electron capture process from the atomic shells of the target were also recorded with two separate detection systems. One setup was placed roughly centered in the first dipole magnet downstream the target to cover outer trajectories with respect to the beam. It consisted of a multi-wire proportional chamber (MWPC) detector with position resolution in the mm range. Projectile ions, which captured one or more electrons in the target, hit the MWPC with a few centimeter spacing depending on their charge state, see Eq 2.1. Therefore, the one, two, etc. electron capture peaks became clearly separable in the spectrum. With this direct detection of the e^--capture products, both the radiative and the non-radiative components could be recorded. The one-electron peak corresponds dominantly to the one electron-captures from the target,

while the other peaks originate mostly from beam interactions with the residual gas near to the target. The other setup consisted of a germanium detector placed at 90^o from the inside with respect to the beam axis in order to measure the K-REC photons for cross section normalization.

The cross section of the ^{96}Ru(p,γ)^{97}Rh reaction was successfully measured at 11 MeV, 10 MeV and 9 MeV center-of-mass energies. The results show a good agreement for the two normalization methods using the MWPC and the X-ray data, see Figure 2.10.

2.3.2 The ^{124}Xe experiment

After the successful demonstration of the feasibility of a (p, γ) experiment at the ESR, the next step in the proton-capture campaign at GSI was realized in 2015. The aim was to determine the proton capture reaction cross section using a stable heavy ion beam at the ESR at astrophysically important energies, possibly in the vicinity of the Gamow-window of the particular reaction.
However, in general decreasing the beam energy for the (p, γ) reaction corresponds to massive decrease in the reaction cross section. In the few MeV center-of-mass energy range, the dependency is close to exponential, see Figure 2.10. To compensate the low rates in some extent, the stable ^{124}Xe ions offered a great prospect. Xenon can be procured as an "easy-handle" noble gas, which is accessible as a high intensity beam. In addition, the abundance of ^{124}Xe can be reproduced by the γ-process models only within about a factor 3, see Figure 1.5.

At the start of the measurement phase within the ESR cycle of the ^{124}Xe(p,γ)^{125}Cs experiment, about 10^6-10^7 fully stripped ^{124}Xe^{54+} ions were stored in the ESR at five different low energies with momentum spread of $\Delta p/p \sim 10^{-5}$. The beam passed through the hydrogen gas jet target $2.5 \cdot 10^5$ - $5 \cdot 10^5$ times per second resulting in peak luminosities of 10^{26} cm^{-2}s^{-1} [9]. Excellent vacuum condition for the entire ring is essential to maximize beam life time and improve the duty cycle. During the experiment, the vacuum reached about $5 \cdot 10^{-11}$ mbar corresponding to 2.5 s beam life time. An ESR cycle took 50 s including a $\sim$ 10 s long measurement [9].

The detectors for the ^{124}Xe experiment were arranged in a similar way as in the previous ^{96}Ru experiment. One double sided silicon strip detector (DSSSD) was placed at the end of the first dipole (at $\sim 53.5^\circ$ from 60° bending angle) after focusing quadrupole duplett and the gas jet target. The position allows the spatial separation

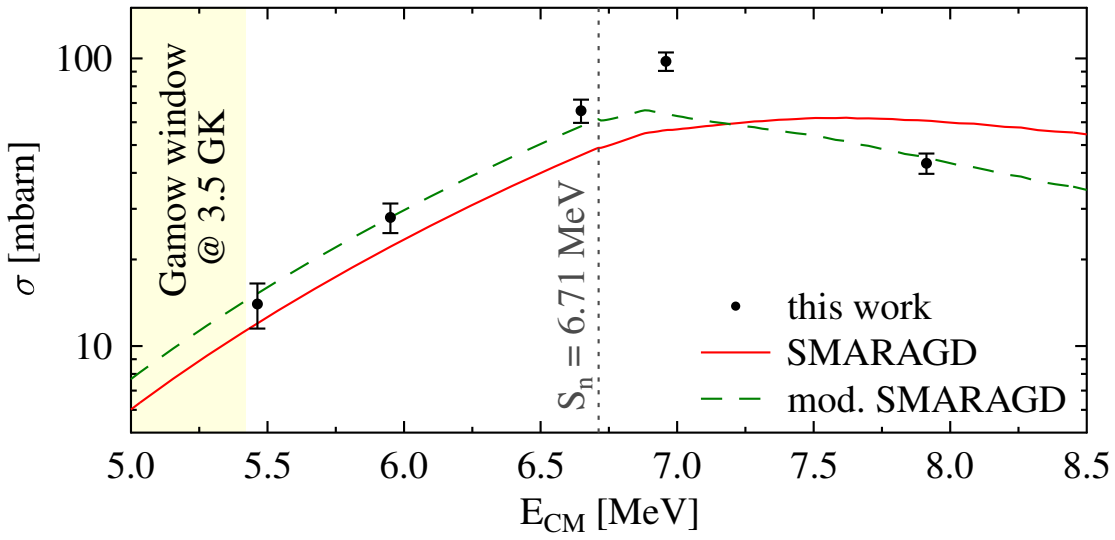

Figure 2.11: The cross section of the ^{124}Xe(p,γ)^{125}Cs reaction has been successfully measured at five different center-of-mass energies from 8 MeV down to 5.5 MeV approaching the Gamow window of the reaction within less than 100 keV. Therefore, the applicability of the method is proven for heavier nuclides at the astrophysically relevant energies. Figure is extracted from [8]

of the (p,γ) reaction products from the stored beam by about 5 cm. The DSSSD is supported by a specially designed detector holder connected to a long movable arm. The holder tilts the detector by $\sim$45° making it fit horizontally between the yokes of the dipole magnet and has a window for the circulating beam leaving it to pass undisturbed, see Figure 2.7. In order to measure the (p,γ) products at the desired low beam energies close to the Gamow-window, the DSSSD was UHV-compatible.
In addition, three X-ray detectors were surrounding the gas jet target at 35°, 90° and 145° with respect to the direction of the orbiting ions to measure the K-REC signature for the precise normalization of the (p,γ) cross section.

The cross section of the ^{124}Xe(p,γ)^{125}Cs reaction has been successfully measured for five different center-of-mass energies between 8 MeV and 5.5 MeV with uncertainties on the order of 10 %. The upper edge of the Gamow-window of this reaction was approached within <100 keV [136] proving the applicability of the method for heavier nuclides in astrophysically relevant energy ranges.

Chapter 3

Ion optical simulations of in-ring reactions

In this chapter, the methodology of the ion optical simulations for the Experimental Storage Ring will be introduced focusing on proton-capture reactions relevant for the recent (p, γ) experiments. As a showcase, the 8 MeV/u dataset of the E108b experiment is evaluated in detail. Later in this chapter, a newly developed technique will be discussed which is proven to significantly increase the measurement sensitivity for the (p, γ) events by over 95%.

3.1 The MOCADI code

In order to better understand the transport of charged particles inside a storage ring, Monte Carlo simulations are a useful tool, such as the MOCADI code developed at GSI [137, 138]. In the code, the ion optical system is implemented in the form of transfer matrices. Sets are available for various experimental facilities worldwide including the Experimental Storage Ring. When running the MOCADI code, multi-dimensional data array can be created and stored in the form of a ROOT file [139], which includes the spatial information of the ions as well as other properties such as their energies, time-of-flights, etc.

In the framework of the current (p, γ) studies, it is sufficient to simulate only a section of the ESR starting from the target until the DSSSD placed at the end of the following dipole magnet. This section includes a quadrupole duplett and the mentioned dipole magnet. The beam pipe, connecting these instruments, is not directly included in the simulation, therefore, the limitation on particle trajectories given by the walls of the pipe are not accommodated for each position, it is represented only by an acceptance window at the start of each ion optical device. This can lead to unrealistic trajectories

primarily in case of multiturn investigations. For the current study, when the most limiting spatial acceptance is given by the particle detector itself, such artifacts can be fully neglected.
The number of simulated ions is user defined and the properties of the ions are randomly generated right before the target section based on a given distribution characteristic for the stored beam. MOCADI is not designed for reaction simulations, but simple two-body kinematics for reactions as (p, γ) or (p, n) can be implemented by using external libraries. The employed routine handles the interaction with the target in inverse kinematics with relativistic treatment. The scattering angle in the center-of-mass system (ϑ) is preserved for each ion, thereby, non-uniform scatterings can be implemented as well. The routine contains no information about the cross section of the reaction. Therefore, when combining multiple reaction channels, the processes need to be scaled. In the following list, the variable input parameters for the MOCADI simulation of the (p, γ) reaction are listed ordered according to their relevance.

- charge state of the beam
  During all (p, γ) experiments the ions in the beam are fully stripped. Hence trajectories due to the electron loss are obsolete. This condition distinctly defines the charge state of the beam as $^{124}Xe^{54+}$ for the E108b and E127 experiments and $^{118}Te^{52+}$ for the E127 experiment.

- ion masses
  Nuclear masses of the ions are calculated for 1st order kinematics by subtracting from the corresponding atomic masses [140, 141] the binding energy of bound electrons [142–144]. In the simulations the mass of the molecular hydrogen target is approximated as the mass of the proton as a necessity to describe correctly the available energy in the center-of-mass system during a nuclear proton-capture reaction. The available energy in the center-of-mass system defines the size of the corresponding scattering cones.

- beam energy
  In the E108b experiment 5 different energies were applied ranging from 8 MeV/u to 5.5 MeV/u, while for the E127 experiment the beam energy was kept at 10 MeV/u. The energy of the beam is controlled by the electrons in the cooler, which compensates the energy loss in the target. The energy uncertainty is defined by the accuracy on the voltage set in the electron cooler device. The

nominal beam energy is set as a reference energy for all the ion optical instrument to preserve the beam.

- detector position
  The detector position is defined by the layout of the storage ring and can be estimated through technical drawings. In the code, the detector can be implemented as a so-called SAVE point where all the properties of the ions are recorded.

- beam emmittance
  A good estimate can be given on the beam quality by using the published data from [145] for 10^5 $^{238}U^{92+}$ ions at 3 MeV/u. Therefore, the beam emittance in the x direction, which is approximated to be equal in the y direction for the simulations as well, reaches $\epsilon = 0.5\,\text{mm·mrad}$ with momentum spread of $\delta p/p = 10^{-4}$ (2σ - value). For simplicity, the beam shape is defined as a uniform distribution in the ellipse defined by the beam emittance and energy spread.

- nuclear structure
  To model the 2nd order kinematic effects, such as the peak shape of the particle distributions within the recoil cone, the population of excited states and γ-cascades after compound reactions need to be taken into account.

An example MOCADI input file for the (p, γ) case at 8 MeV/u including a statistical treatment for the 1st populated state and for the subsequent gamma cascades is given in the Appendix A.

3.2 Modeling the spatial response of the DSSSD

3.2.1 The DSSSD spectra

The DSSSD is placed at 53.5° out of the 60° bending angle of the complete dipole according to technical drawings. The bending angle of the dipole defines the distortion of the scattering cones and will be taken as a fixed value in the simulations. However, the exact x and y positions of the detector relative to the beam at the 53.5° plane is not precisely known and must be calibrated.

At beam energies close to the Gamow window typically two or three different reaction channels contribute dominantly to the count rate on the detector. These are the Rutherford scattering and the (p, γ) and (p, n) nuclear reaction channels.

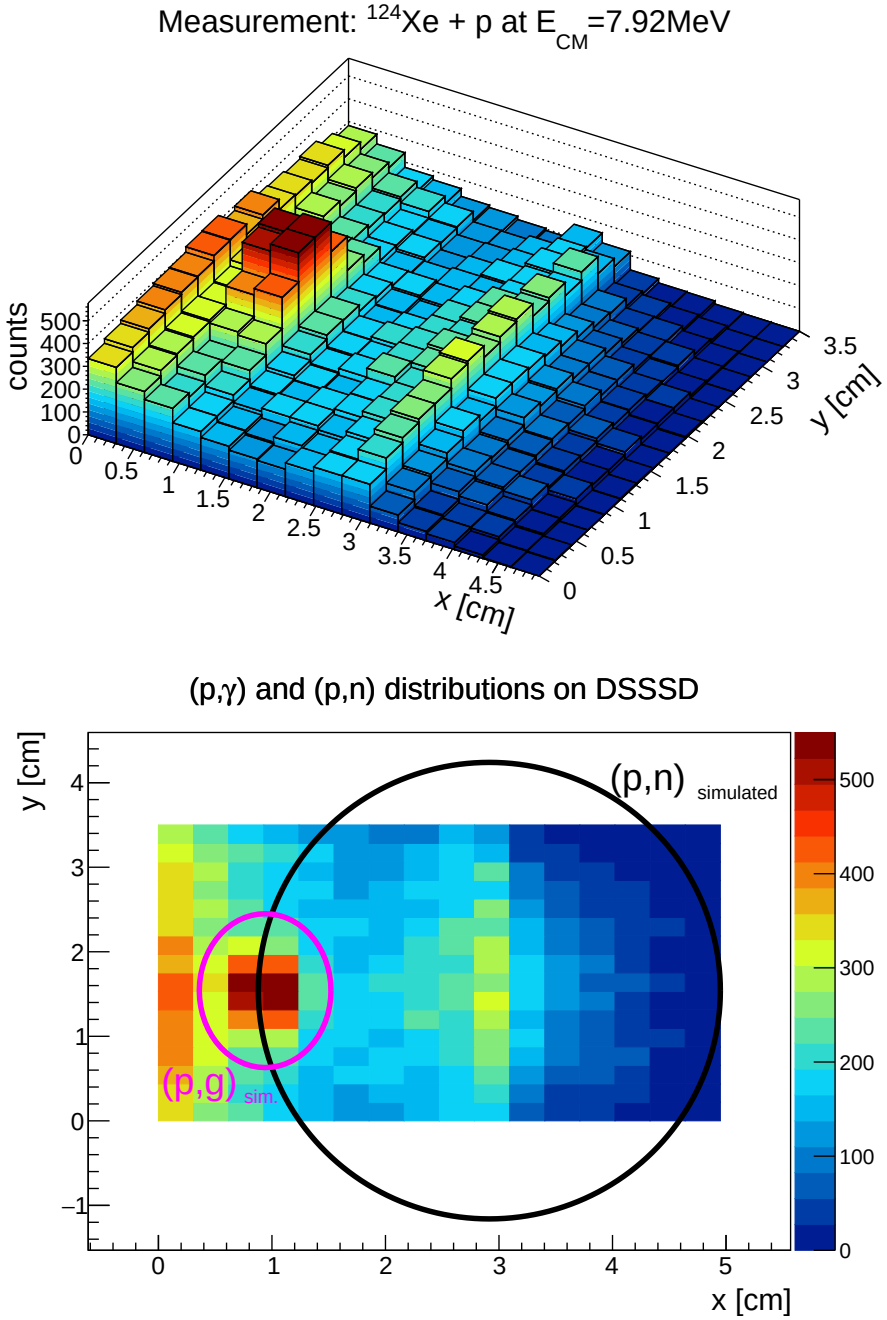

Figure 3.1: The measured detector response in 3D (upper panel) and map (lower panel) views are shown for $^{124}Xe^{54+}$ beam interacting with H_2 target at 7.92 MeV center-of-mass energy. The three main reactions visible are the (p, γ) centered at x≈1 cm, the (p, n) nuclear reaction channel centered at x≈ 2.9 cm, and the Rutherford scattering. The size and the position of the clusters corresponding to nuclear reaction products can be well reproduced with Monte Carlo simulations.

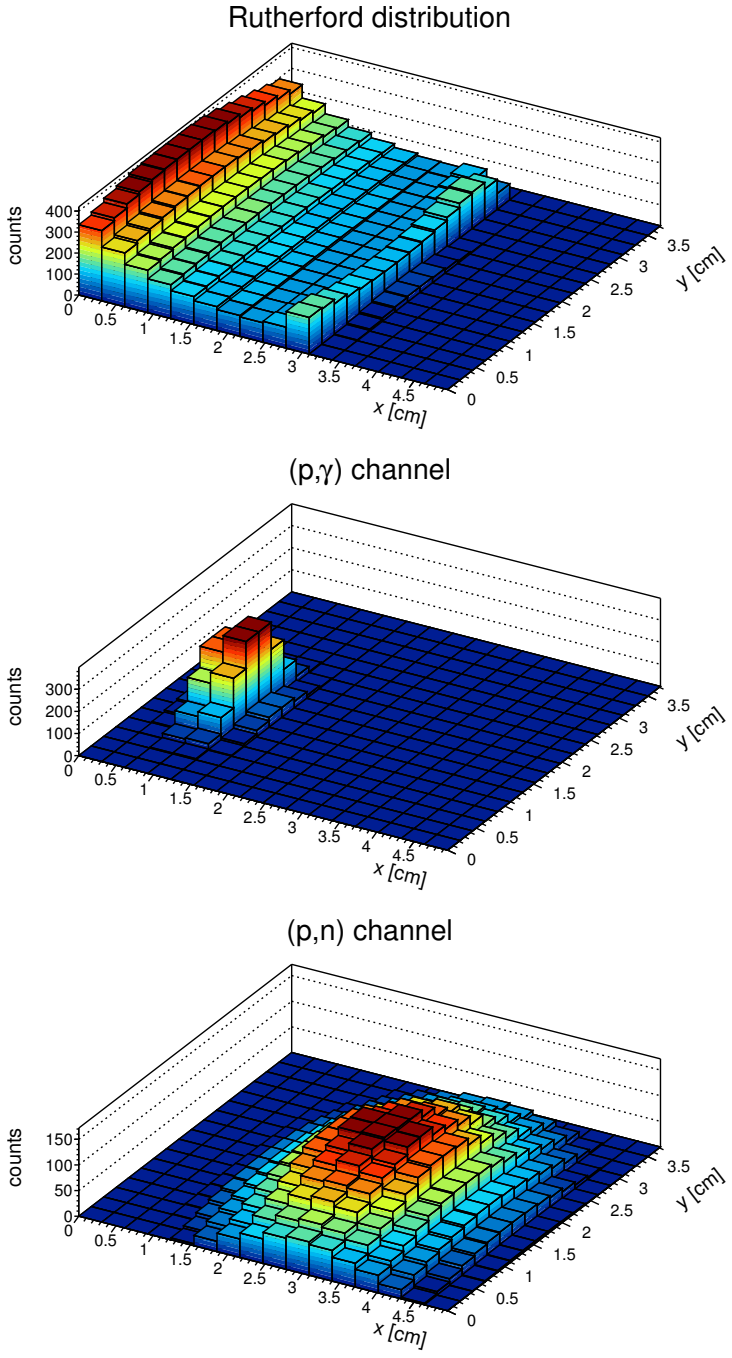

Figure 3.2: The significant processes after the interaction of the $^{124}Xe^{54+}$ beam and the H_2 target at E_{CM} =7.92 MeV are modeled separately and then combined together taking into account the segmentation of the silicon detector. The simulated processes are the Rutherford scattering (top), the (p, γ) reaction (middle) and the (p, n) reaction (bottom).

In addition to these processes, the (p, α) and the (p, p') nuclear reactions can occur as well, however, in both cases the size of the reaction cones exceeds widely beyond the DSSSD. For the (p, α) case, using the TALYS nuclear reaction simulation code [21], the cross section is 40 times less than for the (p, γ) reaction. Taking into account the detector acceptance for every 2400 (p, γ) events occurs a single (p, α) event. In other words, during the whole 8 MeV/u measurement time approximately one (p,α) should have been detected on the complete detector surface which is unrealistic to distinguish from other ion hits. The (p, p') distribution is analogous to (p, α). Although the cross section is about a factor 2 higher than for the (p, γ) case, the scattering cone extends as the Rutherford distribution. Thereby, the reaction does not contribute to the count rate of the DSSSD to a sizeable extent. For the 8 MeV/u measurement data of the E108b experiment the (p,γ), (p, n) and the Rutherford channels contribute dominantly as shown in Figure 3.1 and in Figure 3.2 and will be discussed in detail.

3.2.2 Rutherford scattering

The phenomenon, when the charged projectiles suffer elastic scattering due to pure Coulomb interaction with the target nucleus, is named Rutherford scattering. The cross section of the process is inversely proportional to the squared kinetic energy and has a strong dependency on the scattering angle

$$\sigma_{Rutherford} \sim \frac{1}{E_{kin}^2 \cdot \sin^4(\vartheta/2)} \tag{3.1}$$

while the scattering is symmetric in the azimuth angle (φ) resulting in a strong position sensitivity on the distance between the detector and the stored beam. The events, when the scattering angle is close to 90° are the furthest from the beam axis and form the edge of the scattering cone when the distribution is projected onto the detector plane. This edge at 8 MeV/u underlies to the center of the (p, n) distribution on the detector, while the (p, γ) events are on the rising tail of the elastically scattered ions, see Figure 3.1 upper panel. The Rutherford scattered particles appear as the dominant background for both the (p, γ) and (p, n) events, especially the forward scattered ($\vartheta < 90°$) component. The angular dependency of the Rutherford cross section is implemented in the simulations through a post-weighting process of the MOCADI output.

3.2.3 Position calibration of the DSSSD

When the (p,γ) and (p,n) reaction products are projected onto the detector surface, the size of the simulated distributions and their positions can be fully reproduced within the measurement uncertainties, see Figure 3.1 lower panel. These distributions are used as reference to localize the detector position with respect to the beam and thus, the x and y coordinates of the measurement become defined. However, using the same optical settings for the simulation of the Rutherford distribution shows inconsistency. The sharp edge of the distribution appears shifted by one strip (around 0.31 cm) than the actual measurement along the x-axis. The agreement for (p,γ) and (p,n) events with the simultaneous mismatch for the wider Rutherford distribution might be explained by an imperfect quadrupole focusing in the ring or by its imperfect implementation in the simulation. The elastic scattering cone at the position of the quadrupole magnets is much broader as compared to the ones from (p,n) and (p,γ) reactions. It can thus reach the inhomogeneous part of the field within the quadrupole magnets leading to a distorted distribution. However, further investigations need to be carried out on the beam optics to confirm or disprove any of these assumptions. In the model of the detector response, this effect is taken into account simply by introducing stretching factors in x and y directions for the Rutherford scattered particles only, thereby, stretching or squeezing its distribution.

3.2.4 Background subtraction

In order to precisely measure the cross section of (p,γ) or (p,n) reactions, the Rutherford scattered events should be subtracted from the total spectrum. Firstly, a complete model is fitted to the measurement data consisting of the combination of the Rutherford scattering, the (p,γ) distribution on the detector modeled by a two dimensional Gaussian function and an estimated (p,n) distribution deducted from MOCADI simulations. The parameters of the combined fit include scaling factors for the three distributions, the stretching factors in x and y for the Rutherford distribution, and the width of the (p,γ) distribution. It does not contain the position of the detector since it is already defined through the simulations. While fitting the complete area of the detector with the sophisticated combined model of the significant nuclear and elastic processes a χ^2/NDF $\sim$1.3 was achieved, where the number of degrees of freedom is NDF=243.

After fitting, the Rutherford plus (p,γ) components of the fit are subtracted from the measured histogram to obtain separately (p,n) events, see Figure 3.3. Analo-

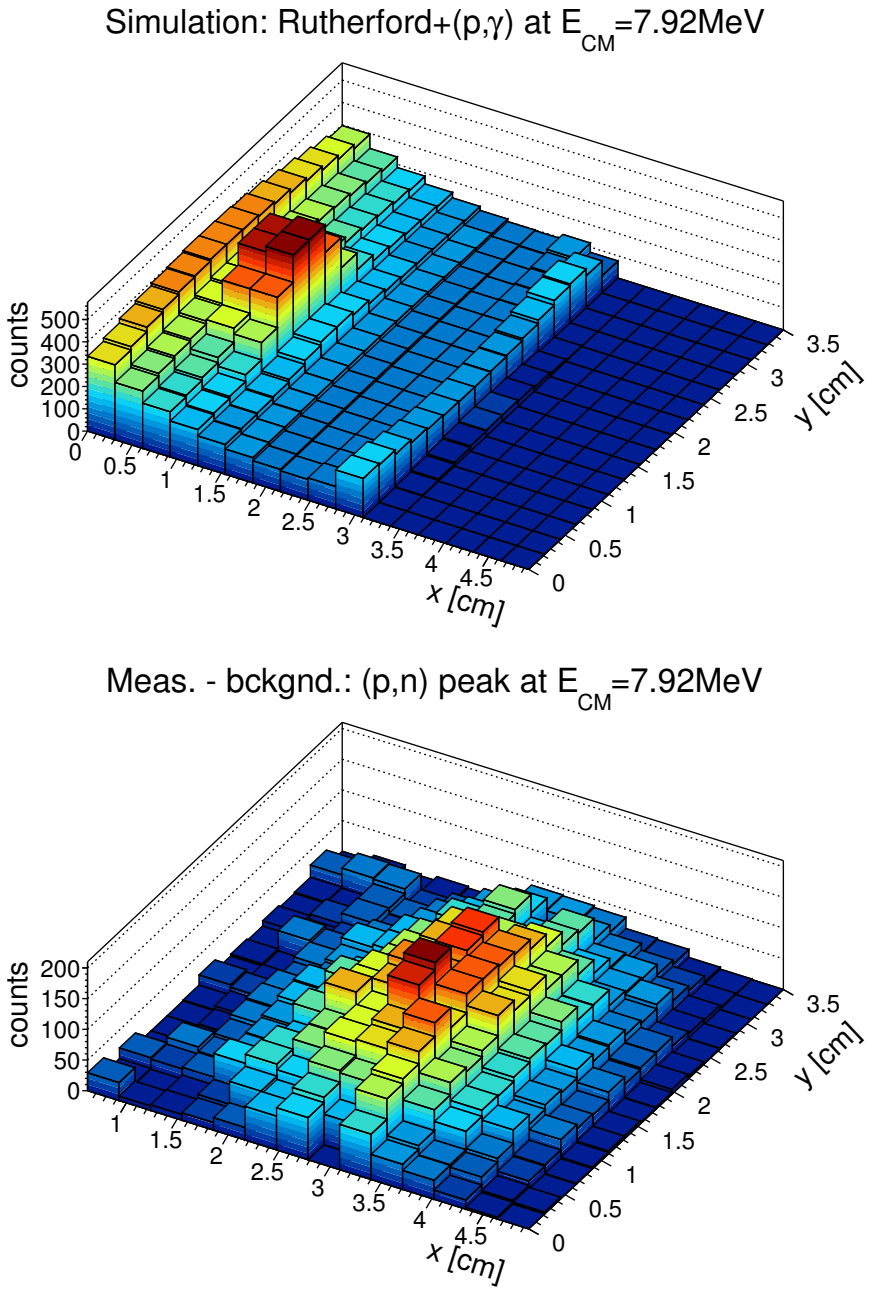

Figure 3.3: Upper panel: the subtracted background consists of the elastic scattering distribution simulated with MOCADI and the (p, γ) distribution modeled as a 2D Gaussian fit. Lower panel: the remaining (p, n) distribution after the background subtraction.

gously, the (p, γ) events can be obtained by subtracting the Rutherford plus (p, n) components. The uncertainty on the number of counts for each bin of the resulting histogram has two components. The statistical uncertainty is given by taking the

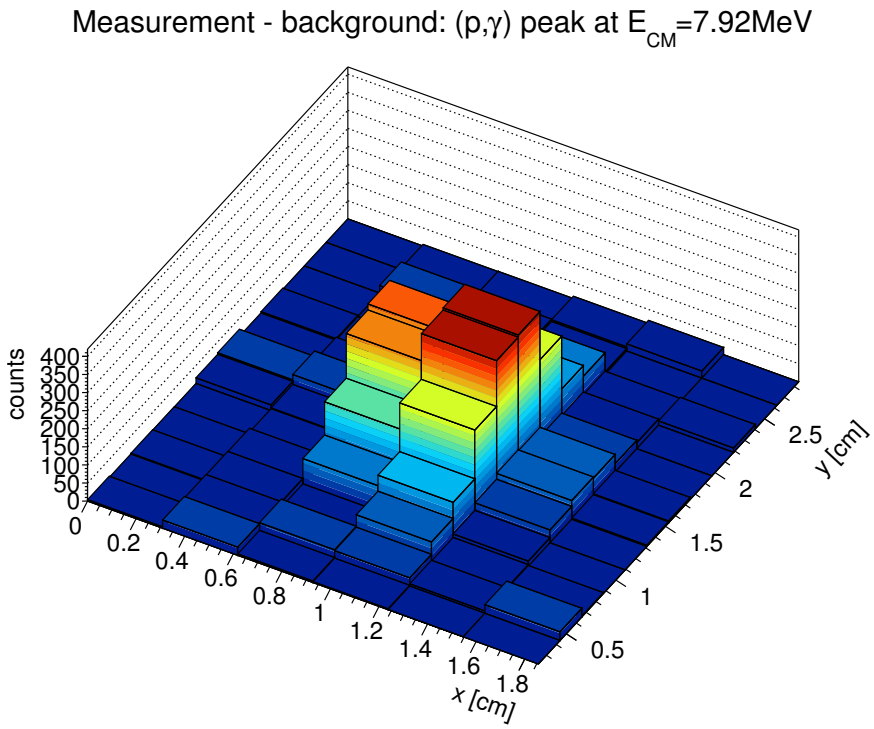

Figure 3.4: The measured (p,γ) peak after global background subtraction. The baseline fluctuates mostly around zero, but in two strips nearest to the beam directly next to the peak a slight increase can be observed in the number of hits. This phenomena can be caused by interactions between the beam and the off-target residual gas, however, its effect is included in the uncertainties.

square root of the number of primarily measured events, as follows conveniently from Poisson statistics. As a conservative and simplistic approach, the systematic uncertainty is defined as the uncertainty of the whole fitted model with 3σ confidence level. The results on the determined cross sections for the (p,n) and the (p,γ) reactions are discussed in Chapter 6.2 and quantitatively given in Table 6.1.

3.2.5 The (p,γ) peak

The main focus of the proton capture campaign at GSI is to measure (p,γ) reactions with high accuracy. In order to undoubtedly capture all reaction products, the detector is positioned to intercept the entire scattering cone of (p,γ) events. The measured (p,γ) hits during the E108b experiment at $E_{CM} = 7.92\,\mathrm{MeV}$ are shown in Figure 3.4.

Since in the (p,γ) reaction the momenta of the emitted γ-rays are relatively small, the process results in a narrow cluster of recoiling ions on the detector surface. The

(p,γ) distribution is typically a few centimeters in diameter on the detector plane, while the diameter of the (p,n) cone exceeds the spatial detector acceptance already at 1 MeV center-of-mass energy above its threshold. To precisely model the shape of the (p,γ) distribution is quite complex. Due to the massless recoiling photons, not only the first populated state after γ emission but also the subsequent γ cascades play a role in the reaction kinematics, see Figure 3.5. In the framework of this thesis the shape of the (p,γ) peak was not modeled by the MOCADI code. The empirical experience shows, however, that to describe the (p,γ) peak a two dimensional Gaussian function is a good approximation. After subtracting the (p,n) and Rutherford background, the number of (p,γ) events has been integrated for the area of the (p,γ) cone on the DSSSD. For the $E_{CM} = 7.92\,\mathrm{MeV}$ dataset the result is $\mathrm{N}^{8\,\mathrm{MeV}}_{^{124}\mathrm{Xe(p,\gamma)}} = 2902 \pm 100_{stat} \pm 117_{syst}$. The statistical error accounts for the measurement uncertainty before background subtraction and the systematical uncertainties are representing the uncertainty of the fitted model. Analogously, the number of (p,γ) events was evaluated for the $E_{CM} = 6.96\,\mathrm{MeV}$ dataset from the E108b experiment. The result is $\mathrm{N}^{7\,\mathrm{MeV}}_{^{124}\mathrm{Xe(p,\gamma)}} = 5827 \pm 112_{stat} \pm 204_{syst}$.
By using the luminosity measurement from [9] and Equation 5.7, the number of (p,γ) counts can be converted into cross section values. The obtained result for 8 MeV/u is

$$\sigma_{^{124}\mathrm{Xe}(p,\gamma)}(E_{CM} = 7.92(1)\,\mathrm{MeV}) = 45.5 \pm 1.6_{stat} \pm 2.8_{syst}\,\mathrm{mb} \tag{3.2}$$

and for 7 MeV/u is

$$\sigma_{^{124}\mathrm{Xe}(p,\gamma)}(E_{CM} = 6.96(1)\,\mathrm{MeV}) = 103.9 \pm 2.0_{stat} \pm 7.1_{syst}\,\mathrm{mb}. \tag{3.3}$$

In Equation 3.2 and 3.3, the systematic uncertainty of the measured cross section contains in addition the uncertainty of the luminosity measurement. The results are in agreement with the published cross section values in [9] and are discussed in the context of the previous (p,γ) measurement at the ESR in 2016 in Chapter 6.2. All cross sections determined in this work are given in Table 6.1.

3.2.6 The (p,n) peak

The size of the (p,n) distribution on the detector increases with the available excitation energy. Already 1.2 MeV above the threshold the (p,n) events occupy the majority of the detector surface extending beyond its frames overlapping even with the (p,γ) peak, see Figure 3.1. The overlap increases the uncertainty of the (p,γ) peak determination and clearly complicates the analysis. Also, the (p,n) spot on the

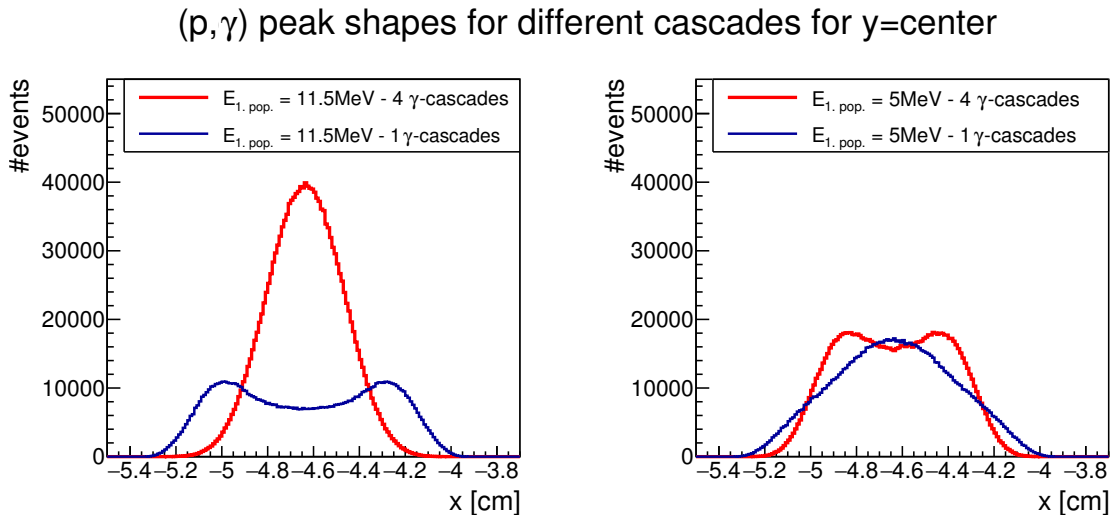

Figure 3.5: The shape of the (p,γ) peak is the result of complex de-excitation processes. The momentum of the recoiling photon is comparable to the momentum of the subsequently emitted photons. For a reliable peak model not only the occurrence of the first populated state after (p,γ) reaction must be known but also the relative strength of the cascades until reaching the ground state. For $\sim$11.64 MeV energy budget at 7.92 MeV center-of-mass energy this treatment would include hundreds of excited states. It is impossible to resolve individual contributions from the measured (p,γ) peak.

detector takes an unfortunate place by being centered near to the hardly reproducible edge of the Rutherford scattering. This leads to highly uncertain smaller regions near to the center of the obtained standalone (p,n) distribution. The number of (p,n) events were obtained first by subtracting the (p,γ) and simulated Rutherford distributions from the measured spectrum. Then, the regions of the (p,n) distribution, which are not covered by the detection area, have been extrapolated. The obtained number of (p,n) counts are $\mathrm{N}^{8\,\mathrm{MeV}}_{^{124}\mathrm{Xe(p,n)}} = 11908 \pm 174_{stat} \pm 127_{syst}$. The statistical error accounts for the measurement uncertainty before the background subtraction and the extrapolation procedure, while the systematical uncertainties are representing the uncertainty of the fitted model.

By using the luminosity measurement from [9] and Equation 5.7, the number of (p,n) events can be converted into cross section values. The obtained result for 8 MeV/u is

$$\sigma_{^{124}\mathrm{Xe(p,n)}}(E_{\mathrm{CM}} = 7.92(1)\,\mathrm{MeV}) = 186.5 \pm 2.7_{stat} \pm 8.9_{syst}\,\mathrm{mb}. \tag{3.4}$$

In Equation 3.2, the systematic uncertainty of the measured cross section con-

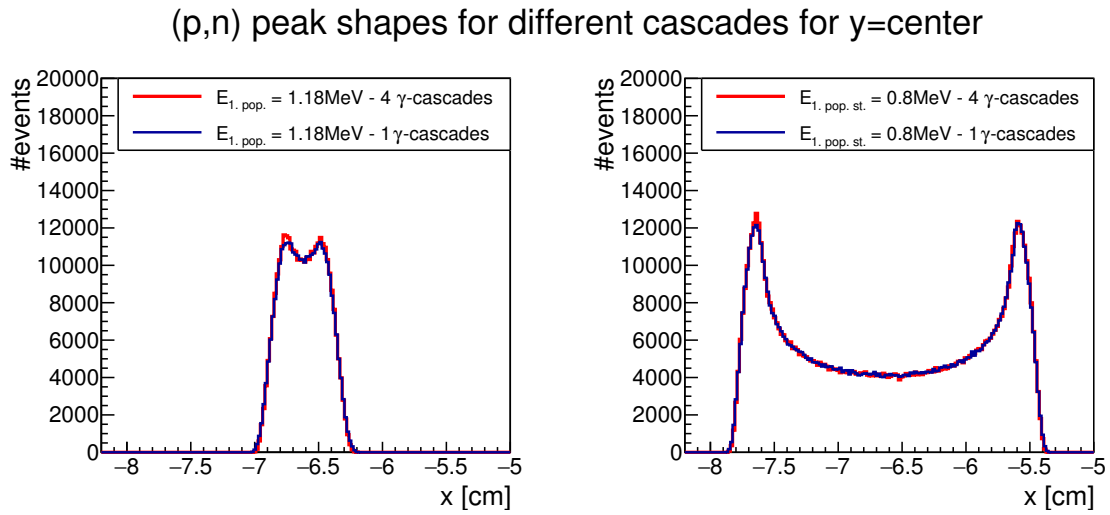

Figure 3.6: Contrary to the (p, γ) peak, the (p, n) peak is defined dominantly by the first populated state after binary neutron emission and negligibly from the subsequent γ-cascades making shape investigations possible.

tains in addition the uncertainty of the luminosity measurement as well. The result is discussed in the context of the previous (p, γ) measurement at the ESR in 2016 [9] in Chapter 6.2. All cross sections determined in this work are given in Table 6.1.

However, the (p, n) distribution also carries within itself an important, advantageous feature. On the contrary to the (p, γ) reaction, the shape of the (p, n) distribution is defined predominantly by the strength of the populated states after neutron emission and not by the subsequent γ-cascades as represented in Figure 3.6. This is due to the fact that assuming the same kinetic energy $E_n = E_\gamma$ the emitting neutron causes a larger recoil as compared to the emitting γ-ray. Therefore, the subsequent cascade of photons cannot considerably change the momentum vector of the recoiling heavy ion, it is already determined by the emitted neutron, see Figure 3.6. This makes, in combination with the modest available excitation energy, the modeling of the (p, n) peak shape feasible. Using theoretical models to calculate the distribution of the binary reaction products is challenging since the states, with the exception of the first few above the ground state, are not well known and have to be treated statistically [146].

In the analysis, the following method was used to measure the occurrence of the first populated state in ^{124}Cs after neutron emission. The available excitation

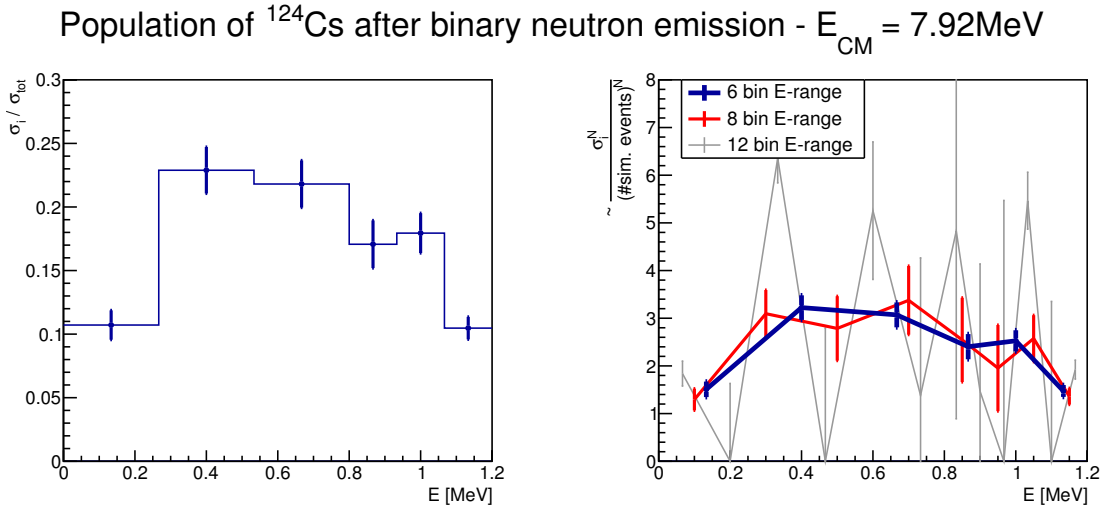

Figure 3.7: Simple-shape models were fitted to the obtained (p, n) distribution. Left panel: the occurrence of the firstly populated states after binary neutron emission are shown for the most stable, N=6 bin model. Right panel: increasing the level density in the models does not necessary lead to more precise description of the peak shape but to fluctuations with increased uncertainty around the 6-bin model. This is understandable if taking into consideration that the radial size of the (p, n) peak on the detector is only 6 bins in x- and 7-9 bins in y-direction, while the number of events in the bins at the edge of the distribution is small.

energy, roughly 1.2 MeV, is distributed into two parts. For the lower 2/3 of the available energy a rough binning is applied with $N/2$ equal sections and the remaining upper 1/3 is also distributed into $N/2$ equally wide bins. The finer division for the upper energy range is needed since the size of the (p, n) cone increases rapidly with decreasing the energy of the first populated excited state. MOCADI simulation is used where the excited state is represented by the energy taken at the bin middle. Then, the excited state decays directly to the ground state of ^{124}Cs through γ-emission. The primary neutron-emission and the following γ-emission is approximated with a uniform distribution for the ϑ and φ angles in the center-of-mass system. The simulated distributions of the ^{124}Xe(p,n)^{124}Cs reaction are concentric on the detector plane but have different sizes. The resulting final (p, n) peak is taken as the sum of all simulated distributions weighted with a fitted strength factor.

The fitting procedure was done for different number of bins N=6, 8, 10, 12. In the left panel of Figure 3.7 Panel left the N=6 case is plotted representing the most stable fit result, while in the right panel the obtained fit parameter values are shown for different bins normalized for the summed number of events. The fits were evaluated

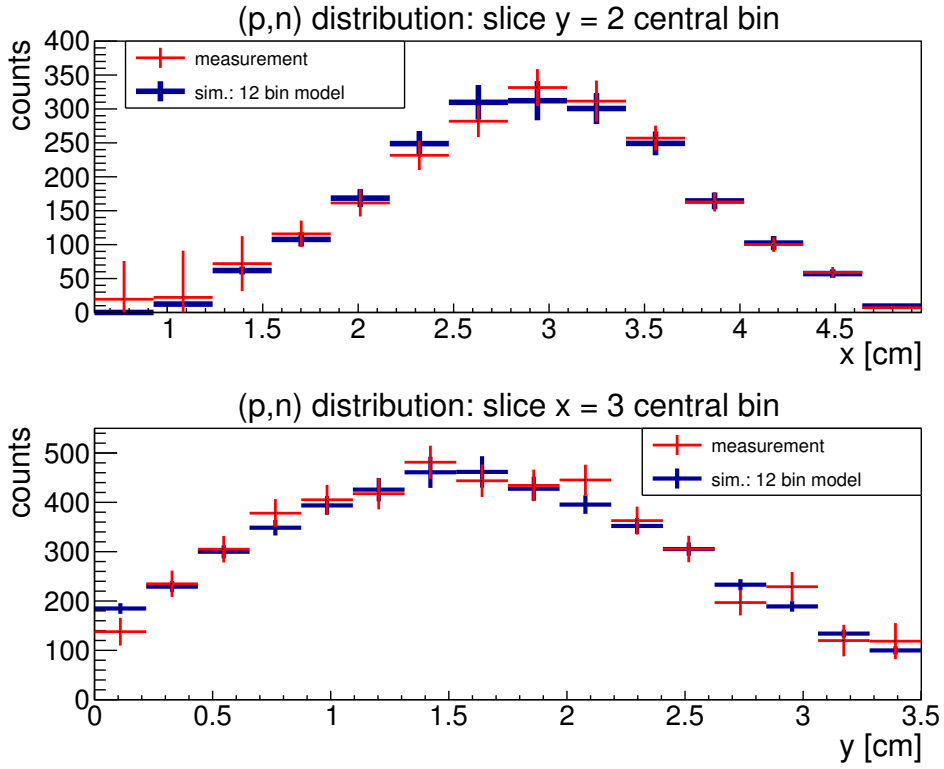

Figure 3.8: A good match ($\chi^2/NDF \sim 1.1$) can be achieved for the fitted shape models assuming different number of excited states. However, a characteristic disagreement can occur for the most central bins in case of a modest distribution of the available energy. For demonstration, here the 12-bin model is shown.

for the area occupied by the (p, n) peak. The model and the measured distribution matches quite well for every fit, especially considering all steps to obtain the pure (p, n) distribution as well the limits of a binned approximation, see Figure 3.8. For all modeled histograms $\chi^2/NDF \sim 1.1$ was achieved, while the number of degrees of freedom (NDF) was between 200-206. However, a characteristic disagreement can occur for the most central region when the energy of the assumed uppermost excited state is not large enough to describe a (p, n) cone with a diameter of 1-2 strip size on the detector. This can be improved when using a finner binning for the upper range of the available energy or with non-equidistant, decreasing bin size towards the maximum. However, the strength parameter of the fits, when using high number of bins, becomes unstable and fluctuates around the result achieved for the N=6 case. This indicates that the details of the shape models of the (p, n) distribution can easily reach the limit given by the position resolution of the used silicon detector. The obtained population data for the N=6 and 8 models are available in Table 3.1.

	population after binary neutron emission			
	6 bin model		8 bin model	
	E [keV]	**population [%]**	**E [keV]**	**population [%]**
1. ex. state	133	0.11 ± 0.01	100	0.07 ± 0.01
2. ex. state	400	0.23 ± 0.02	300	0.16 ± 0.03
3. ex. state	667	0.22 ± 0.02	500	0.15 ± 0.04
4. ex. state	867	0.17 ± 0.02	700	0.18 ± 0.04
5. ex. state	1000	0.18 ± 0.02	850	0.13 ± 0.05
6. ex. state	1133	0.10 ± 0.01	950	0.10 ± 0.05
7. ex. state	-	-	1050	0.14 ± 0.03
8. ex. state	-	-	1150	0.07 ± 0.01

Table 3.1: The spatial segmentation of the DSSSD, used during the E108b experiment [9], provides the opportunity to investigate the distribution of the excited states ^{124}Cs populated in the ^{124}Xe(p,n) reaction. The available energy after neutron emission was divided into two sections containing 2/3 and 1/3 of it. Both sections were subdivided into $N/2$ bins, the energy of the excited states is taken as the bin middle. Here, the results for N=6 and 8 excited states are shown, the populations for both models are normalized to unity.

In summary, when the statistics is high enough, obtaining information about the population of the excited states of the recoiling ions is feasible, but the level of accuracy strongly depends on the spatial resolution of the measured distribution.

3.3 The ERASE technique

From the experiments in the past it is obvious that the signal-to-background ratio for (p,γ) and (p,n) reactions becomes smaller when approaching the Gamow-window. This is caused by the strongly diverging cross sections involved and causes a major sensitivity limitation for the entire proton-capture campaign. This section describes a novel approach, the Elimination of the Rutherford elAstic ScattEring (ERASE) technique to maximize the sensitivity of the method.

3.3.1 Methodology

During the measurement phase a scraper device can be placed in front of the first dipole after the target from the inside direction of the ring. Due to the extension of the Rutherford cone at this point, part of the scattering distribution can be blocked, while leaving the stored and the recoiling ions after (p,γ) and (p,n) reaction undisturbed. The technique is sketched in Figure 3.9. The edge of the scraper can be placed

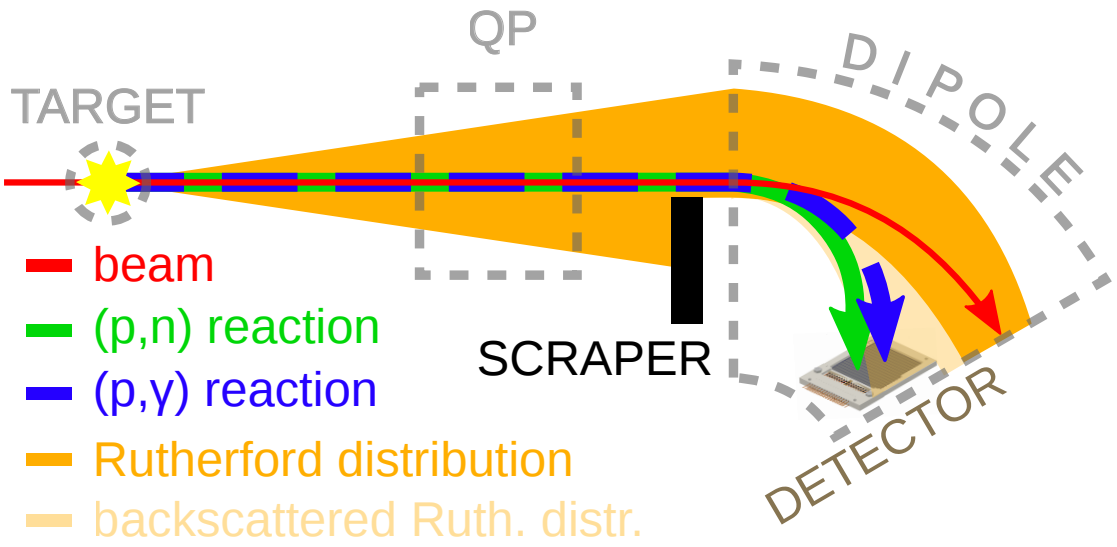

Figure 3.9: The schematic figure of the ERASE technique is illustrated. MOCADI simulations show, that when a scraper device is placed in front of the dipole magnet from the inside with respect to the ring geometry, the dominant part of the background (Rutherford scattering) can be eliminated at the detector position. This improves the measurement sensitivity for the (p,γ) events drastically, >95 % for ^{124}Xe(p,γ)^{125}Cs reaction at astrophysical energies. To avoid secondary scattering from the scraping edge touching the beam, a brush like design in combination with highly polished scraping edges were employed.

sufficiently far from the beam axis to keep a few cm of safe distance from the (p,γ) and even from the (p,n) recoil cones while still effectively blocking the background.

After the partial background truncation, the magnetic field of the dipole twists the Rutherford scattering cone such that only the backscattered particles can reach the (p,γ) and (p,n) clusters at the detector plane. The "twisting" effect can be understood with the help of the diagram on Figure 3.10. The Rutherford distribution, marked with brown color, scatters strongly asymmetrically in ϑ angle and symmetrical along the φ angle, see Equation 3.1. On the left panel, the scraper position is shown, where part of the scattering cone is removed on the inside by the scraper. After the rotational-effect of the dipole magnet, this truncation results to an elimination of the Rutherford scattered events with scattering angle $\vartheta > 140°$at the (p,γ) and (p,n) positions on the detector plane as shown in Panel B. Since the backward scattered events of the Rutherford distribution occur scarcely as compared to the dominant forward scattering component such an exclusion results in a massive, $> 95\%$ sensitivity increase for the (p,γ) events. It should be noted as well, that the truncation of the Rutherford cone happens already along the vertical

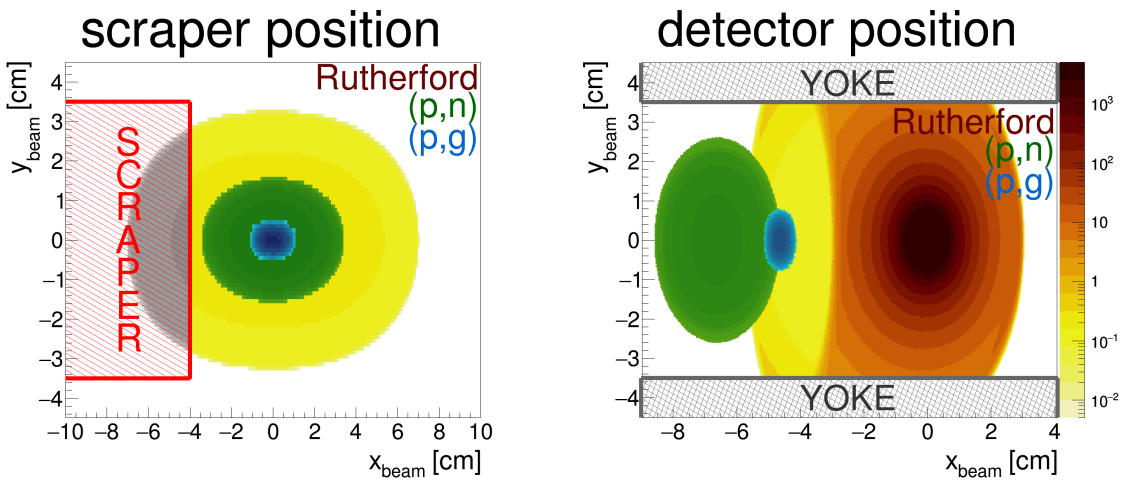

Figure 3.10: Shown are the simulated Rutherford scattering and (p, γ), (p, n) reaction events at the scraper position (left panel) and at the detector position (right panel). The $x < 0$ direction points to the center of the ring, the (x=0, y=0) coordinate corresponds to the stored beam axis. The intensity of all distributions increases from lighter to darker colors. Please note the logarithmic scale for the color steps. The blocked background events are displayed with gray color. When comparing the two panels, the shift of the proton capture reactions towards to ring center and the distortion of the Rutherford cone after traveling through the dipole field are clearly visible. When applying the ERASE technique only the strongly backward-scattered (ϑ >140°) Rutherford events with low intensity can reach the detector thus increasing the sensitivity of the measurement for the (p, γ) events dramatically.

axis (y-axis), $\Delta y_{\text{dipole}} = 7\,\text{cm}$, when the scattering cone reaches the entrance of the dipole magnet. However, the most limiting factor for the elastically scattered particles in regard to their y-coordinate is the spatial acceptance of the detector itself ($\Delta y_{\text{DSSSD}} = 5/\sqrt{2}\,\text{cm}$).

The impressive consequence of the ERASE technique can be represented by the simulated 2D position histogram of the detector, see Figure 3.11. Without applying ERASE the number of the Rutherford events in the (p, γ) peak region is more than the the counts in the peak itself. Using the ERASE technique the number of background events is roughly one tenth of the events in the (p, γ) peak. The principle of the method is published in [147] and its effectiveness was confirmed by the E127 experimental data in 2020, see Chapter 5.5.2.

3.3.2 Requirements on the ERASE design

The scraper device is in position only during the measurement phase, when the target is switched on, but during the beam preparation phase (injection, cooling, deceler-

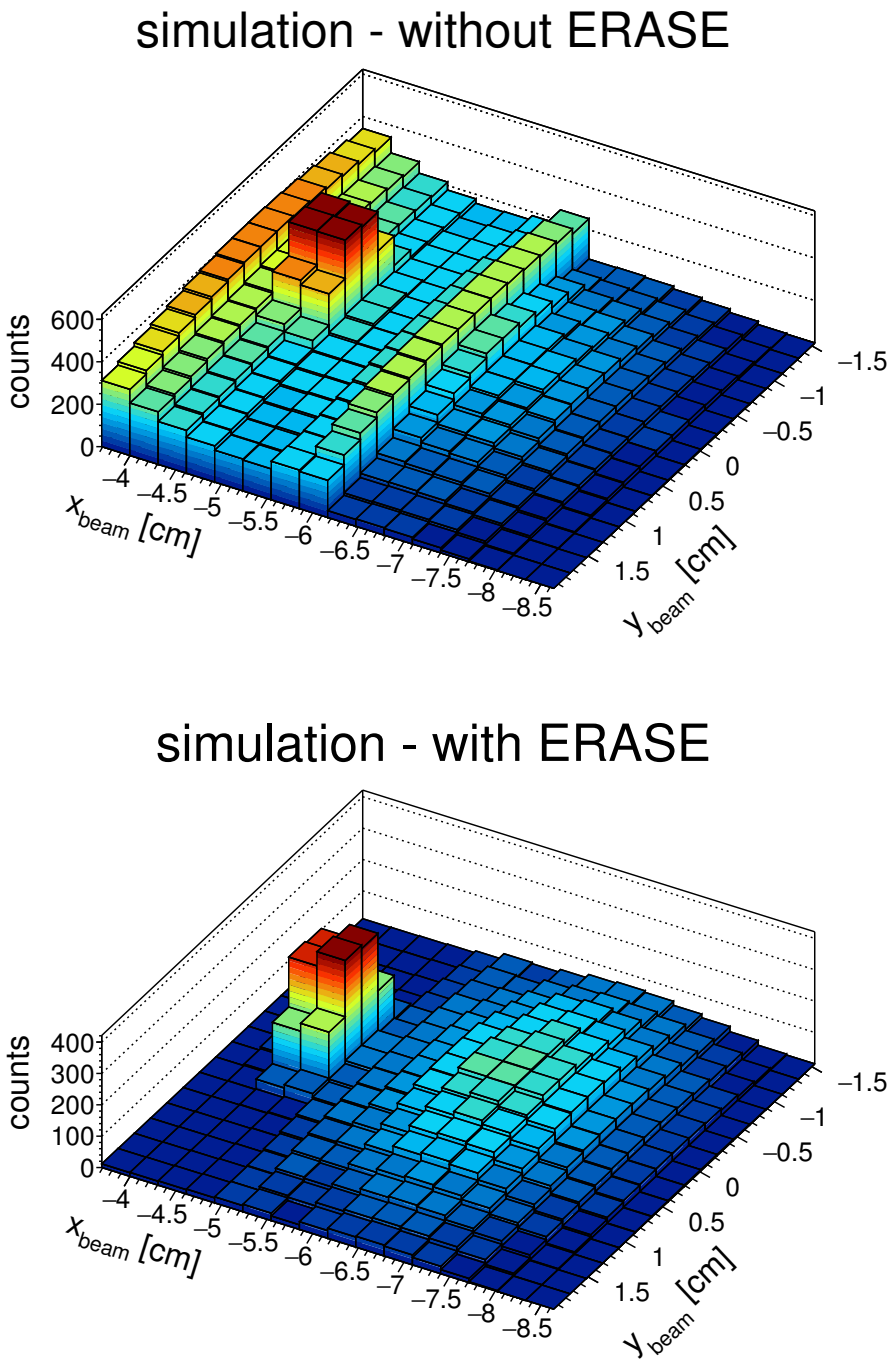

Figure 3.11: The effect of the scraping system is shown by the simulated detector response for the E108b dataset at 7.92 MeV center-of-mass energy. Whereas without the scraping system the Rutherford events are dominantly present at the position of the (p, γ) and (p, n) distributions (upper panel), when the scraper is in use the clusters of the two nuclear reactions stand out nearly background free (lower panel).

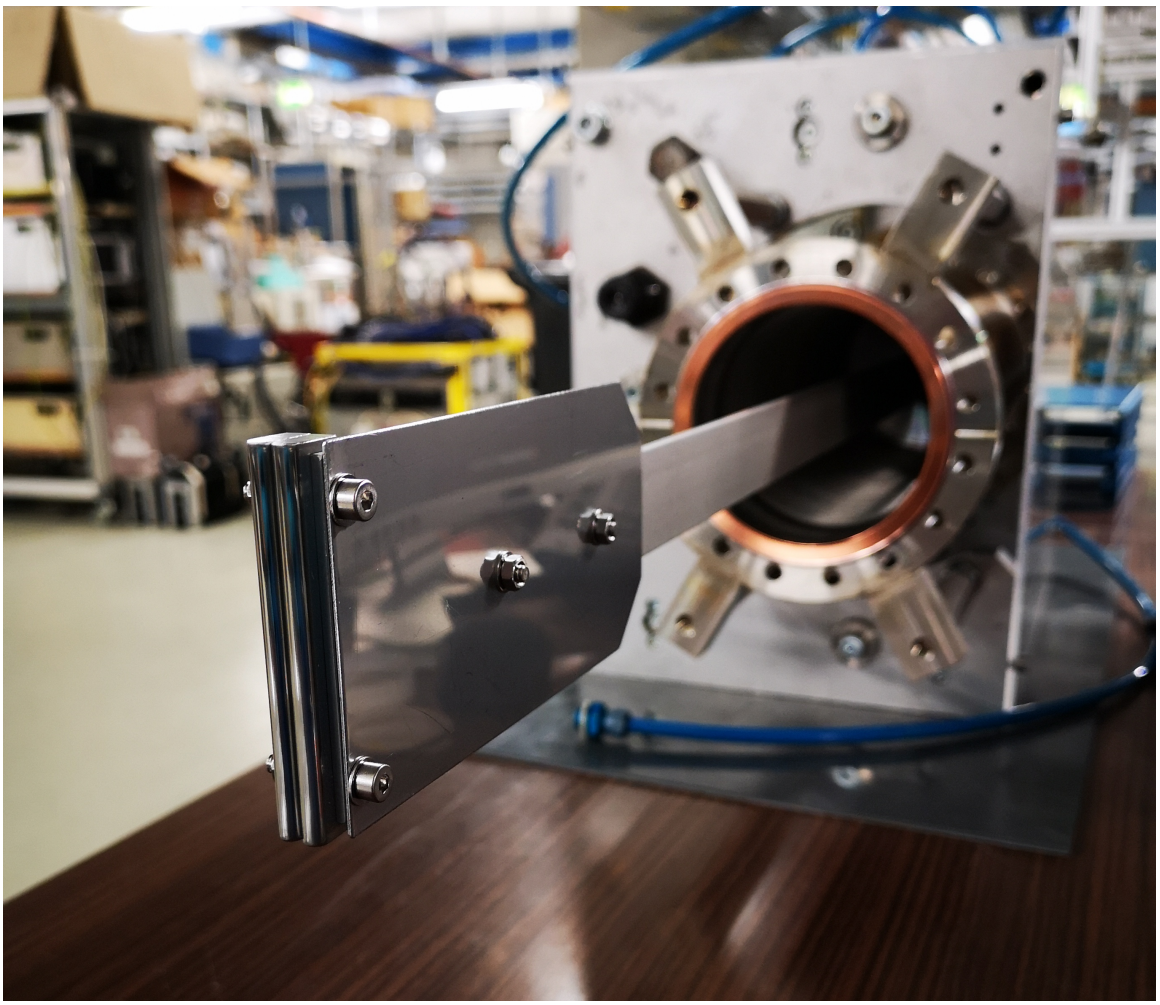

Figure 3.12: The scraping system for the E127 experiment in 2020 is shown with its pneumatic positioning system in the background before the attachment to the ESR. The main elements are a long supporting arm welded to a standard vacuum-flange, a scraping plate and two high-quality scraping edges. All parts of the scraping device were manufactured at GSI.

ation, cooling) the scraper should be kept outside the beam pipe in order to not affect the beam. This requires a fast and precise, automatically controlled positioning system attached to the scraper. For this reason, a fast moving pneumatic piston with position resolution in the sub-millimeter range was attached to a standard ∅100 vacuum-flange connected via a movable bellow to the beam pipe. Inside the vacuum a 675 mm long holding arm was welded to the flange equipped with the scraper device on the other end. The scraper consists of a covering plate made of a 7 cm×14 cm stainless steel sheet with 1 mm thickness, which stops all penetrating ions, and two mirror-polished rounded edges made of stainless steel with 5 mm width in a brush

like structure, see Figure 3.12. The polishing and the structure helps to dramatically reduce the secondary scattering on the edges as it is suggested in [148]. The technical drawings of the scraper devices can be found in Appendix B.

The functionality of the scraper can be further enhanced by the usage of a radiation-hard, position sensitive detector instead of the passive covering plate. Such a detector could provide additional information on the Rutherford scattering cone and thus help to improve the knowledge on the absolute reaction luminosity. for instance segmented solar cells can be an excellent candidate if taking into account their radiation hardness and low costs in combination with their fair energy resolution and segmentation capabilities. The usage of solar cells for heavy ion detection in a ring environment is in focus of current research, pioneer studies can be found in [149].

3.3.3 Complete background removal

As it was shown in the previous sections, more than 95 % of the Rutherford background can be removed by using the ERASE technique during measurement. However, the excellent energy resolution of the used silicon detector gives the possibility to remove the remaining <5 % component [147], thus achieving completely background free measurement of the (p, γ) and (p, n) events. After the scraping of the background, the detector surface can be reached only by strongly backwards scattered particles which have considerably lower energy than the (p, γ) or (p, n) recoils, see Figure 3.13. Therefore, if the detected events can be reconstructed with a relative energy resolution $\delta E/E < 2\,\%$, an offline energy threshold enables the (p, γ) and (p, n) clusters to be completely separated from the Rutherford background.

In the following chapter, the energy calibration of the DSSSD will be discussed, thereby, investigating the feasibility of the complete background-free measurement of the (p, γ) and (p, n) events.

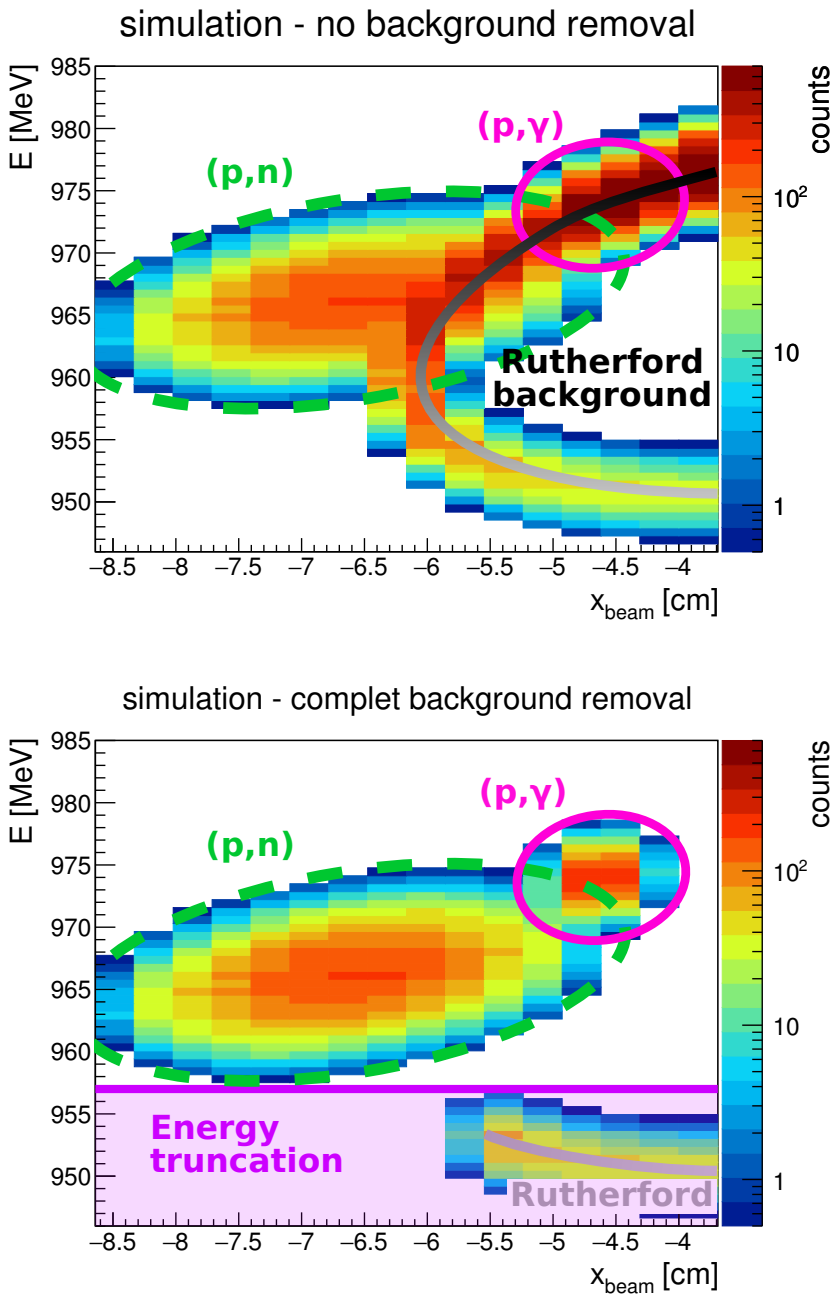

Figure 3.13: Exploiting the energy information from the Si detector can provide additional opportunities for the separation of the events of interest from the background. MOCADI simulations hint that this can lead to complete background removal in combination with the active scraping via a truncation of the low-energy component of the Rutherford background. The condition for the applicability of the method is that the relative energy resolution of the detector shall be below 2 % ($\Delta E/E < 2\,\%$).

Chapter 4

Energy calibration and reconstruction of DSSSD events

Utilizing the energy information of the ions beside their spatial distribution can open new ways to better identify particles in focus of the experiment. Simulations have shown in the previous chapter, that by combining an offline energy selection with an on-line Rutherford background removal, practically background-free measurement can be achieved for the (p, γ) and (p, n) nuclear channel products. In this chapter, the feasibility of this technique will be discussed by analyzing the energy information of the DSSSD for the E108b experiment. Unfortunately, the separation of the (p, n) peak cannot be tested experimentally since the energy information of the DSSSD for the corresponding dataset at E_{CM}=7.92 MeV is partly corrupted. Instead, the data at E_{CM}=6.96 MeV will be discussed in detail investigating the feasibility of the separation between the low-energetic part of the Rutherford scattering and the (p, γ) peak.

4.1 Event types on the DSSSD

The DSSSD is a silicon detector which is on both of its sides segmented into strips perpendicular to each other. When an ion enters into the detector medium, it deposits a part or whole of its energy through ionization. The created charge carriers, the electron-hole pairs, are collected on the ohmic- and the junction side of the detector, respectively $^{124}Xe^{54+}$ ions with kinetic energies below 10 MeV/u can penetrate no more than 50 µm [131, 132] which is around one tenth of the total detector thickness. Depending on the charge collection of the detector segments the energy-reconstruction of the ion hits should be treated differently. Two main categories will be investigated in the following:

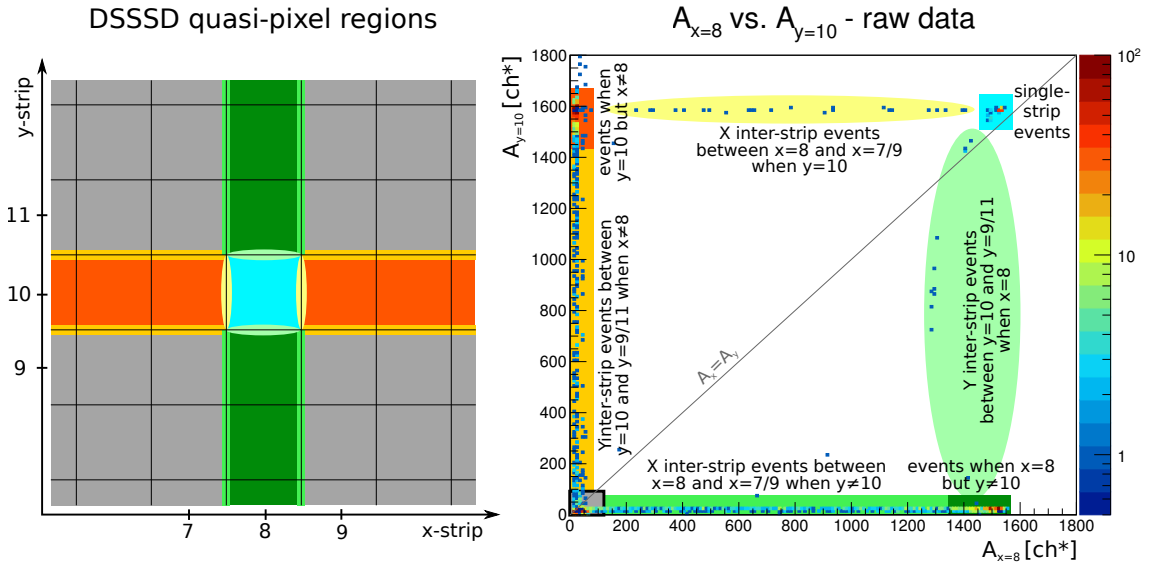

Figure 4.1: Energies of the registered events for strip x=8 (back side) are plotted against strip y=10 (front side) before any selection or calibration. In the figure, based on the location, the event categorization can be approximately performed. For details please see text.

- single-strip event: All charge carriers generated by an incident ion are collected by only one strip on both sides of the detector in coincidence. The charge collection of these strips is complete, both strips measure the same deposited energy. The signal from other detector segments can be neglected.

- inter-strip event: When the trajectory of the ion inside the detector intersects the electric fields of two adjacent strips, the generated charge carriers become shared asymmetrically between the two strips, both segments measure a significant part of the deposited energy in coincidence. Therefore, for energy reconstruction the signal of both adjacent strips should be taken into account.

In addition to these main categories, so-called double inter-strip hits can also occur, when the collection of the generated charge carriers is shared on both sides. However, double inter-strip events contribute only on the order of one percent to the total number of events. Therefore, in this study, they are excluded from the energy reconstruction.

The types of the DSSSD events are demonstrated in Figure 4.1. The pixel map of the DSSSD is schematically shown in the left panel, while in the right panel the uncalibrated energy of all events registered for the x=8 strip (back side) is plotted

against the y=10 strip energy (front side). The same type of events are marked with the same colors and shapes on both diagrams. In the energy plot, for the case of the full charge collection of strip x=8 and y=10, in the top right corner, the group of single-strip events can be found indicated by a cyan shade. Since the energy information at this step of the analysis is not yet calibrated, the signal amplitudes are slightly different for the same event. The yet missing calibration is expressed on the axis units by an asterisk. The single-strip events typically correspond to ion hits in the middle region of a pixel, although the border of the inter-strip region is not identical to the geometrical segmentation of the DSSSD [150].
When moving away from the single-strip region along the A_x-axis, events can be found with decreasing amplitudes for the x strip but nearly constant amplitudes for the y strip. The trend can be followed until the A_x=pedestal region, where a large group of events can be found (region in orange). This group corresponds to all single-strip or to all x inter-strip events when y=10 but $x \neq$8. It represents basically the projection of the y=10 strip events (without the y inter-strip regions) to the y-axis outside x=8 and its x inter-strips regions. The events on the trend-line between the peaks correspond to charge sharing between strip x=8 and its neighbors, these are the so-called x inter-strip events (yellow region).
Analogously, events in the peak at the $A_x \approx$1550 ch* and A_y=pedestal are the single or inter-strip events for the original x=8 strip when y$\neq$10 (dark green color). The events between this peak and the single-strip region are the y inter-strip events of the y=10 strip and its neighbors (light green color). The non-linearity of these events is a well researched phenomena and is discussed in Chapter 4.4.
Events in the pedestal peak (gray color) are the ion hits corresponding to strips for which $x \neq$8 and $y \neq$10.

The single-strip events can be clearly assigned to a pixel of the DSSSD, but for the inter-strip events, which are distributed randomly between adjacent strips both in the geometrical and in the energy aspects, a selection criteria is required to avoid the distortion of the DSSSD spatial spectrum by double counting of certain hits. In the following, the events are assigned to a strip on each side (to a pixel) where a signal with the highest amplitude among all detector segments on the same side is measured. This selection method leads to a natural separation between inter-strip hits about at the half of the total deposited ion energy. However, it should be highlighted that such a comparison between the signal of two different strips is only possible when their

scales are matched. This can be accomplished by an intrinsic energy calibration of the DSSSD strips.

4.2 Gain matching

All segments on both sides of the DSSSD are read out as individual channels. Therefore, to use the energy information it is necessary to calibrate each segments of the detector. If an absolute energy scale is not determined, but the signal of different segments are on the same scale, therefore comparable, is called an intrinsic energy calibration. By realizing gain match between the strips of the DSSSD, a relative energy calibration can be achieved. It should be noted, that this relative energy calibration can be realized for data sets only when the ion detection of the DSSSD and the electronic response does not show significant decrease or variations over time, thus ensuring a non-varying dependency between the amplitude of the detector signal and the energy of an ion hit. Such variations in the signal amplitude can be caused by radiation damage of the silicon lattice, or instabilities in the applied bias voltage, etc. .

The here discussed gain matching calibration method is based on [151] and only its main steps are introduced. The method assumes a linear dependence between the response of the front and back side segments. The condition is fulfilled for the single-strip events but not applicable for inter-strip events. As it is visible from Figure 4.1, the events recorded for the energy map of an x and a y strips form a complex structure. The selection of the calibration events is not trivial. As a first step, the main goal is to select as many single-strip events for a pixel region as possible simultaneously strictly filtering out cases of charge sharing which would give an unwanted bias to the calibration. Contrary to mono-energetic studies such as in [151, 152] or micro-beam studies such as in [150], when using a heavy ion beam with an internal target in a storage ring environment, wide-spread, continuously distributed, overlapping processes shroud the area of the DSSSD with varying energy. Filtering of single-strip events cannot be accomplished during such an experiment, only with the employment of an offline selection. For this, the following procedure is used. Every event on the DSSSD above the noise level is associated to a pixel (x, y) whose intersecting strips detect the highest signal. Although, the scales of different strips are not yet matched at this point, the problematic energy regions are eliminated in the later phases of the process. In coincidence, the signal of the adjacent strips, $x\pm1$ and $y\pm1$, is recoded as well. In case of a single-strip event at the pixel (x, y), the

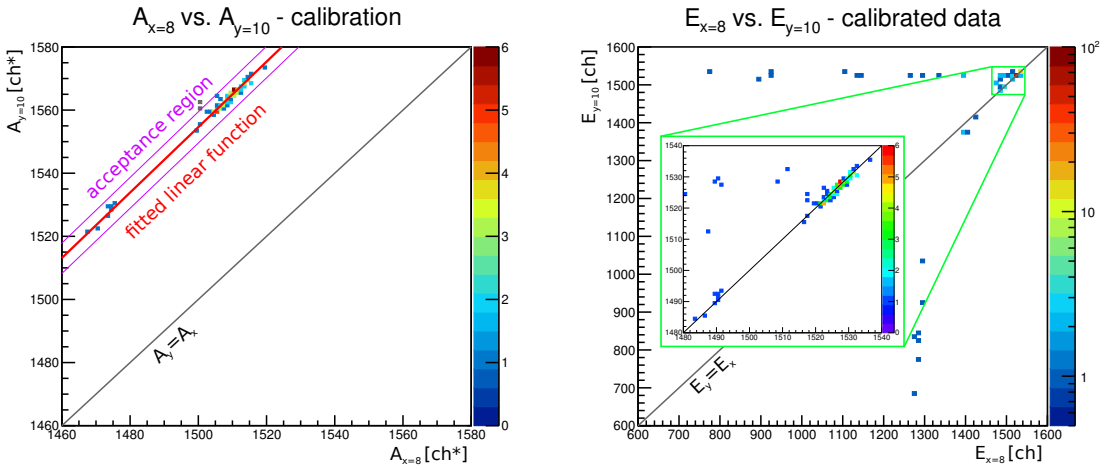

Figure 4.2: Left panel: the selected single-strip events for the gain matching calibration. The events are fitted with a linear function. The slope of which is used to find the gain parameters of individual strips. Right panel: the events associated to the pixel (8,10) after the gain matching calibration.

adjacent $x\pm1$ and $y\pm1$ strips must have a signal in its pedestal peak due to the lack of charge sharing. Due to the rough binning of the pedestal region, the baseline fluctuations cannot be precisely measured. To safely select only single-strip events, the pedestal peak region is therefore rather narrowly confined, which eventually reduces the set of the single-strip events selected for the calibration. As a phenomenological observation, the limits of the pedestal region are selected as the most probable value of the peak (MPV) $\pm$ 2 bins, which is equivalent to around $\pm3\sigma$ width of the peak. These borders function well for most of the inner strips, however, in the case of the most outer strips an additional noise component is present. In order to secure the calibration event selection, an extra limit is given for the amplitudes measured within the original pixel: events, which deviate from the uncalibrated trend-line on the A_x vs A_y plot by more than $\pm5\,\sigma$ of the expected energy resolution of the DSSSD, are treated as outliers, see left panel of Figure 4.2. In addition, events with less than 80 % of the total ion energy are removed to filter out the non-linear y inter-strip events that cross the A_y =A$_x$ line at low A_y values.

In the calibration method of [151], a linear correlation is assumed between the strip signal and the deposited energy. The study shows that a significantly better calibration can be obtained when a two parameter linear fit (slope and offset) is carried out instead of a single parameter fit (slope). In the current study, only one parameter (slope) is fitted, but all pedestal peaks are shifted to (0,0), thus eliminating the

need for an additional offset parameter in the linear fit. Then, the linear connection between the signal and energy can be written for an x strip as

$$E_x = s_x A_x \tag{4.1}$$

and for a y strip as

$$E_y = s_y A_y, \tag{4.2}$$

where s_x and s_y are the calibration coefficients (slopes) for the xth strip on the back side and the yth strip on the front side, respectively. Since the charge collection of other channels is negligible, both sides measure the same deposited energy,

$$E_x = E_y = E. \tag{4.3}$$

With help of Equations 4.1, 4.2 and 4.3 the signal amplitudes of the strips on each side can be related to each other by

$$A_y = S_{yx} A_x \tag{4.4}$$

where S_{yx}=s_x/s_y. Its uncertainty, ΔS_{xy}, can be determined experimentally by fitting the calibration data presented on the A_x vs A_y plane, see left panel in Figure 4.2. By using (N_x· N_y) slope parameters, the set of (N_x+N_y) calibration coefficients $\{s_x, s_y\}$ for all strips can be determined which reproduces best the set of the measured slopes $\{S_{xy}\}$. This can be done by minimizing the following chi-squares estimate

$$\chi^2 = \sum_{y,x} \left(\frac{S_{yx} \; - \; s_x/s_y}{\Delta S_{yx}} \right)^2. \tag{4.5}$$

The minimization is performed by applying the MIGRAD alogirthm from the ROOT Minuit package [153–155]. Since it is a relative calibration, for obtaining only one solution of Equation 4.5, one arbitrarily chosen reference coefficient needs to be fixed. Following the common convention, $s_{x=1} = 1$ was employed.
With the introduced calibration, a $\chi^2/NDF = 0.978$ was achieved for the U_{bias}=-60 V dataset at E_{CM}=6.96 MeV from the E108b experiment.
After finding the best set of calibration coefficients, the DSSSD signals can be expressed on the scale of the first x-strip with units of *ch.* using the current parameter fixation. The gain-matched events associated to pixel (8,10) are demonstrated in the right panel of Figure 4.2.

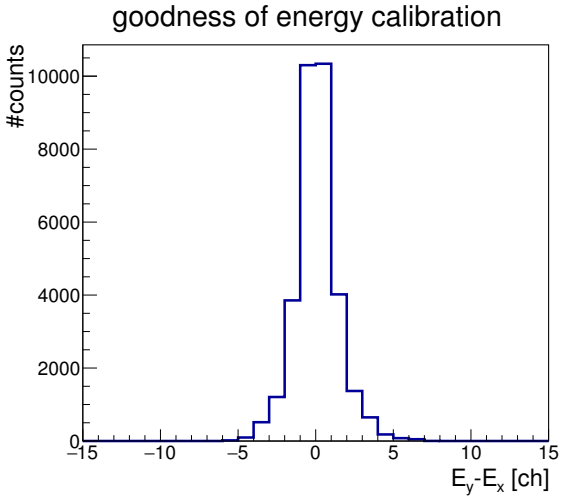

Figure 4.3: The energy resolution of the DSSSD can be caracterized by subtracting the energies measured on the front and back sides for each event after a successful gain matching calibration. For details please read the text.

After matching the gain of the strips, the energy of the single-strip events becomes reconstructed and no additional processing is required. It is important to highlight that the set of single-strip events is not identical to the set of the calibration events, the former group contains the latter one. There are many ways to select single-strip events. Mostly this is done by setting an arbitrary lower limit for the measured mono-energetic events like in [156]. In this work, similarly to [152], events are accepted as single-strip events, if after the calibration the $E_y = E_x$ condition is satisfied within 5σ.

The goodness of the minimization process and, therefore, the energy resolution of the DSSSD can be characterized by the following procedure. By subtracting E_x from E_y for all single-strip events, a peak appears centered at zero in case of a successful calibration. This is demonstrated for the example dataset, see in Figure 4.3. Following the interpretation of [151], the width of the peak characterizes the relative energy resolution and can be expressed as $FWHM = \sqrt{(\Delta E_x)^2 + (\Delta E_y)^2} \approx \sqrt{2} \cdot \Delta E_{s.s.}$. Therefore, when using an averaged $E_{s.s.} = (E_x + E_y)/2$ value for the energy of the single-strip events, the uncertainty of the measured energy deposition reduces to $\Delta E_{s.s.}/\sqrt{2} = FWHM/2$. Taking into account, that the total ion energy is around 1530 ch, the relative energy resolution of the single-strip events is below 0.1 %. This is an excellent energy resolution for a silicon detector employed for heavy ion measurements. However, this value characterizes only the energy resolution of the detector and its electronics but it does not take into account the energy uncertainty

of the beam and other effects, caused for example by the longitudinal extension of the target, the beam, etc.

4.3 Applicability of an energy threshold for the single-strip events

The main goal of the DSSSD energy calibration is to realize a separation between the (p,γ) peak and the back-scattered Rutherford events, which remain present even after applying the ERASE technique, see Chapter 3.3. Since after the calibration the strips are gain matched, the averaged energy of the single-strip events can be studied as a function of the horizontal axis of the DSSSD i. e. the x coordinate. The corresponding plot is presented for the U_{bias}=-60 V dataset of the E108b experiment at E_{CM}=6.96 MeV on the upper left panel in Figure 4.4. The main distributions are the Rutherford scattering reaching until roughly the $15th$ strip of the DSSSD and the (p,γ) peak centered at the $7th$ strip, corresponding to E_{avg} ≈1526 ch. In addition, a small (p,n) cone at the upper end of the Rutherford distribution can be distinguished. However, the (p,n) distribution is not sufficiently intense to draw any reasonable conclusions. Therefore, they are excluded from further analysis. Some background contribution was also detected on the first five strips of DSSSD with energies slightly above the forward-scattered Rutherford events, which matches to the pattern of events recorded when the target was switched off.
On the $1st$ strip, the lower deviation from the forward-scattered Rutherford events at ∼1520 ch indicates that this particular strip requires a more strict single-strip event selection. The event categorization is difficult in particular for the most outer strips, where irregular energy detection was recognized for some cases. However, for the (p,γ) region, within strips 5-10, such behavior was not observed.
In order to characterize the effective energy resolution of the DSSSD during the experiment, the Rutherford scattering and the (p,γ) reaction were simulated and fitted to the measured distributions based on the spatial information of the detector as introduced in Chapter 3.2. The energy information of the fitted distributions was simulated by the MOCADI code. The simulation includes a realistic energy spread of the beam, but other energy blurring effects, such as the longitudinal size of the beam and target, are not included. In order to match the simulation to the actual measurement, the simulated distributions was broadened with a Gaussian kernel along the energy axis by $2.5\times\Delta E_{s.s.}$. The cause of the difference is not well understood. The simulated distributions after Gaussian broadening are shown in the right panel of

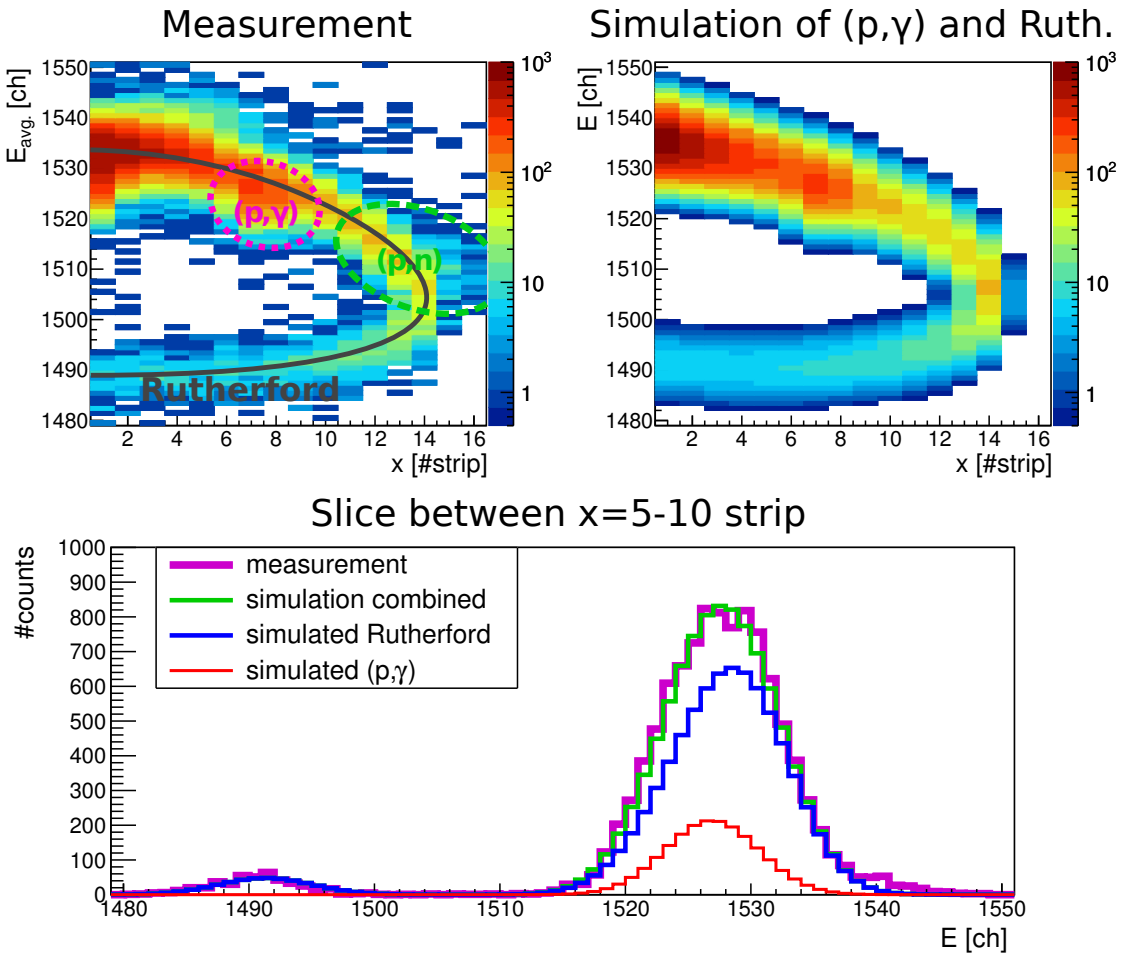

Figure 4.4: The averaged energy of the single strip events is shown as a function of the horizontal coordinate x of the DSSSD. The contributing distributions are the Rutherford scattering and the (p, γ) peak, but other processes with low statistics such as the (p, n) cone can be recognized as well. The separation between the back-scattered Rutherford events and the (p, γ) distribution is achieved.

Figure 4.4, the comparison between measurement and simulation for the strips 5-10 and the simulated components of the distribution are shown in the bottom panel. The effective energy resolution remains in the order of the excellent $\Delta E/E \approx 0.25\,\%$, which is eight times lower than the actual criteria for truncation, $\sim 2\,\%$, see Chapter 3.3.3. The energy separation between (p, γ) and backscattered Rutherford events is achieved.

Despite the promising achievements of the method, the main drawback is that only a part of the whole dataset can be the subject of the energy reconstruction, thereby reducing the amount of the measured events. For the complete E_{CM}=6.96 MeV dataset

from the E108 experiment, the recognized single-strip events constitute ∼70 % for the introduced selection method.

4.4 Extension of the energy reconstruction

After proving the applicability of the energy separation for the single-strip events, it is beneficial to extend the method to the inter-strip events. For this purpose, two approaches can straightforwardly be realized.

The first, hardware based, method is to increase (if possible) the reverse bias voltage of the silicon detector. For this reason a U_{bias}=30 V and a U_{bias}=60 V datasets were studied. The increased applied voltage causes higher electric field within the depleted region of the silicon detector. In higher field the generated charge clouds becomes smaller, which leads eventually to a reduced number of inter-strip events. The effect clearly manifests in the difference between the event type ratios between the two datasets. Employing the same selection criteria, for 30 V bias voltage the ratio of the single-strip events was obtained to be ∼66 %, while for the 60 V bias it reached 73 %. Higher bias voltage can increase even further the proportion of single-strip events.

The second, software based, possibility is to extend the event reconstruction to the inter-strip events. The inter-strip effects in a silicon detector have been widely researched [150, 152, 156–158]. As for the single-strip events, the amount of the inter-strip events is basically a matter of definition. In this study, the inter-strip events are identified by investigating the signals of the adjacent strips to a central pixel. If the induced signal in the adjacent strip is outside of its pedestal peak with more than ±4 bins (equivalent to about ±5σ), it is considered as an inter-strip event for this particular strip.
It is important to differentiate between front side (y inter-strip) and back side (x inter-strip) events. For x inter-strip events, the amount of generated charge by the incident ions does not differ to the single-strip case [150, 152], a complete charge collection is realized by the three involved strips. The full energy signal of the incident particle can be reconstructed simply by summing the charge collected by the two adjacent strips in coincidence after the gain match, $E_x + E_{x\pm1}$, or by using the energy measured on the front side E_y. The effect can be seen from the left panel of Figure 4.5, where the calibrated energy of the x=7 strip is plotted against the energy of

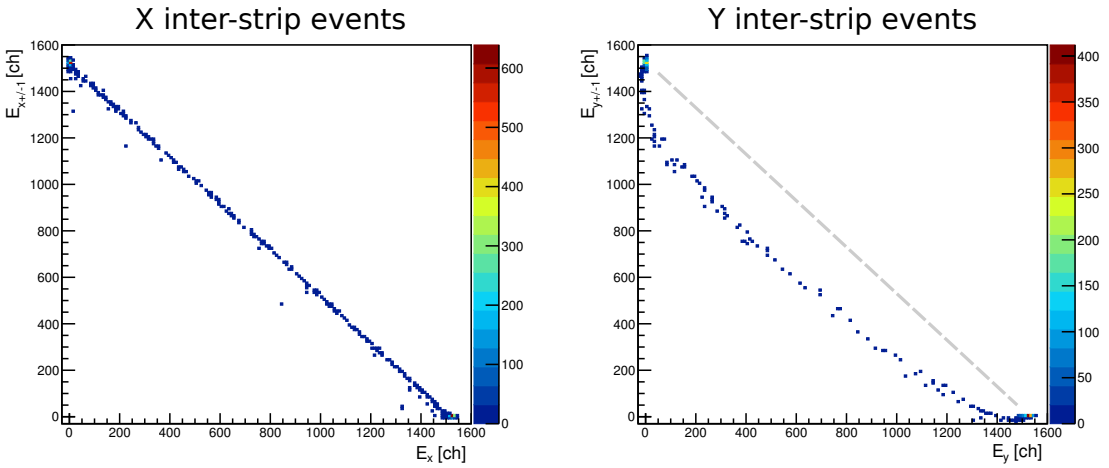

Figure 4.5: The energy measurement of the inter-strip events on the two sides of the DSSSD differs fundamentally when the incident ions are stopped within the detector medium [150, 152, 156–158]. The energy of the x inter-strip events can be reconstructed simply by summing up the signal of the fired adjacent strips in coincidence (left), while in the case of y inter-strip events an energy defect is present (right). For detailed explanation, please see text.

its neighboring strips in coincidence. The peaks at $E_x \approx E_{x\pm1} \approx 1530\,\text{ch}$ consist of single-strip events when no charge sharing occurred. The x inter-strip events are situated between the single-strip peaks on a straight line.

In the case of y inter-strip events, a non-linear energy defect appears for the summed signal of the two adjacent strips in coincidence. This effect can be explained in the framework of the model proposed by Yorkston and collaborators [157]. Briefly, in the inter-strip region a local modification of the electric field is present due to the SiO_2 layer of the DSSSD. When the incident particle travels through this region, so-called opposite polarity signals are induced leading eventually to a deficit in the summed energy. It should be noted, that the phenomenon can be observed also for back side inter-strip events, when the ion energy is high enough (>38 MeV/u for $^{124}Xe^{54+}$ beam [131,132]) to punch through the complete detector medium [152]. The y inter-strip events are shown for strip y=7 on the right panel of Figure 4.5. With the setup of the E108b and E127 experiments negative polarity signals were not recorded. It is clear that the trend-line massively differs from the backside case, a non-linear energy defect is present for the y inter-strip events. The energy reconstruction of these events is not impossible [150], and has to be omitted. Other interpretations of the inter-strip effects can be discussed in the framework of the Shockley-Ramo

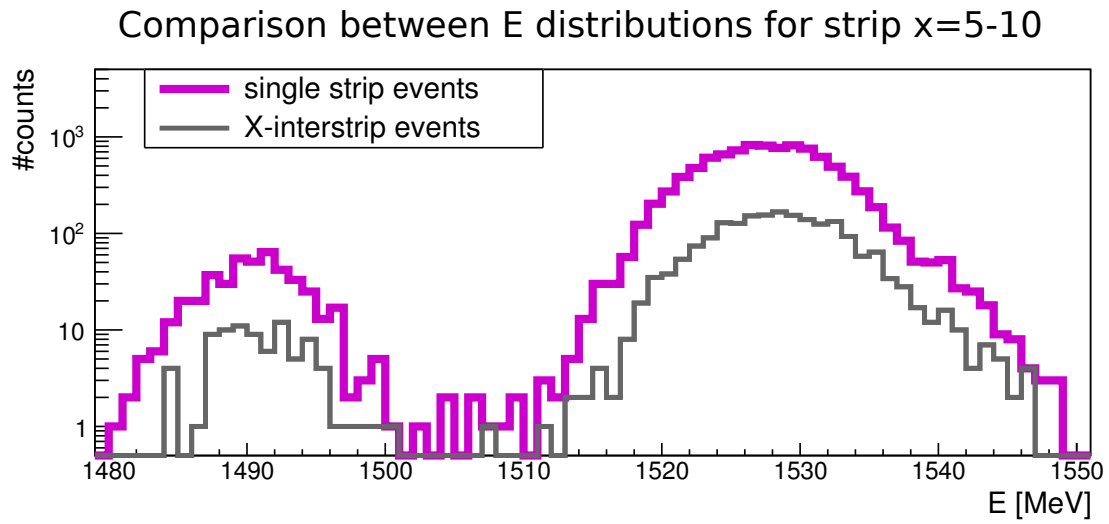

Figure 4.6: Comparison between the energy distributions of single-strip and the inter-strip events is shown for strip 5-10. The broadening of the inter-strip peak only slightly exceeds the width of the single-strip peak. For both cases, the energy separation between the backscattered Rutherford events and the (p, γ) peak can be clearly achieved.

theorem [159, 160] or in general by Gunn's theorem [161].

To extend the energy reconstructed dataset, the calibrated energy of the front side strip (E_y) was used for the x inter-strip events. As a result, a similar distribution can be obtained as for the single-strip events (upper left panel of Figure 4.4). The comparison between the energy distributions of the single-strip and inter-strip events is shown for strips x=5-10 in Figure 4.6. Despite the usage of the energy information from only one side of the DSSSD for the x inter-strip events, the width of the energy distribution exceeds only slightly over the energy distribution of the single-strip events. This indicates that the uncertainty is not dominated by the detector's intrinsic energy resolution but by other effects such as the probable overestimation of the beam quality or by the not accounted for longitudinal size of the target and beam, or other effects. The separation between (p, γ) peak and the back-scattered Rutherford events can be clearly achieved for the x inter-strip events.
The proportion of event types categorized by energy reconstruction is summarized in Figure 4.7. The ratio of the single-strip events, for which the energy reconstruction can be done only by realizing an intrinsic gain matching calibration, is conservatively estimated to be 70 % of all measured events. By reconstructing the energy of the x

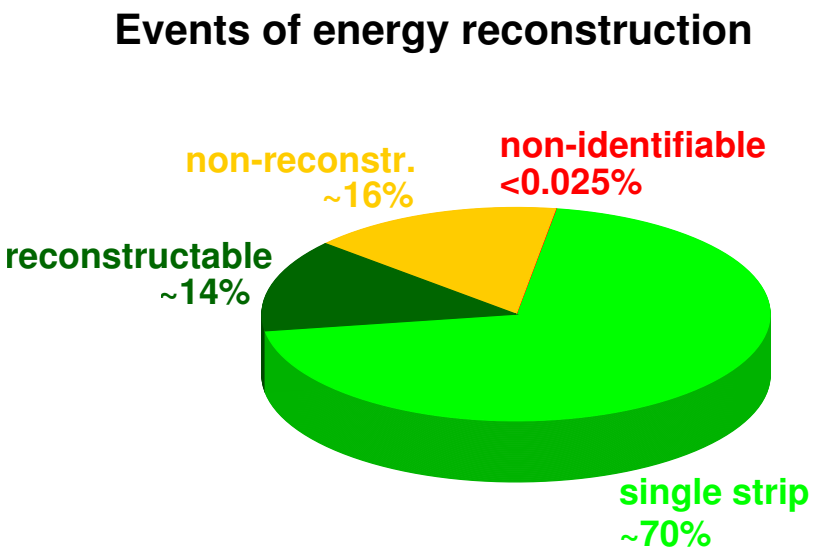

Figure 4.7: The proportion of events types categorized by the energy reconstruction. The ratio of the reconstructable events exceeds 80 %. The events, which could not be clearly distinguished between noise and an ion hit, are below 0.025 %.

inter-strip events, the ratio of events applicable for the energy separation method can be increased to 84 %. The remaining data include mainly the y inter-strip events, double inter-strip events (x and y inter-strip in coincidence) and also events for which the event categorization failed.

It is crucially important to determine the identification efficiency, which defines the amount of ion hits correctly recognized by the DSSSD. For $^{124}Xe^{54+}$ at beam energies of multiple MeV/u, the signal of an ion hit (in case of a single-strip event) is at least one order of magnitude higher than the noise level. Therefore, the ion can be undoubtedly distinguished from the noise. In the case of inter-strip events, the ion hit is associated to a pixel region with the largest deposition. Practically, this condition gives a natural limit at the half of the total ion energy for the x inter-strip events, and a slightly lower limit for the y inter-strip due to the energy defect, see Figure 4.5. For this reason, during the analysis a lower energy limit was set at one third of the energy of the single strip events, $E_{s.s.}/3$, above which the highest signal from each event was assigned to a valid ion hit. Reversely formulated, if the largest signals of an event is below the $E_{s.s.}/3$ energy threshold, it is considered as non-identified. The ratio of such events is below 0.025 %. Therefore, the ion-identification of the DSSSD surpasses >99.975 %.

In conclusion, the energy separation in combination with the Rutherford-background blocking is a powerful way to achieve complete background removal for the (p, γ) reaction measurements. The main drawback of the method originates from the limitations of a segmented silicon detector, namely that not the entire measured dataset, but approximately 80 % of all hits can be evaluated. This shrinks the applicability of the energy separation to cases, when the removal of the back-scattered Rutherford events is decisive. The cross section of the given (p, γ) reaction is extremely low in comparison to the Rutherford background as it is in the case of center-of-mass energies in the vicinity of the Gamow-window.

Chapter 5

The E127 experiment

In this chapter, first the proton-capture experiment performed in 2020 in the Experimental Storage Ring at GSI, the so called E127 experiment, will be described in detail. Uniquely, this is the first measurement of the proton-capture in a storage ring carried out using not only fully stripped, stable ^{124}Xe beam but radioactive ^{118}Te ion beam as well. Then, all major steps of the data analysis are discussed, starting with a brief introduction of the E127 DAQ, followed by a description of the calibration method and precise luminosity determination. Finally, the DSSSD spectra are investigated in order to determine the cross section for the (p, γ) and (p, n) nuclear reaction channels.

5.1 Experimental steps

For the E127 experiment, the time period between 17. - 22.03.2021 was granted by the GSI Program Advisory Committee (GPAC) at the Experimental Storage Ring [162]. For the calibration few additional days were provided before and after the experiment, see Figure 5.1. The E127 beam time had two major objectives.

- The realization of the first proton-capture measurement using a highly charged, radioactive-ion beam at the ESR. For this purpose the fragment separator (FRS) was used. The ^{118}Te(p,γ)^{119}I reaction was chosen, since ^{118}Te is in the region of the γ-process, has a reasonable half life of six days [30] and has no known metastable excited states.
- The proof of principle measurement of the novel background scraping technique, introduced in Chapter 3.3, which has the potential to improve the measurement sensitivity for the (p, γ) events tremendously.

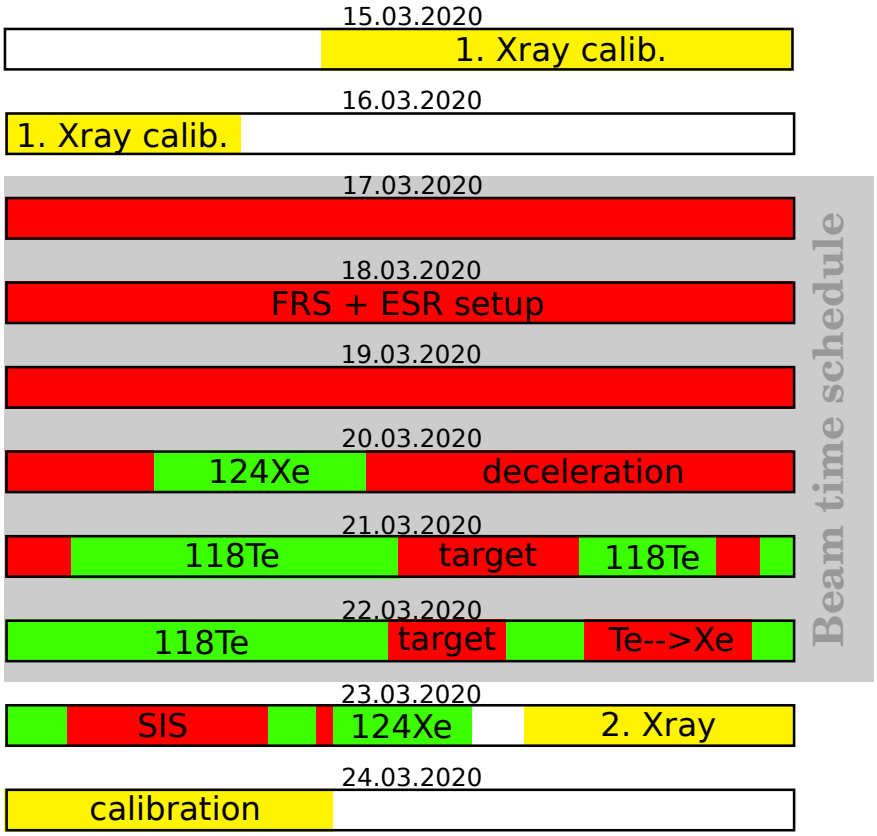

Figure 5.1: The time schedule of the E127 experiment. Green color denotes the measurement times, the red colored ranges mark the breakdown and optimization phases. The calibration times are tagged with yellow color.

The primary beam consisted of stable, fully stripped $^{124}Xe^{54+}$ ions allowing the test of the scraping device at high intensity ion beam. The fragment beam was created in the FRS by shooting the ^{124}Xe ions onto a Be production target with thickness of 2 mg/cm^2 and filtering out the $^{118}Te^{52+}$ ions by applying the $B\rho$-ΔE-$B\rho$ method, see Chapter 2.1.4. As a degrader 1 mm plastic scintillator was used. The rest gas pressure in the ESR was kept low, for the whole experiment it remained below $< 5 \cdot 10^{-11}$ mbar.

The exact time schedule of the experiment is shown on Figure 5.1. Green colored ranges mark the times spent with measurement in the ring, the calibration measurements are colored yellow. All the red colored fields denote optimization or troubleshooting phases such as optimization of the transmission from FRS to ESR, realization of beam deceleration, target density improvements, etc.
The major limitations of the accelerator setup were the modest transmission from the FRS to the ESR. Furthermore, the beam deceleration was restricted to 10.06 MeV/u due to the malfunction of the control system for the RF cavities at ESR. The lat-

ter effect caused the occurrence of the (p, n) nuclear channel underlying the spot of the (p,γ) cluster on the DSSSD. This fact made the selection of the ^{118}Te(p,γ) events significantly more difficult compared to a measurement below the (p, n) channel threshold at 7.4 MeV/u. Consequently for all measurements 10.06 MeV/u was set as the lowest available beam energy. In all experimental setups the H_2 gas jet target was in use at densities of about $5{\cdot}10^{13}$ atoms/cm^2.
The following beams were employed during the E127 experiment in chronological order:

- **Setting A:** ^{124}Xe beam through the FRS using the ERASE technique: quick test of the ERASE (see Chapter 3.3) and calibration of the ion-optical settings of FRS and ESR.
- **Setting B:** ^{118}Te beam using the ERASE technique: proton-capture measurement with the fragment beam.
- **Setting C:** ^{124}Xe beam excluding FRS using the ERASE technique: proton-capture measurement with high-intensity, stable beam. Beam was transfered from SIS18 via a direct beam line.
- **Setting D:** ^{124}Xe beam excluding FRS, without ERASE: high-intensity, control measurement of the ERASE technique.

In the following, the ^{118}Te and the high intensity ^{124}Xe data using ERASE will be analyzed in detail to calculate cross sections. For the evaluation of the novel ERASE technique, the high intensity ^{124}Xe data with and without the usage of the scraper, see Chapter 3.3 will be qualitatively inspected.

5.2 Data acquisition system

In the E127 experiment, the major devices, which provided the measurement data during beam time, were the HPGe detectors in combination with the DSSSD. All detectors and the data acquisition modules were handled in a common system. The schematic figure of the E127 DAQ is shown in Figure 5.2. The major components of the measurement system are the following:

- DSSSD and HPGe detectors: these units provided the primary measurement input data during the experiment including energy and timing signals. The sensor of the DSSSD was identical to the one, used in the E108b experiment

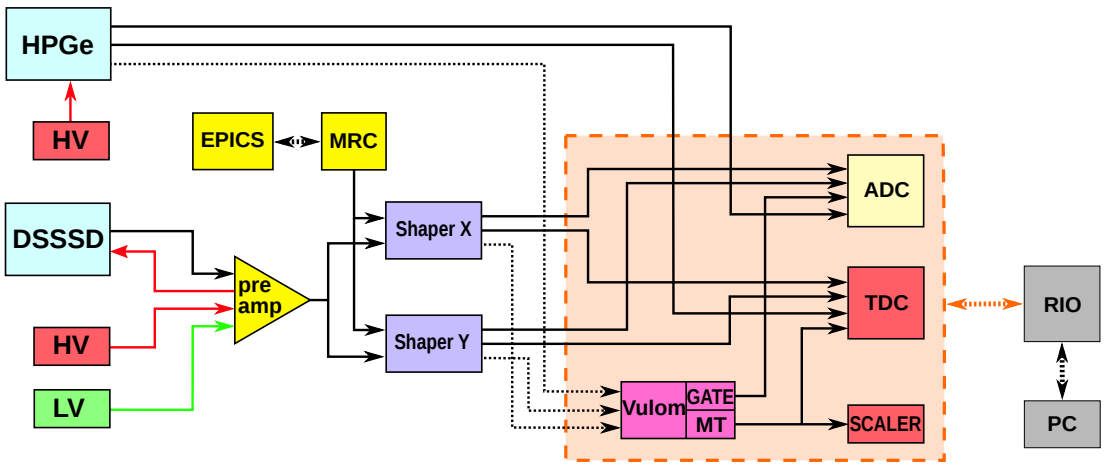

Figure 5.2: The schematic view of the DAQ for the E127 experiment is shown highlighting its major components.

in 2016, Micron Semiconductor Ltd W1-type DSSSD [130]. The DSSSD was responsible for the energy and time measurement of the heavy recoil ions after reaction. The HPGe detectors were used to measure the energy and timing signals of the X-ray photons produced due to the e^--capture at the target. The recorded X-ray spectra were used for cross section normalization as described in Chapter 5.3.

- preamplifier: The small currents of the DSSSD strips were first pre-amplified by a Multichannel PReamplifier manufactured by Mesytec (MPR-32) [163]. The isolation against external noise was ensured by short, well-shielded cables between the feed-through of the vacuum chamber and the preamplifier module.

- shaping amplifier: two MSCF-16 by Mesytec were employed [164]. The shaper module amplified again the signal and converted the pulses into a Gaussian shape. The MSCF modules include a Constant Fraction Discriminator (CFD), therefore, threshold and timing signals were independent of the pulse height [165, 166]. This eliminated amplitude-dependent time walk for signals, which was essential for the timing branch of the DAQ.

- MADC: Multi Analog to Digital Converter. Two MADC-32 units manufactured by Mesytec were used for the experiment to digitize the signal amplitude of the detectors. Each MADC had 2×16 channels, therefore, the DSSSD x and y channels together occupied a complete module.

- TDC: Time to Digital Converter, it digitizes the time information of the detector signal. Two TDC modules manufactured by CAEN (32CH, TDC Mod. V775 [167]) were in use analogously to the ADCs.
- Vulom: It was a universal trigger logic module equipped wiht a programmable FPGA [168]. The firmware TRLO II was used to provide extended trigger logic functionalities [169]. It was used to handle trigger priorities, dead time and logical signal distribution to ensure reliable readout.
- EPICS and MRC: the EPICS server was responsible for the remote control of MSCF and HV. The communication with all remote controllable Mesytec modules was ensured by the MRC unit (MRC-1 Mesytec [170]).
- RIO: it was the heart of the data acquisition. It handled the readout of all VME modules by running the Drasi DAQ [171]. It also ran transport and stream servers to store and to monitor the experimental data, respectively.

During the experiment the count rates and the spectra from different detectors were monitored online in case any quick intervention is required. Simultaneously, the experimental data was stored on multiple hard drives in form of compressed *lmd* files, which are the basis for the final analysis.

5.3 Calibration of the HPGe detectors

During the experiment three High-Purity Germanium (HPGe) detectors by ORTEC [172] were placed around the H_2 gas-jet target at 35°, 90° and 145° with respect to the beam axis in order to measure the X-ray radiation emitted through the atomic interaction of the stored ions with the internal target.All HPGe detectors were calibrated twice, before and after the experiment by employing calibrated X-ray and γ emitters: ^{241}Am, ^{133}Ba, and ^{210}Pb covering the relevant energy range for the experiment between 26 keV and 81 keV.

5.3.1 Energy scale calibration

The energy calibration of the X-ray detectors was based on the identification of the gamma and X-ray radiation lines in the spectra of the certified sources. The energies of the characteristic lines are available in nuclear databases, such as the NUDAT2.0 [173]. After the energy calibration of the X-ray detectors, the signature of the atomic interaction between beam and target can be identified in the experimental dataset.

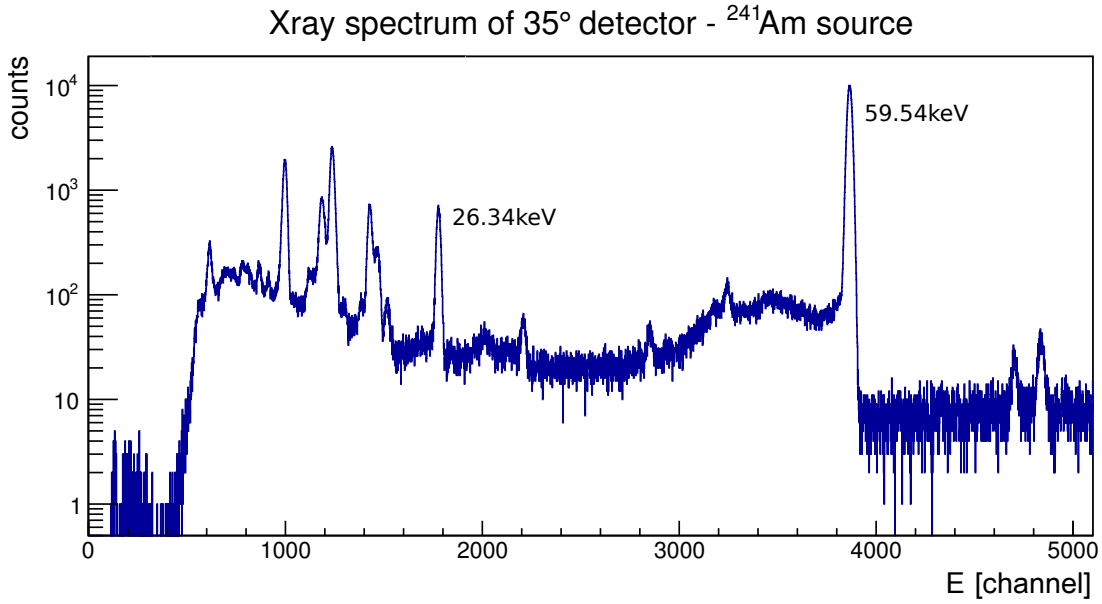

Figure 5.3: The X-ray spectrum obtained with the Germanium detector at 35° using the ^{241}Am source. For calibration, characteristic lines at 26.34 keV and 59.54 keV were used.

Unfortunately, an initially wrong ADC gate setting for the HPGe detectors made the energy calibration before the experiment useless. However, the energy calibration after the experiment was successful.

In Figure 5.3 the measured spectrum from the Xray detector at 35° of the ^{241}Am source is shown. For calibration the characteristic lines at 26.34 keV and 59.54 keV were used. The mean value of the peaks, thereby, the position of the lines is determined by a combined fit of a Gaussian function describing the peak with a linear function representing the background. The procedure was also done for the high-intensity ^{133}Ba source, extended with a low-intensity ^{133}Ba source measurements, using characteristic lines at 30.973 keV, 34.987 keV, 35.818 keV, 53.1622 keV, 79.6142 keV and 80.9979 keV for each detector. In addition, the 46.539 keV line from the ^{210}Pb source was analyzed for the 90° detector. The parameters of the fitted linear calibration function can be found in Table 5.1.

5.3.2 Efficiency calibration

The used planar High-purity Ge-detectors are ideal to measure photons with energies in the X-ray regime. The typical intrinsic detector efficiency can reach nearly 100 %.

	slope [keV/channel]	intersection [keV]
HPGe detector at 35°	0.015898 ± 3e-06	-1.91 ± 0.01
HPGe detector at 90°	0.02106 ± 2e-05	-2.26 ± 0.05
HPGe detector at 145°	0.01663 ± 2e-05	-1.76 ± 0.06

Table 5.1: The energy calibration results are shown, obtained from the linear fit of the Xray data performed after the E127 beam time.

In order to characterize precisely the efficiency curve of the Ge detectors used during the E127 experiment as a function of the photon energy, calibrated source measurements have been employed. To obtain an absolute efficiency valid for the geometry between target and detectors, this geometry was precisely reproduced with the sources for each detector during the experiment. This way the intrinsic efficiency ($\epsilon_{intrinsic}$), which describes exclusively the efficiency of the detector, becomes weighted with the solid angle of the detector window ($\Delta\Omega/4\pi$). The so called absolute efficiency could be directly obtained such as

$$\epsilon_{abs.}(E) = \frac{\Delta\Omega}{4\pi}\epsilon_{intrinsic}(E). \tag{5.1}$$

The absolute efficiency of a detector for a certain energy can be determined experimentally by dividing the number of detected events by the total number of expected decays and the line intensity. For a certain line at energy E with a known intensity, the absolute efficiency can be expressed as

$$\epsilon_{abs.}(E) = \frac{C_{det}(E)}{R_0 \cdot \exp\{-\lambda t_w\}\ \ I_\gamma(E)\ t_M\ \Theta\ \frac{1-\exp\{-\lambda t_M\}}{\lambda t_M}} \approx \frac{C_{det}(E)}{R\ I_\gamma(E)\ t_M\ \Theta} \tag{5.2}$$

where, $C_{det}(E)$ denotes the number of detected events at a characteristic photon energy, $R = \ R_0 \cdot \exp\{-\lambda t_w\}$ is the activity of the calibration source at the start of the measurement, $I_\gamma(E)$ denotes the radiation intensity known from literature e.g. from the NUDAT2.0 database [173]. The term $t_M\Theta$ is the effective measurement time, meaning that the total measurement time t_M is corrected for dead time $dt = 1-$(accepted triggers)/(incoming triggers) such as $\Theta = 1-dt$. The term λ denotes the decay constant of the radioactive source. Since the measurement times are orders of magnitude shorter than the decay constant $t_M \ll \lambda$, the last term in the denominator can be neglected.

The number of the detected photons was determined by integrating the peak area without background of the characteristic lines in the X-ray spectra, see Figure 5.3. Technically, the peaks with reasonable intensity were first fitted with a combined

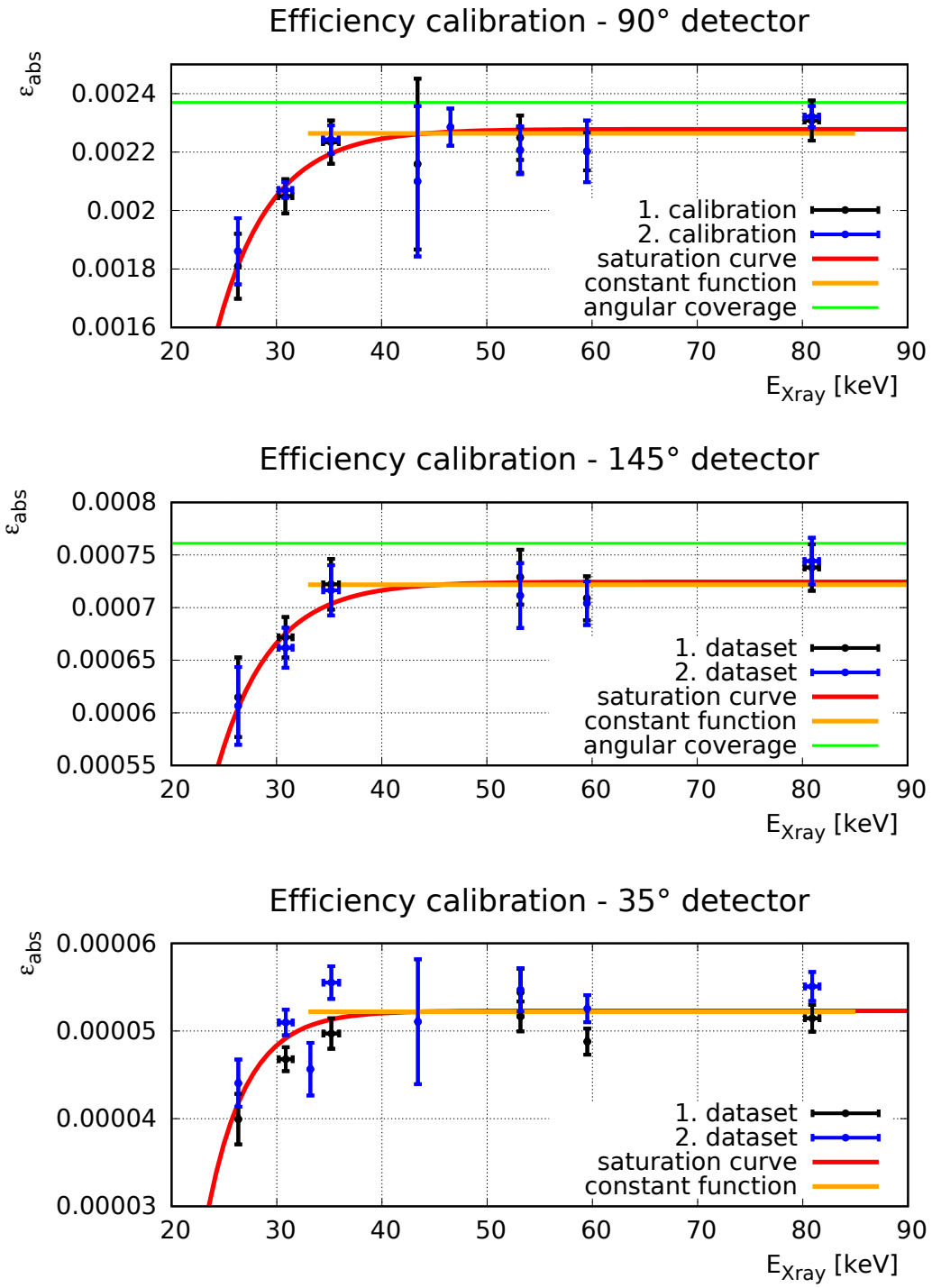

Figure 5.4: The measured efficiencies for employed X-ray detectors are shown. The data is fitted with a phenomenological function describing the effect of the thin Be window at the entry of the detector. In addition, a constant function is fitted above ∼35 keV to obtain the plateau of the detector efficiency curve.

Gaussian and linear function, than the background component (the linear fit) was subtracted.

The measured efficiency values for all three HPGe detectors are shown in Figure 5.4. The commonly used empirical function to describe the global dependency of the efficiency for HPGe detectors over the energy is the combination of a rising and a decaying exponential curves,

$$\epsilon_{HPGe}(E) \sim (1 - e^{-\frac{(E-p_2)}{p_1}}) \cdot e^{-\frac{E}{p_3}} \approx 1 - e^{-\frac{(E-p_2)}{p_1}}, \text{ when } E < 100\,\text{keV}. \tag{5.3}$$

The rising exponential function describes the transmission through the berillium window at the entry and the decaying exponent takes into account the finite detector thickness [174]. Since all source energies are below 100 keV, the full energy of the photons is deposited within the detector volume. Therefore, the second term in Eq. 5.3 can be neglected. The measured efficiencies were fitted with a rising exponential function and in addition the efficiency values above >35 keV were fitted with a constant function to obtain the plateau of the detector efficiency curve. The two fits are in agreement within the measurement uncertainties of 41.4 keV - 52.6 keV, where the K-REC lines of ^{124}Xe and ^{118}Te are expected. The uncertainties of the measured efficiencies were under control: the activity of the sources accounts for 2% uncertainty; the peak fitting contributes 3.5 %; and the geometry of the target and HPGe detectors is known within 1 % accuracy. The efficiencies were measured two times for all three HPGe detectors. The results could be reproduced for the detectors at 90° and 145° within <1.5 % agreement and within 7 % for the detector at 35°for the K-REC energy range (between 35-55 keV). Summing up all the uncertainties conservatively, for the 90° and 145° detectors an overall uncertainty was taken as 5 %, while for the detector at 35° 10 % uncertainty was assigned.

5.4 Luminosity measurement

The luminosity determination was carried out by using the three Xray detectors around the gas jet target. The method is based on the K-REC normalization technique and is described in detail in Chapter 2.2.4. The number of events recorded by the X-ray detector at 90° was by about one and two orders of magnitude larger than as for the detectors at 145° and 35°, respectively. For this reason, the data recorded by the 90° detector will be used exclusively to calculate the luminosity. The measurements at 145° and 35° still serve as control measurements.
The integrated luminosity for a measurement can be expressed as

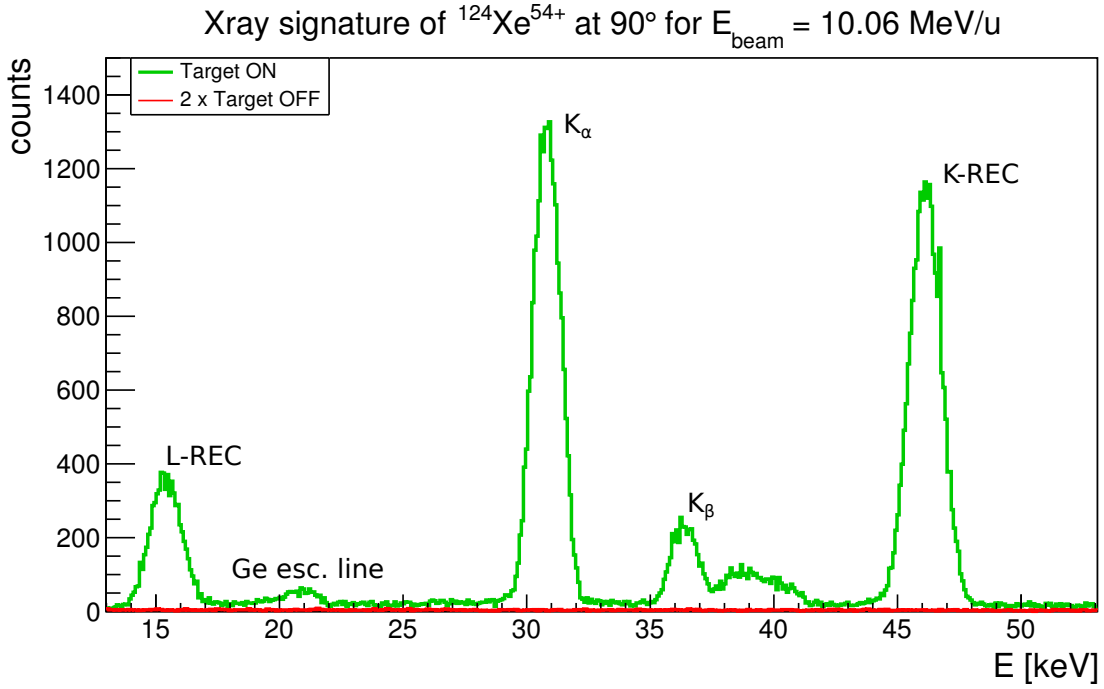

Figure 5.5: The X-ray signature of the beam and target interaction recorded by the HPGe detector at 90° when using high intensity ^{124}Xe beam on H_2 target.

$$L_{int.} = \frac{N_{KREC}}{4\pi\ \epsilon_{abs.}(E_{KREC})\ \frac{d\sigma_{KREC}}{d\Omega}\big|_{det.}}. \tag{5.4}$$

where N_{KREC} is the number of events in the K-REC peak, $\epsilon_{abs.}(E_{KREC})$ is the detector efficiency at the K-REC energy, $\frac{d\sigma_{KREC}}{d\Omega}\big|_{det.}$ denotes the theoretically calculated differential K-REC cross section taken for the covered angles of the detector. Accordingly, an averaged luminosity per unit time can be calculated as

$$L_{avg.} = \frac{N_{KREC}}{4\pi\ \epsilon_{abs.}(E_{KREC})\ \frac{d\sigma_{KREC}}{d\Omega}\big|_{det.}\ t_M\ \Theta}\ , \tag{5.5}$$

which basically equals the integrated luminosity divided by the the effective measurement time ($t_M\Theta$).

The X-ray signature of the beam and target interaction recorded at 90° is shown for Setting C in Figure 5.5. In the spectrum multiple atomic lines can be observed such as for the K_α, K_β, K_{REC} and L_{REC} transitions in ^{124}Xe. In addition, the K_α escape line is also present. When the energy of the impinging photon is higher than the K-edge energy of the atoms of the detector, the photons are able to excite its K-shell electron. After de-excitation the emitted K_α photon of germanium can leave the detector and

the energy of the impinging photon is only partly absorbed. The missing energy is consistently large, therefore, a characteristic line occurs in the spectrum below the energy of the original impinging photon. This line is called the germanium K_α escape line, which appears at

$$E_{esc,K\alpha} = E_{ph.} - 9.876\,\text{keV}\ [175], \tag{5.6}$$

where $E_{ph.}$ is the energy of the incident photon.
It is important to highlight, that no structured background contribution can be observed in the range of the K-REC peak. Therefore, the number of events within the K-REC peak can be determined by using the standard peak fitting method realized by a Gaussian function combined with a linear background. The measured position of the K-REC peak is 46.093(5) keV and 43.14(5) keV at 90° for the ^{124}Xe and the ^{118}Te ions, respectively. Although, both values slightly deviate from the literature values, which are 46.37 keV for ^{124}Xe and 43.27 keV ^{118}Te beams at 10.06 MeV/u [133, 176], this discrepancy affects the efficiency determination to a negligible extent. The obtained numbers of events in the K-REC peaks can be found in Table 5.2.
Theoretical calculations of the K-REC process were performed by Prof. Dr. Andrey Surzhykov [177]. The differential K-REC cross section for $^{124}Xe^{54+}$ and $^{118}Te^{52+}$ beams at 10.06 MeV/u were determined as a function of the photon emission angle in the laboratory frame ϑ_{lab} with respect to the beam direction. The photon-emission is symmetrical in the azimuthal φ angle but asymmetric in ϑ_{lab}. The reaction was approximated as a collision of a beam ion with two hydrogen atoms instead of a H_2 molecule. Therefore, the accuracy of the model is conservatively within 1 % [177]. The differential cross section was integrated for the finite solid angle coverage of the Xray detectors. The obtained effective differential cross section values are shown in Table 5.2.

According to Eq. 5.5, the luminosity for the ^{124}Xe and for the ^{118}Te measurements was determined, see Table 5.2. Three separate luminosity measurements of the ^{124}Xe datasets taken by the X-ray detectors at 90°, 145° and 35° are in good agreement. For the ^{118}Te dataset only the peak at 90° was distinguishable from the background in the corresponding spectra. The difference of the luminosities between the ^{124}Xe and ^{118}Te measurements is about two orders of magnitude and might have several causes. The major reason is the low intensity of secondary ^{118}Te beam as compared to primary ^{124}Xe beam. In average the intensity of the decelerated ^{124}Xe beam was

	^{124}Xe with scraper			^{118}Te
det. angle	**90°**	**145°**	**35°**	**90°**
$\mathbf{N_{KREC}}$	21694 ± 151	2145 ± 52	175 ± 15	1196 ± 69
$\epsilon_{\mathbf{abs.}}(\mathbf{E_{KREC}})$	(2.3±0.1)e-3	(7.2±0.4)e-4	(5.2±0.5)e-5	(2.3±0.1)e-3
$\frac{d\sigma_{KREC}}{d\Omega}\Big\vert_{\mathbf{det.}}$ [b/sr]	128.4±1.3	42.0±0.4	45.6±0.5	118.6±1.2
$\mathbf{t_{meas.}}\ \Theta$ [s]	4411	4411	4411	30396
$\mathbf{L_{avg.}}$ [$\mathbf{barn^{-1}s^{-1}}$]	1.343±0.069	1.284±0.073	1.33±0.17	(1.17±0.09)e-2
$\mathbf{L_{int.}}$ [$\mathbf{barn^{-1}}$]	5926±305	5663±320	5846±762	355±27

Table 5.2: The summary table of all the values required for luminosity calculation. The luminosities measured by the three Xray detectors for the ^{124}Xe beam are in agreement. The difference between the luminosity of the Xe and Te data are significant.

around $6 \cdot 10^6$ ions and the intensity of ^{118}Te beam was below 10^5 ions at the start of a measurement phase.

5.5 Analysis of the DSSSD spectra

5.5.1 The ^{124}Xe(p,γ) reaction

For all experiments performed with the ^{124}Xe or with the ^{118}Te beam the DSSSD was positioned in such a way to safely measure all (p,γ) events. The corresponding peak is captured approximately in the middle of the detector. The precise location of the (p,γ) cluster's center is determined by fitting the peak in the 2D spectrum from the detector. Due to the low amount of hits in the ^{118}Te dataset, the fit could be realized only for the high intensity ^{124}Xe beam in Setting C. However, since the detector movements are well documented during the E127 beamtime, the fit of the ^{124}Xe dataset, extended by MOCADI simulations, defines the location of the ^{118}Te(p,γ) peak's center as well. The position of the (p,n) distribution could not be determined by fitting since the it is much more spread out in comparison to the (p,γ) peak. In addition, only a part of the (p,n) distribution, around ∼35 %, was covered by the detector. The center of the (p,n) peak was defined relative to the (p,γ) peak based on MOCADI simulations. The MOCADI simulations were already tested in the analysis of the E_{CM}=7.92 MeV dataset from the E108b experiment and they were proven to be precise in regard to the relative positions of the (p,γ) and (p,n) peaks, see Chapter 3.2.

The regions on the detector plane, which contain all (p,γ) and all (p,n) events, were determined by MOCADI simulations assuming the compound nucleus decays directly

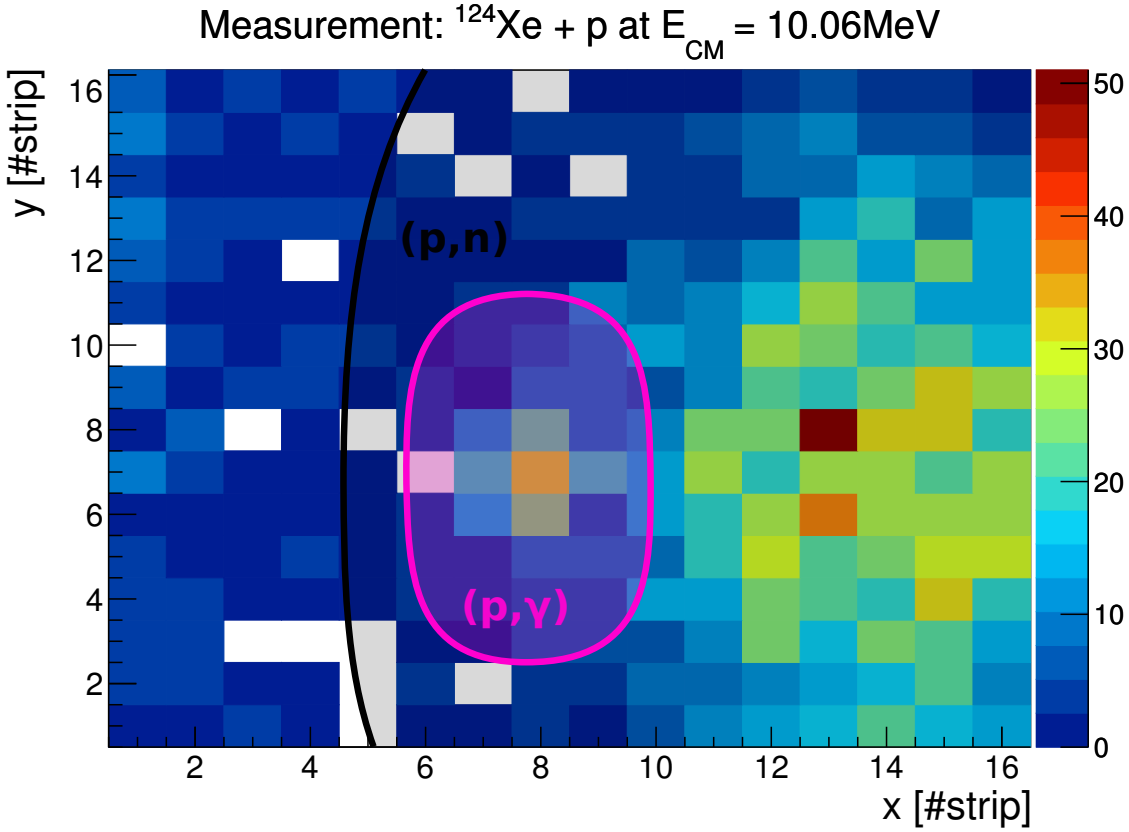

Figure 5.6: The measured DSSSD spectrum is shown for the high intensity ^{124}Xe beam. The kinematically possible ranges for the (p,γ) and (p,n) events are indicated on the Figure. The (p,n) distribution spreads over the (p,γ) spot.

to the ground state. Thereby, the largest, kinematically possible cone is obtained, within which all narrower cones from cascading decays are included. These cones, projected onto the DSSSD surface, are shown for the ^{124}Xe dataset using Setting C on Figure 5.6.

The (p,n) region spreads over the (p,γ) distribution for the ^{124}Xe beam, complicating the determination of the (p,γ) events. In addition, to simulate the shape of the (p,γ) or the (p,n) distributions the cascade information of the compound nucleus is required, which is not precisely known for neither case. Therefore, in the fit model both peaks are approximated by Gaussian-shape distributions. In addition, the fit also contains a constant parameter, which represents the background due to the back-scattered Rutherford events. The complex model was fitted locally, in the vicinity of the (p,γ) peak. While using the approximations to describe the shape of the (p,γ) and (p,n) distributions, a χ^2/NDF=0.83 and NDF=83 was achieved for the fit. The number of (p,γ) events was obtained by subtracting the background

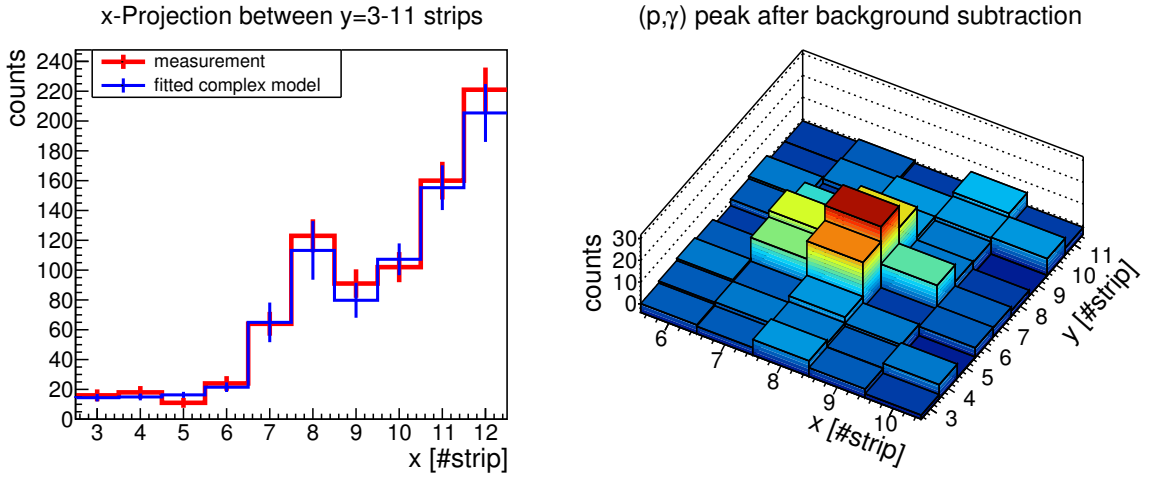

Figure 5.7: Left panel: A comparison between the measurement and the fitted function is shown for the ^{124}Xe(p,γ) peak. Right panel: the (p,γ) peak after background subtraction.

component of the fit from the measurement data. A comparison between the measurement and the fit is shown in left panel of Figure 5.7, while in the right panel the background subtracted (p,γ) peak is visible. After background subtraction from the (p,γ) peak, the events within its maximal spot size were integrated, and the number of (p,γ) counts was found to be $N_{^{124}\mathrm{Xe(p,\gamma)}} = 139 \pm 20_{stat} \pm 28_{syst}$. The statistical uncertainty accounts for the measurement uncertainty before background subtraction. The systematic uncertainties represent the uncertainty of the fitted model. In order to obtain the cross section of the (p,γ) reaction for E_{CM}=10.06(1) MeV, the number of (p,γ) counts was divided by the integrated luminosity of the related measurement (Table 5.2),

$$\sigma_{^{124}\mathrm{Xe(p,\gamma)}}(E_{CM} = 10.06(1)\,\mathrm{MeV}) = \frac{N_{^{124}\mathrm{Xe}(p,\gamma)}}{L_{int.}^{^{124}\mathrm{Xe},\,90^\circ}} = 23.4 \pm 3.3_{stat} \pm 4.9_{syst}\,\mathrm{mb}. \quad (5.7)$$

The systematic uncertainty of the cross section includes the uncertainty of the luminosity measurement of the order of ∼5 %. The result is discussed in the context of the previous (p,γ) measurement at the ESR [9] in Chapter 6.2. All cross sections determined in this work are given in Table 6.1.

5.5.2 Test of the ERASE technique

The E127 beam time provided the first opportunity to test the novel Elimination of the Rutherford elAstic ScattEring (ERASE) technique to improve the measurement sensitivity for the proton capture products. The technical details were carried out

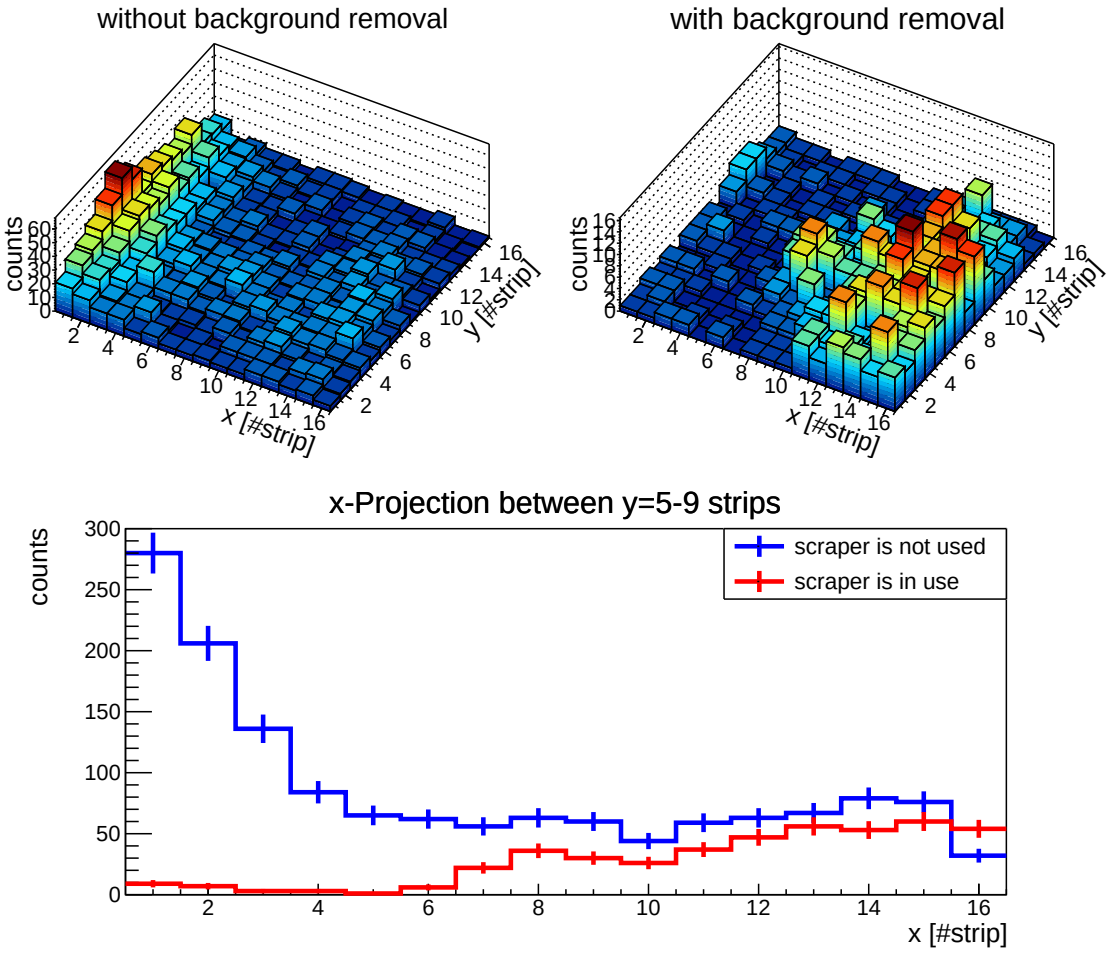

Figure 5.8: The comparison is shown between measurements without (upper left panel) and with (upper right panel) applying the novel scraping method. The difference for the middle y-strips, which include most of the (p,γ) distribution and a cross section of the (p,n) distribution is shown on the lower panel. When the scraper was not in use, the number of events in the (p,γ) peak is comparable to the level of the Rutherford background, the (p,γ) cluster is barely visible. When applying the scraper device, the background is massively reduced at the spot of the (p,γ) and the (p,n) events, the peaks clearly emerge from the background. The effect of the scraper is discussed in the text.

according to simulations introduced in Chapter 3.3, the only parameter which became constrained in experiment is the distance between the beam axis and the scraping edge. For both, the stable and fragment beams the gap was set to (35.0 ± 0.5) mm. The distance was measured by changing the scraper position in millimeter steps until the stored beam was destroyed. At the end of the beam time a control measurement was carried out with the high intensity ^{124}Xe beam without using the scraper device.

The comparison between the control measurement (Setting D) and an identical measurement, when the scraping was applied (Setting C), is shown in Figure 5.8. Both datasets are normalized to integrated luminosity (L_{int}). Since the number of (p,γ) counts is proportional to the integrated luminosity,

$$N_{(p,\gamma)} \sim L_{int} \ , \tag{5.8}$$

and the reaction products are measured by the identical setups with the same DSSSD, the two normalized samples contain the same number of (p,γ) counts ($N_{(p,\gamma)}$). The normalization of the integrated luminosity can be practically realized by normalizing to the number of events in the K-REC peak, since

$$L_{int} \sim N_{K-REC} \tag{5.9}$$

and the setup of the luminosity measurement is as well identical for both datasets.

The emergence of the proton capture products from the Rutherford background in the datasets is apparent. When the ERASE was not in use, the (p,γ) and (p,n) peaks, centered at x=8 strip and x=14 strip, respectively, are situated on the top of the much more intense Rutherford-scattering background, the peaks are easily seen. However, when the scraper is employed, the background is dramatically reduced. For the strips x=1-2, which are the nearest to the beam, some remnants of the forward-scattered and the back-scattered Rutherford components are still present. The $x > 2$ strips, which are further from the beam, the low-intensity backward scattered Rutherford distribution dominates. The direct forward-scattered part of the Rutherford distribution is completely removed by the scraper device for these strips. Therefore, only a low-intensity Rutherford background can be observed within the area of the (p,γ) and (p,n) peaks. This is clearly visible in the measured datasets, see lower panel of Figure 5.8. To quantify the improvement in the sensitivity for the (p,γ) products, the signal-to-background ratio (SBR) is defined as

$$SBR_{(p,\gamma)\ spot} = \left.\frac{N_{(p,\gamma)}}{N_{bckgnd}}\right|_{(p,\gamma)\ spot} = \left.\frac{N_{(p,\gamma)}}{N_{all} - N_{(p,\gamma)} - N_{(p,n)}}\right|_{(p,\gamma)\ spot} , \tag{5.10}$$

where, N_{bckgnd} denotes the number Rutherford background events within the area of the (p,γ) peak. For Setting C, the number of background events can be obtained from the complex fit described in Chapter 5.5.1. The number of the background events can alternatively be obtained by subtracting the number of (p,γ) and (p,n) events

from all measured events in the area of the (p,γ) peak, N_{bckgnd}=N_{all}-$N_{(p,\gamma)}$-$N_{(p,n)}$. This second method was used for Setting D, when the complete Rutherford background is present in the (p,γ) peak. Since a precise cascade model of the ^{124}Xe(p,n) distribution is not known, the number of (p,n) events $N_{(p,n)}$ within the (p,γ) region was estimated from the fitted 2D Gaussian function described in Chapter 5.5.1. By applying Eq. 5.10, the improvement of the signal-to-background ratio between scraping and no-scraping datasets is deduced:

$$\frac{\mathrm{SBR}^{\text{scraping}}_{(p,\gamma)\ \text{spot}}}{\mathrm{SBR}^{\text{no-scraping}}_{(p,\gamma)\ \text{spot}}} = 10.8 \pm 2.4. \tag{5.11}$$

This result means, that employment of the ERASE technique improves the signal-to-background ratio by a factor of $\sim$11 in the area of the (p,γ) peak. This is certainly an efficiency boost of the measurement technique for the (p,γ) products at the ESR. The improvement can be expressed in the extent of the Rutherford background removal. Since in both datasets the number of (p,γ) counts is the same, the quality of the background removal can be described with

$$1 - \frac{\mathrm{N}^{\text{scraping}}_{\text{bckgnd}}}{\mathrm{N}^{\text{no-scraping}}_{\text{bckgnd}}} = 1 - \frac{\mathrm{SBR}^{\text{no-scraping}}_{(p,\gamma)\ \text{spot}}}{\mathrm{SBR}^{\text{scraping}}_{(p,\gamma)\ \text{spot}}} = (91 \pm 2)\% \tag{5.12}$$

The uncertainties of the values in Eq. 5.11 and Eq. 5.12 reflect the limited statistics of the measured datasets and can be improved in the future by increasing the integrated luminosity. Although, eliminating (91$\pm$2) % of the Rutherford background is slightly below the predicted 95% value, as simulated in Chapter 3.3.1, it is still an excellent result which clearly justifies the application of the ERASE technique for future measurements.

The cause of the 4 % discrepancy between the measurement and simulation in regard to the eliminated background is not straightforward. A better analysis requires a better energy calibration of the DSSSD data. Furthermore, such calibration could further remove or even completely eliminate the background contribution at the area of the (p,γ) peak. However, due the limited data collected during in the E127 beamtime, an energy calibration of the DSSSD could not be reliably performed. It remains unclear, for example, whether Rutherford events, which re-scattered on the scraping edge, reach the (p,γ) spot. However, even if so, the measured datasets strongly hint that the amount of unexpected secondary scattering processes is negligible and only the low-intensity back-scattered Rutherford component remains sizeable at the spot of the (p,γ) events.

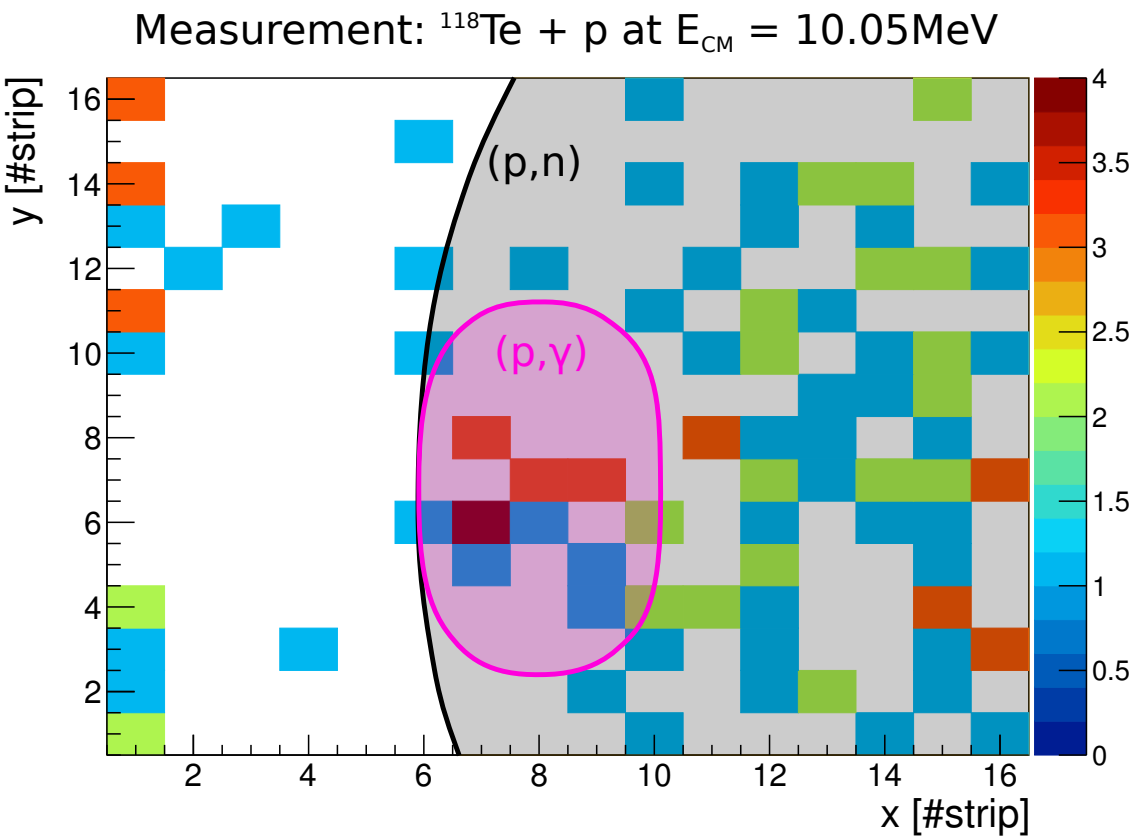

Figure 5.9: The DSSSD spectrum for the ^{118}Te measurement. The location of the (p,γ) and (p,n) peaks is analogous to the ^{124}Xe measurement, the (p,n) distribution completely covers the entire (p,γ) spot.

5.5.3 The ^{118}Te(p,γ) reaction

The spatial spectrum on the DSSSD for the radioactive ion beam measurement is completely analogous to the case of the stable ^{124}Xe beam, however, the obtained statistic is about 17 times lower than in the ^{124}Xe case, which makes the analysis much more difficult. The DSSSD spectrum for the ^{118}Te measurement is shown in Figure 5.9. The maximal spot size of the (p,γ) and (p,n) distributions was determined with MOCADI simulation. The location of the (p,γ) peak is analogous to the ^{124}Xe measurement and it is completely covered by the (p,n) cone. Here, the same methodology as in the case of ^{124}Xe(p,γ) events was not applicable. Due to the limited statistics, the peaks cannot be fitted reliably.

In order to determine the (p,n) contribution, the (p,γ) spot was subdivided into zones, see Figure 5.10. For each zone, a kinematical simulation of a possible (p,n) distribution has been carried out by the MOCADI code. The contours of the simulated (p,n) distributions define the outer edges of the zones. The size of the (p,n)

distribution on the DSSSD with good approximation depends only on the energy of the first populated state after the decay of the compound nucleus, as it is discussed in Chapter 3.2.6. The back-scattered Rutherford contribution at the spot of the (p,γ) peak is nearly negligible, and is already contained within the (p,n) distribution.
To restrict the number of (p,n) events (N_Z^A) within the (p,γ) spot for one zone (Z), the measured (p,n) events outside the (p,γ) spot for that particular zone (N_Z^B+N_Z^C) were used with some carefully chosen weights (w_z) as follows:

$$\text{total } (p,n) \text{ bckgnd.}\Big|_{(p,\gamma)\ \text{spot}} = \sum_{Z=1}^{3} N_Z^A = \sum_{Z=1}^{3} (N_Z^B + N_Z^C)\frac{w_Z^A}{w_Z^B + w_Z^C} \tag{5.13}$$

For the weights a minimum and a maximum estimation is given. In case of the minimum background estimation, the weight equals to the area of the given region, i.e. w_Z^i=$Area_Z^i$, where i=$\{A,B,C\}$. In case of the maximum background estimation the weight is defined by the kinematically possible maximum asymmetry of the (p,n) cone, i.e. w_Z^i=K_Z^i, where K_Z^i denotes the number of events in a kinematic simulation for zone Z and i=$\{A,B,C\}$. This asymmetry occurs for all distributions with spherical shape in the center-of-mass system after passing through the dipole magnet. The highest asymmetry within a zone is realized when the zone includes the edge of the simulated (p,n) distribution. The size of a zone reflects the width of the outer rim of the simulated (p,n) distribution.
In order to distribute the integer counts of the measured events among the zones and to account for the (p,γ) position uncertainty, a Monte Carlo simulation has been carried out. The simulation treats the coordinates of the center of the (p,γ) distribution as random variables within their uncertainties, Δx=0.085 strip and Δy=0.092 strip. Therefore, the simulation provides a reliable estimate of the uncertainty of the (p,γ) counts though the uncertain location of the peak.

The result of the Monte Carlo simulations is shown on Figure 5.11. The position of the distribution indicates the number of (p,γ) events of using the minimum background estimation (left panel) and maximum background estimation (right panel). The result for the number of (p,γ) events is taken as the average of these values and amounts to $N_{^{118}\text{Te(p,}\gamma\text{)}} = 13 \pm 4_{stat} \pm 2_{syst}$. The statistical uncertainty corresponds to the uncertainty of the measured events, as follows conveniently from Poisson statistics. In the systematic uncertainty the leading term is the position uncertainty of the (p,γ) and (p,n) distributions of the order of $\sim$13 %, which is defined by the width of the distribution in Figure 5.11. In additon, it contains also the difference between

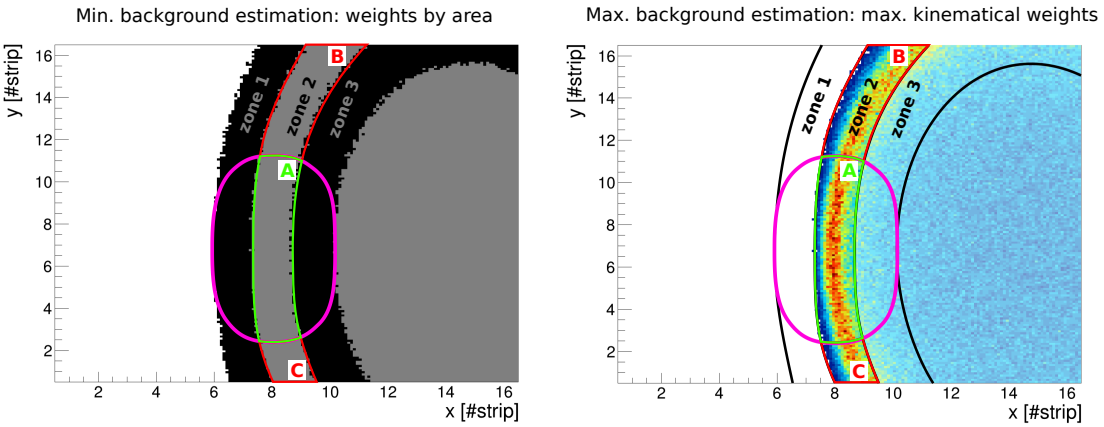

Figure 5.10: In order to estimate the background within the spot of the (p,γ) events, the (p,γ) region is subdivided into three regions defined by possible (p,n) distributions. The left panel shows the method for the minimum estimation of the background while in the right panel the method for the maximum background estimation is displayed. Detailed description of the method can be found in the text.

the minimum and maximum background estimations in the order of ∼2 %, which is defined by the difference of these two peaks. In order to obtain the cross section of the (p,γ) reaction for E_{CM}=10.05(1) MeV, the number of (p,γ) counts was divided by the integrated luminosity of the related measurement (see Table 5.2),

$$\sigma_{^{118}\mathrm{Te(p,\gamma)}}(E_{CM} = 10.05(1)\,\mathrm{MeV}) = \frac{N_{^{118}\mathrm{Te(p,\gamma)}}}{L_{int.}^{^{118}\mathrm{Te},\,90^\circ}} = 35.7 \pm 12.5_{stat} \pm 5.4_{syst}\,\mathrm{mb}. \quad (5.14)$$

Accordingly, the systematic uncertainty is increased by the uncertainty of the luminosity measurement, which is about ∼8 %. A discussion on the obtained result is given in Chapter 6.3. All cross sections determined in this work are given in Table 6.1.

5.5.4 The (p,n) reaction

The major challenge of the (p,n) channel measurement for ^{124}Xe and ^{118}Te beams at 10 MeV/u is the size of the corresponding distribution. To cover the complete area of the (p,n) distribution at the detector plane, the combined measurement of at least two DSSSDs would be required. Such a setup cannot be realized due to the size limitations within the dipole magnet. Still, the dominant part of the distribution can be measured and the remaining parts can be estimated. Although, during the E127 experiment the detector was positioned primarily to cover the (p,γ) peak, ∼35 % area of the complete (p,n) distribution was measured. Since the ^{124}Xe and ^{118}Te datasets

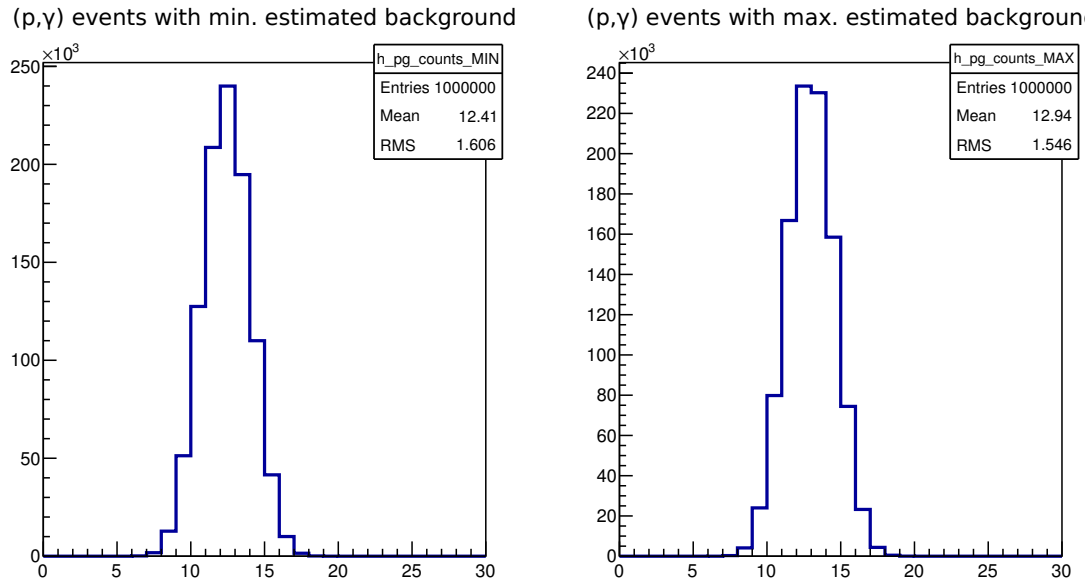

Figure 5.11: The number of ^{118}Te(p,γ) events was determined by Monte Carlo methods. For the background at the spot of the (p,γ) distribution a minimum and a maximum estimation was given. For more details, see text.

are analogous, the methodology will be demonstrated by the analysis of the ^{124}Xe measurement.

The measured and the missing parts of the ^{124}Xe(p,n) distribution are shown in Figure 5.12. The size of the distribution is determined by MOCADI simulation. The center of the distribution is determined by the combined information of the ^{124}Xe(p,γ) fit and the MOCADI simulations.
The (p,n) distribution can be divided into five regions, see Figure 5.12. For the measured region, all events within the borders of the (p,n) peak, including the (p,γ) events, were summed up. The shape of the (p,n) distribution was found to be symmetric for mirroring it to its x- and y-axis within $<$1 % of discrepancy with MOCADI simulations. Therefore, to obtain the number of events in zone 1-3, the measured counterpart regions were counted once more. The problematic part of the (p,n) distribution is zone 4, from which there is no direct measurement information. Therefore, to constrain the number of events in zone 4, a lower estimate and an upper estimate were calculated. As a lower estimate, it was assumed that there are 0 (p,n) events in that region. This is a realistic lower limit, motivated by the count rate on the y=16 strip within the (p,n) distribution. The number of counts in that strip is compatible with zero level and the number of counts per bin is rapidly decreasing with

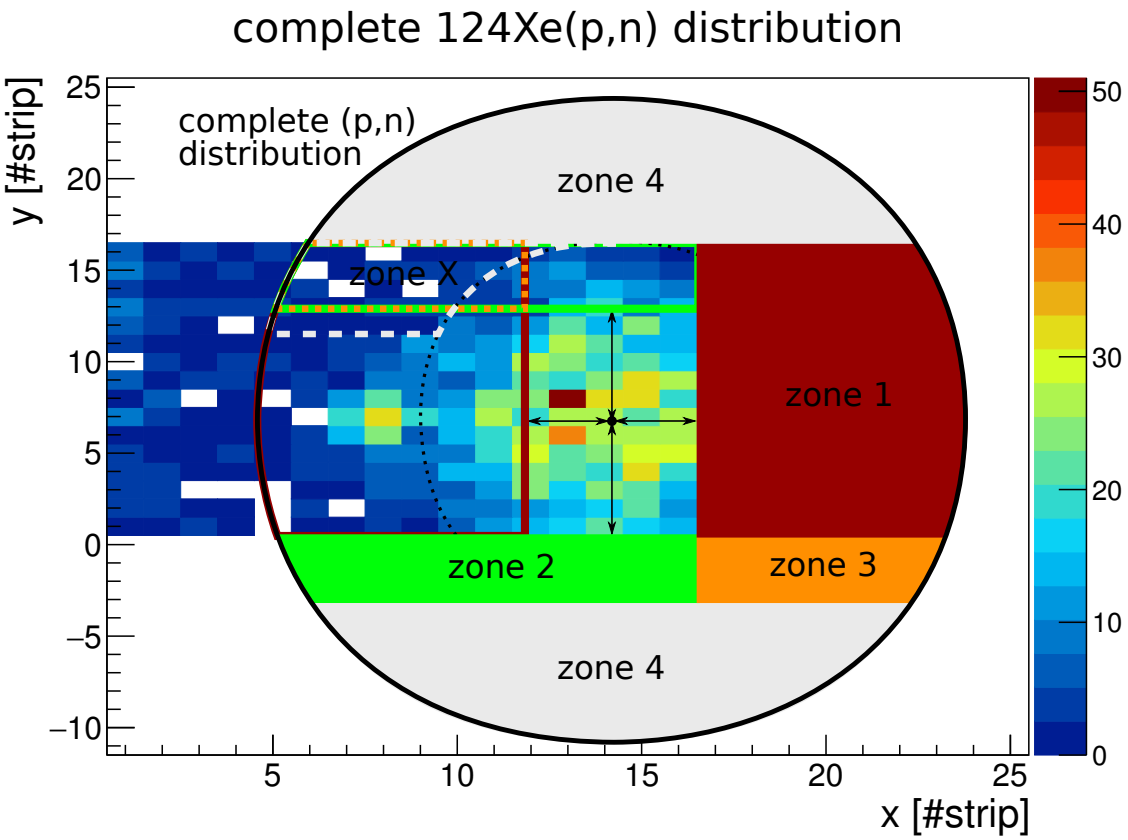

Figure 5.12: The measured and missing parts of the ^{124}Xe(p,n) distribution are shown. To estimate the number of events in the missing sections a Monte Carlo simulation was performed. For more details, see text.

the distance from the center of the (p, n) distribution. Estimating the upper limit is more complicated. As a best estimate, the upper limit on the average number of counts in zone X was employed. The area of zone X excludes the (p, γ) peak, and bounded by the size of the complete (p, n) distribution. In addition, zone X excludes all kinematically possible scattering cones of the (p, n) events, which do not reach zone 4. With this choice it is ensured that the average number of counts within zone X is around at the same level of zone 4 or even slightly higher due to the distortion of the (p, n) distribution after passing through the dipole magnet, see Chapter 5.5.1. To estimate the uncertainty on the (p, n) counts due to its uncertain location, the Monte Carlo simulation treated the coordinates of the center of the (p, n) distribution as random variables. The result of the simulation for the ^{124}Xe dataset is shown in Figure 5.13 and for the ^{118}Te dataset in Figure 5.14. The counts within the integrated regions are taken as the average of the central position of two simulated peaks corresponding to the minimum and maximum count rate estimation in zone 4.

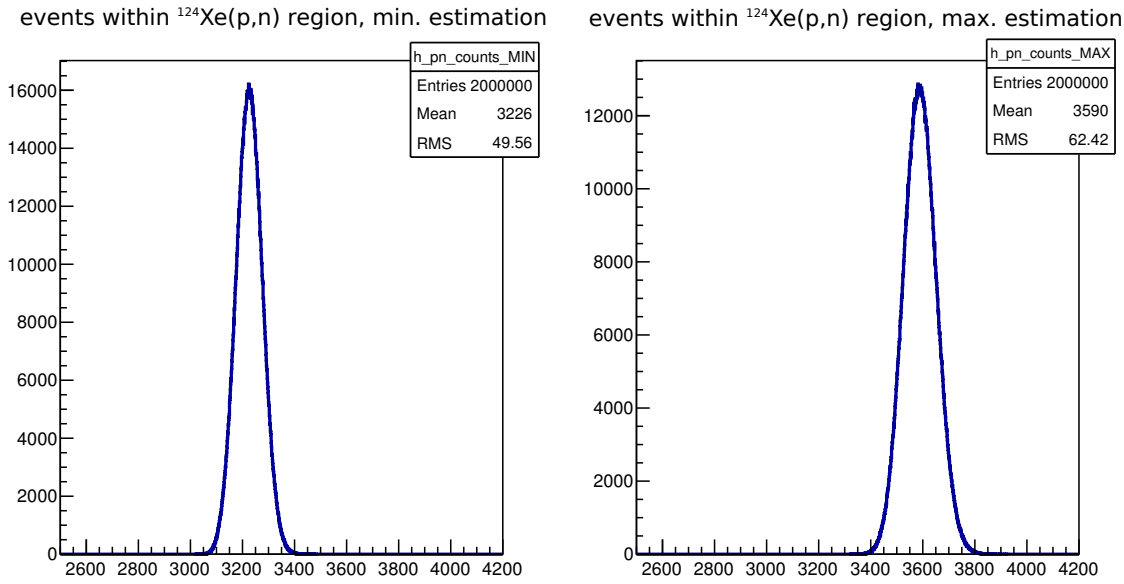

Figure 5.13: The number of events within ^{124}Xe(p,n) spot was determined through a Monte Carlo simulations which treated the missing regions of the (p, n) distribution as "mirrored" measurement regions. For the regions, which were not covered by the DSSSD a minimum and a maximum estimation was given. For more details, please see text.

It is important to subtract from the obtained number of events twice the counts of the (p, γ) events and an estimated Rutherford background. The boundary of the back-scattered Rutherford distribution is not precisely known, since its determination would require much larger statistics. However, from simulations it can be estimated to be between the x=10-12 strips. For the ^{124}Xe dataset, the count rate of the back-scattered Rutherford background is known from the complex fit of the (p, γ) peak. For the ^{118}Te dataset, the Rutherford background was estimated in the region between the (p, γ) peak and the second strip where only the backscattered Rutherford events are present.

Accordingly, the number of (p, n) events for the ^{124}Xe dataset has been obtained as $N_{^{124}\mathrm{Xe(p,n)}} = 2779 \pm 57_{stat} \pm 205_{syst}$ and the number of (p, n) events for the ^{118}Te dataset has been obtained as $N_{^{118}\mathrm{Te(p,n)}} = 143 \pm 13_{stat} \pm 20_{syst}$. By dividing the number of (p, n) events by the luminosity ($L_{int.}$) given in Table 5.2, the cross section of the ^{124}Xe(p,n) reaction was determined

$$\sigma_{^{124}\mathrm{Xe(p,n)}}(E_{CM} = 10.06(1)\,\mathrm{MeV}) = 468.9 \pm 9.6_{stat} \pm 42.2_{syst}\,\mathrm{mb}. \tag{5.15}$$

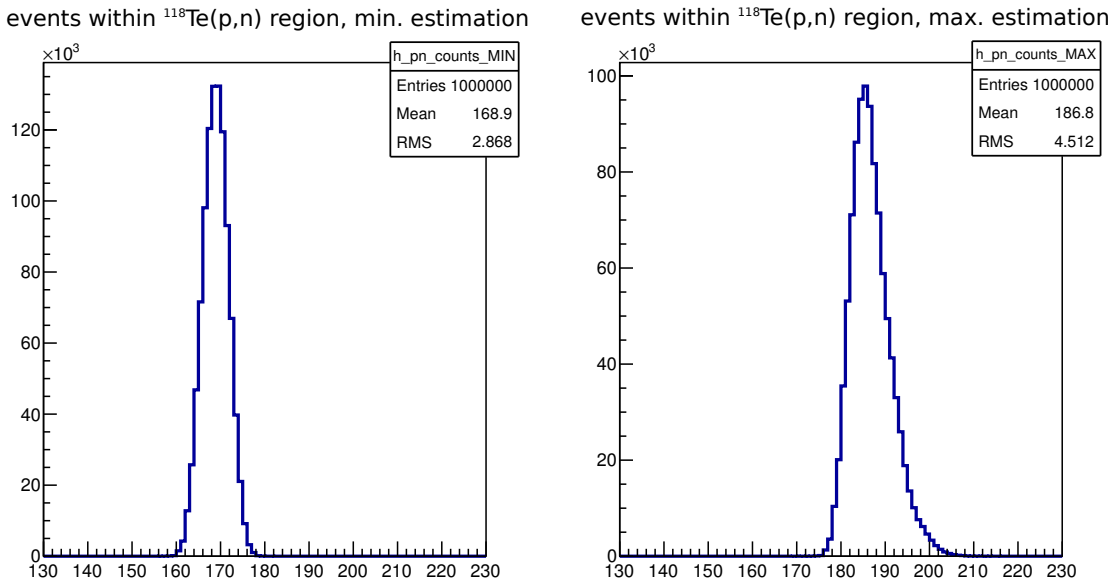

Figure 5.14: The number of events within the ^{118}Te(p,n) spot was determined by the Monte Carlo simulations analogously to the number of ^{124}Xe(p,n) events. For detailed description, see text.

The cross section of the ^{118}Te(p,n) reaction has been determined

$$\sigma_{^{118}\mathrm{Te(p,n)}}(E_{CM} = 10.05(1)\,\mathrm{MeV}) = 403.2 \pm 36.8_{stat} \pm 63.8_{syst}\,\mathrm{mb}. \tag{5.16}$$

The statistical uncertainty is derived from the uncertainty of the measured events according to Poisson statistics. The systematic uncertainty contains multiple components. The leading term is in the order of ∼10 % and corresponds to the difference between the minimum and the maximum estimations for the (p, n) counts. This relatively large uncertainty is not unexpected, since there was no direct or even indirect measurement for the count rate in zone 4, while it covers around the ∼34 % area of the complete (p, n) distribution. Furthermore, the systematic uncertainty also includes the position uncertainty of the (p, n) peak in the Monte Carlo simulations, which is in order of ∼2 %. The systematic uncertainty includes also the uncertainty of the double subtraction of the (p, γ) counts. This component for the ^{124}Xe dataset is around ∼1 %, and for the ^{118}Te dataset reaches ∼5 %. In addition, the systematic uncertainty includes the uncertainty of the luminosity measurement, which is in order of ∼5 % and ∼8 % for the ^{124}Xe and ^{118}Te datasets, respectively. The measured cross section of the ^{124}Xe(p,n) reaction is discussed in the context of the previous (p, γ) and (p, n) measurements at ESR in 2016 [9] in Chapter 6.2. All cross sections determined in this work are given in Table 6.1.

Chapter 6

Conclusion and outlook

In this chapter, the results, obtained in the current thesis, are summarized. In addition, an outlook is given discussing future proton-capture measurements at ESR and CRYRING at GSI.

6.1 Ion identification with the DSSSD

In Chapter 4.4, the performance of the here employed DSSSD was investigated. The performance of the detector was characterized by the so-called "identification efficiency". From a given number of ion hits it defines how much valid ion hits are registered by the DSSSD. It is important to know this ratio precisely, since if identification efficiency of the detector is not close to 100 %, a significant number of the ion hits are not considered, which can lead to incorrect calculation of the reaction cross sections.

The ratio has been quantified for the U_{bias}=-60 V dataset of the E108b experiment at E_{CM} = 6.96 MeV when using a W1-type double sided silicon detector (DSSSD) manufactured by Micron Semiconductor Ltd [130]. A detailed description of the applied setting on the DSSSD can be found in Chapter 4.4. During the investigation, the number of non-identified events has been found to be negligible. Thus the identification efficiency of the DSSSD exceeds >99.975 %. This result implies that the measured number of ion events in the DSSSD spectra is indeed the true number of ions reaching the sensitive surface of the detector.

The obtained result is not unexpected. By looking at the energy spectrum of the strips of the DSSSD it was clear, that the ions, which penetrate into the detector medium, generate signals significantly above the level of the electric noise. In future measurements, similar settings can be applied for an identical DSSSD as were described for the investigated dataset.

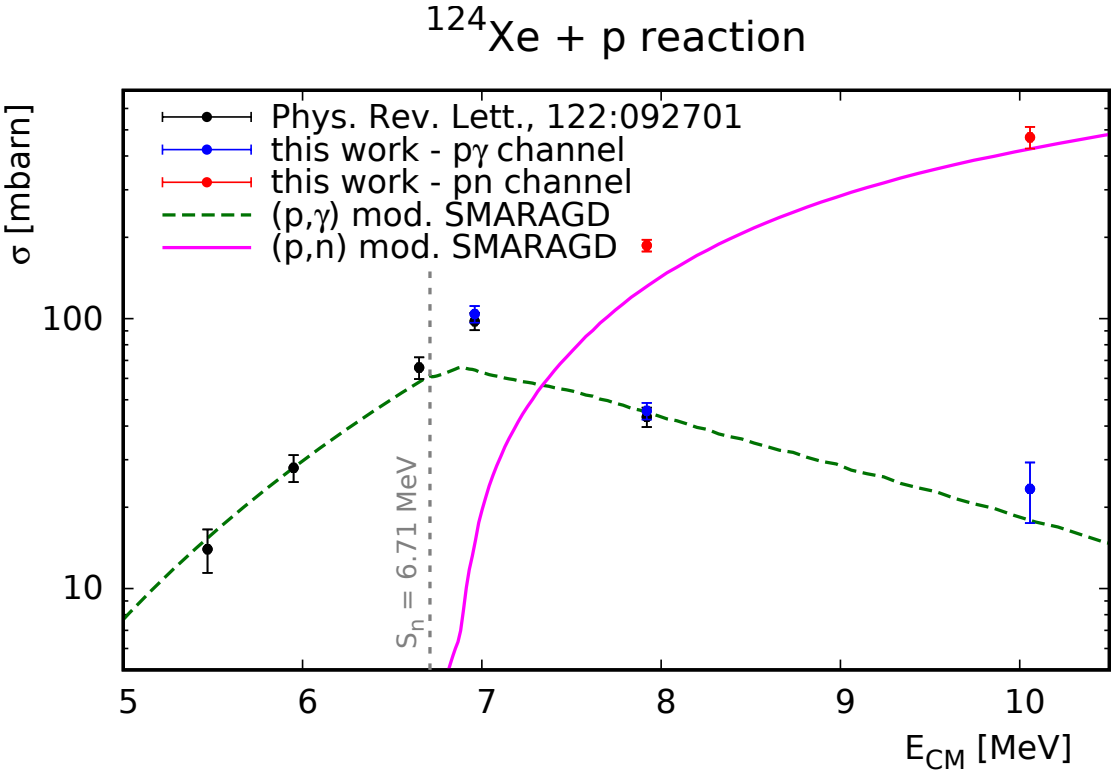

Figure 6.1: The combined datasets of the E108b and E127 experiments for the ^{124}Xe+p reaction for E_{CM} = 5.47 - 10.06 MeV. The experimental results of the E108b experiment were investigated in the framework of the Hauser-Feshbach model. The newly obtained cross section values for 8 MeV and 10 MeV are within the expected variance of the HF SMARAGD code.

6.2 Combined results of the ^{124}Xe(p,x) reactions for E_{CM} = 5.47 - 10.06 MeV

The ^{124}Xe+p reaction has been investigated two times at GSI, between $E_{CM} = 5.5 - 8$ MeV in the framework of the E108b experiment and for $E_{CM} = 10$ MeV in the E127 experiment. The experiments focused on the measurement of two nuclear channels of the reaction, namely on the (p, γ) and (p, n) channels. The experimental cross sections of the associated ^{124}Xe(p,γ) and ^{124}Xe(p,n) reactions are shown in Figure 6.1. All cross section values determined in this work are summarized quantitatively in Table 6.1. The measured dataset of the ^{124}Xe(p,γ)^{125}Cs reaction for $E_{CM} = 6.96$ MeV and 7.92 MeV has been evaluated two times: in the corresponding publication [9] and in this work by applying a method described in Chapter 3.2.4. The results are found to be in good agreement.

Experiment	Beam	E_{CM} [MeV]	Reaction	$\sigma(E_{CM})$ [mbarn]
E108b	$^{124}Xe^{54+}$	6.96(1)	(p,γ)	$103.9 \pm 2.0_{stat} \pm 7.1_{sys}$
		7.92(1)	(p,γ)	$45.5 \pm 1.6_{stat} \pm 2.8_{sys}$
			(p,n)	$186.5 \pm 2.7_{stat} \pm 8.9_{sys}$
E127		10.06(1)	(p,γ)	$23.4 \pm 3.3_{stat} \pm 4.9_{sys}$
			(p,n)	$468.9 \pm 9.6_{stat} \pm 42.2_{sys}$
	$^{118}Te^{52+}$	10.05(1)	(p,γ)	$35.7 \pm 12.5_{stat} \pm 5.4_{sys}$
			(p,n)	$403.2 \pm 36.8_{stat} \pm 63.8_{sys}$

Table 6.1: All cross sections determined in this work are presented. The cross section of the ^{124}Xe(p,x) and ^{118}Te(p,x) reactions for 10MeV/u are determined from the dataset of the recent E127 experiment, while the cross section of the ^{124}Xe(p,x) reactions for 7 MeV/u and 8 MeV/u are obtained by analyzing the E108b experimental dataset [9].

In addition, for the E_{CM} = 8 MeV dataset the distribution of the ^{124}Xe(p,n)^{124}Cs reaction was investigated. Using a simplified cascade scheme of the ^{124}Cs nucleus in the kinematic Monte Carlo simulations, the shape of the measured (p,n) distribution could be reproduced. Thereby, the population of the ^{124}Cs nucleus' states directly after neutron emission could be determined for a continuum binned model. Here, the number of bins in the model are strongly limited by the spatial segmentation of the DSSSD. The method and the results are discussed in Chapter 3.2.6.

Theoretical nuclear cross sections for medium- and heavy-mass nuclei at astrophysical energies are generally discussed in the framework of the the Hauser-Feshbach (HF) formalism [18]. It is a statistical model, which describes the formation of a compound nucleus for high level densities, see Chapter 1.1.2. The experimental cross section values of ^{124}Xe(p,γ) reaction between $E_{CM} = 5.5 - 8$ MeV have been investigated with the HF code SMARAGD [23], which provides astrophysical rate predictions by employing a widely used combination of nuclear models [178,179]. To obtain an improved agreement, the nuclear input parameters of the SMARAGD code relevant for the γ-process [180], were fine-tuned, thereby, establishing a *modified SMARAGD code*. The predictions of this code for the E108b measurement are within the empirical variance for proton-induced reactions, which is about a factor of 2.
The newly calculated experimental cross sections, determined in this thesis, fit well into the discussed HF model. The differences between the model and the experimental values are about 40 % for the ^{124}Xe(p,n) reaction at E_{CM} = 8 MeV, around 65 %

for the ^{124}Xe(p,γ) channel at $E_{CM} = 10\,\mathrm{MeV}$ and about 5 % for the (p, n) channel at $E_{CM} = 10\,\mathrm{MeV}$.
Furthermore, above the neutron-emission threshold, above 6.71 MeV, the predictions for the (p, γ) and (p, n) cross sections are sensitive to the γ- and neutron-widths. Therefore, by utilizing the newly obtained cross section values supplementary restrictions can be given on the nuclear input parameters, which allows the further improvement of the theoretical HF model calculations.

6.3 First proton capture measurement on stored radioactive ions

Within the framework of the E127, for the first time the proton capture has been successfully measured using a stored, radioactive ion beam. $^{118}Te^{52+}$ ions were collided with a pure H_2 gas-jet target at 10.06 MeV/u. The two nuclear channels of the reaction, the (p, γ) and the (p, n) channels, were evaluated by analyzing the spectrum measured by a double sided silicon strip detector (DSSSD). The details of the measurement and of the analysis are discussed in Chapter 5, the obtained cross sections are presented in Table 6.1. The experimental results agree well with the prediction of the HF code TALYS [21] within the empirical variance of for proton-induced reactions, which about a factor 2.
This successful proof-of-principle measurement of the proton-capture on radioactive ions opens the pathway for future experiments to study the radioactive regime of the explosive nucleosynthesis. This is an important milestone to fully understand the production of the neutron-deficit stable isotopes with the lowest abundances, i.e. the origin of the p-nuclei.

6.4 Maximized sensitivity for proton-capture

Reaction studies are essential to model explosive nucleosynthesis, in particular for the poorly understood production of p-nuclei. Experiments in a storage ring at the low, astrophysically relevant energy regime, for which the cross section of the proton capture reactions decreases rapidly, while the Rutherford background simultaneously increases leading to a reduced signal-to-background ratio. In order to improve the measurement sensitivity for the proton capture products, a novel RuthErford Background ELimination experimental scheme, the ERASE technique, has been developed in this work. Using a scraping device in front of the first dipole downstream the gas

jet target, a significant part of the Rutherford scattered particles can be blocked. Thereby, only the back-scattered Rutherford events with low-intensity can reach the position of the (p,γ) cluster on the surface of the DSSSD after the dipole improving the signal-to-background ratio significantly .
The E127 experiment provided the first opportunity to test the ERASE technique. Using the stable ^{124}Xe beam it has been demonstrated that the application of ERASE enables measurement with highest sensitivity for proton-induced reactions in inverse kinematics, in which the background has been reduced by about 91 % for the (p,γ) events.
After the offline energy reconstruction for the DSSSD events, the background can be even further reduced. As a result the proton-capture products can be measured nearly background free. Using the energy information of the DSSSD, the (p,γ) events can be separated from the back-scattered Rutherford background. The feasibility of the method has been demonstrated by carrying out a relative energy calibration together with energy reconstruction for more than 80 % of the DSSSD events using the 7 MeV/u dataset of the E108b experiment, see Chapter 4.4.
However, a reliable energy calibration for the dataset from the E127 experiment could not be realized due to the insufficient statistics. It remains unclear, for example, whether Rutherford events, which re-scattered on the scraping edge, reach the distribution of the (p,γ) events. However, the measured datasets strongly hint that the number of unexpected secondary scattered events is negligible and only the low-intensity back-scattered Rutherford component remains sizeable at the position of the (p,γ) distribution.

6.5 Outlook: The E127b experiment

Due to the unexpected complications with the ESR machine and the extraordinary circumstances in 2020, the proposed E127 experimental scheme, which is normally feasible, could not be reached during the corresponding measurement time. To exhaust the full scientific potential, the proposal of the E127 experiment has been resubmitted for the 2021 beam time schedule at GSI.
Assuming the normal operation of ESR, the commissioning phase can be considerably reduced in comparison to the 10 out of 15 shifts in the E127 experiment. Also, one order of magnitude higher beam intensity can be expectedly achieved at energies in the vicinity of the Gamow window of astrophysical interest, below the (p,n) nuclear reaction channel threshold. The proposed experimental plan has been approved by

the program advisory committee of GSI (G-PAC) and named as E127b experiment. The preparations and the experiment are taking place in May 2021, parallel to the submission of this work. The background suppression technique, the ERASE technique (see Chapter 3.3), and the experiences collected during the energy calibration of the DSSSD (see Chapter 4) serve the success of the E127b experiment in a great extent.

6.6 Outlook: Nuclear astrophysics studies at CRYRING@ESR

Storage rings provide exceptionally clean conditions to study nuclear reactions in inverse kinematics which are essential to understand the evolution of nuclear matter. The CRYRING@ESR [107, 117–119, 181] storage ring serves as the low-energy extension of the ESR machine. Stable or radioactive highly-charged ions with half life more than tens of seconds can be slowed down at ESR and transfered to CRYRING, where the ions are further slowed-down to energies as low as a few hundreds of keV/u. Thereby, the complete energy regime of astrophysical scenarios for corresponding reaction studies can be addressed, see Chapter 2.1.6.

Driven by the high scientific potential, there are several initiatives for the CRYRING@ESR project. In the CARME (CRYRING Array for ReactionMEasurements) project [182–184], for instance, a chamber system is being constructed and installed at CRYRING for high-resolution direct and indirect nuclear and atomic physics measurements. The setup allows precision studies on the angular distribution of the reactions products generated in the interaction between the stored beam and the in-ring target. By simultaneously measuring well-understood atomic physics reactions using X-ray detectors around the target, nuclear cross sections can be reliably normalized.

Other example project at CRYRING@ESR is the NECTAR (Nuclear rEaCTions At storage Rings) project [185, 186]. Within the framework of NECTAR a new methodology is being developed to indirectly infer neutron-induced cross sections of unstable nuclei, which are essential for modeling the nucleosynthesis of most heavy elements in the universe. High resolution surrogate reaction measurements can be realized in inverse kinematics using the environment of an ion storage ring, which provides unstable beams of high quality in combination of ultra thin pure targets. For this purpose, the CRYRING@ESR provides a perfectly suited infrastructure.

Appendix A

MOCADI code of ^{124}Xe(p,γ)^{125}Cs reaction

```
*The code simulates the 124Xe(p,g)125Cs reaction with
*a possible subsequent gamma-cascade
*Manual at https://web-docs.gsi.de/~weick/mocadi/mocadi-manual.html

MOCADI37 GICOSY ESRSTD1M
atima-1.0
option listmode tree
EPAX 2

*BEAM CHARACTERISTICS
BEAM
1000000
7.92699 , 0 , 123.8762682729 , 54
4
0.27386, 0.182573, 0, 0, 0
4
0.131477, 0.383186, 0, 0, 0
1
0.02,  0, 0, 0, 0

SAVE    '0'

MATRIXFILE
/u/lvarga/Dokuments/mocadi/matrix/all/
```

```
*TARGET script made by Dr. Jan Glorius
CALL /u/jglorius/mocadi/reaction.so ext_beam
*M_target M_proj1  M_proj2 switch charge angle_low angle_high
1.0072764668 124.888359033705 0 0 55 0 180  '124Xe+p -> 125Cs_3xs.'
parameters

SAVE    '1'

CALL /u/jglorius/mocadi/reaction.so ext_beam
0 124.885424679804 0 0 55 0 180             '3xs -> 2xs'
parameters

CALL /u/jglorius/mocadi/reaction.so ext_beam
0 124.882490325902 0 0 55 0 180             '2xs -> 1xs.'
parameters

CALL /u/jglorius/mocadi/reaction.so ext_beam
0 124.879555972000 0 0 55 0 180             '1xs -> gs.'
parameters

SAVE    '2'

*FREE TRAVEL FROM TARGET TO QP1
DRIFT
 467.069916
DRIFT
  20.500000
DRIFT
   9.500000

*QUADRUPOLE_2 FIELD
MATRIX                   'ff'
ESRSTD2014001.MAT
123.8762682729, 54, 7.92699
3, 3
```

```
COLL
4, 0, 0,  15.500,  15.500,  15.500
MATRIX                'quadrupole'
ESRSTD2014002.MAT
123.8762682729, 54, 7.92699
3, 3
COLL
4, 0, 0,  15.500,  15.500,  15.500
MATRIX                   'ff'
ESRSTD2014003.MAT
123.8762682729, 54, 7.92699
3, 3

*FREE TRAVEL FROM QP1 TO QP2
DRIFT
   9.500000
DRIFT
  32.490001
DRIFT
   9.500000

*QUADRUPOLE_2 FIELD
MATRIX                   'ff'
ESRSTD2014004.MAT
123.8762682729, 54, 7.92699
3, 3
COLL
4, 0, 0,  15.500,  15.500,  15.500
MATRIX                'quadrupole'
ESRSTD2014005.MAT
123.8762682729, 54, 7.92699
3, 3
COLL
4, 0, 0,  15.500,  15.500,  15.500
MATRIX                   'ff'
ESRSTD2014006.MAT
```

```
123.8762682729, 54, 7.92699
3, 3

*FREE TRAVEL FROM QP TO DIPOLE
DRIFT
        56.02

*SCRAPING POSITION
SAVE    '3'

DRIFT
        49
DRIFT
        105.75

*DIPOLE FIELD
MATRIX                  'ff'
ESRSTD2014007.MAT
123.8762682729, 54, 7.92699
3, 3
COLL
1, 0, 0,  20.000,   3.500, 0
MATRIX                'dipole'
ESRSTD008A1.MAT
123.8762682729, 54, 7.92699
1, 1

*DETECTOR POSITION
SAVE    '4'

END
```

Appendix B

Technical drawings of the scraping system

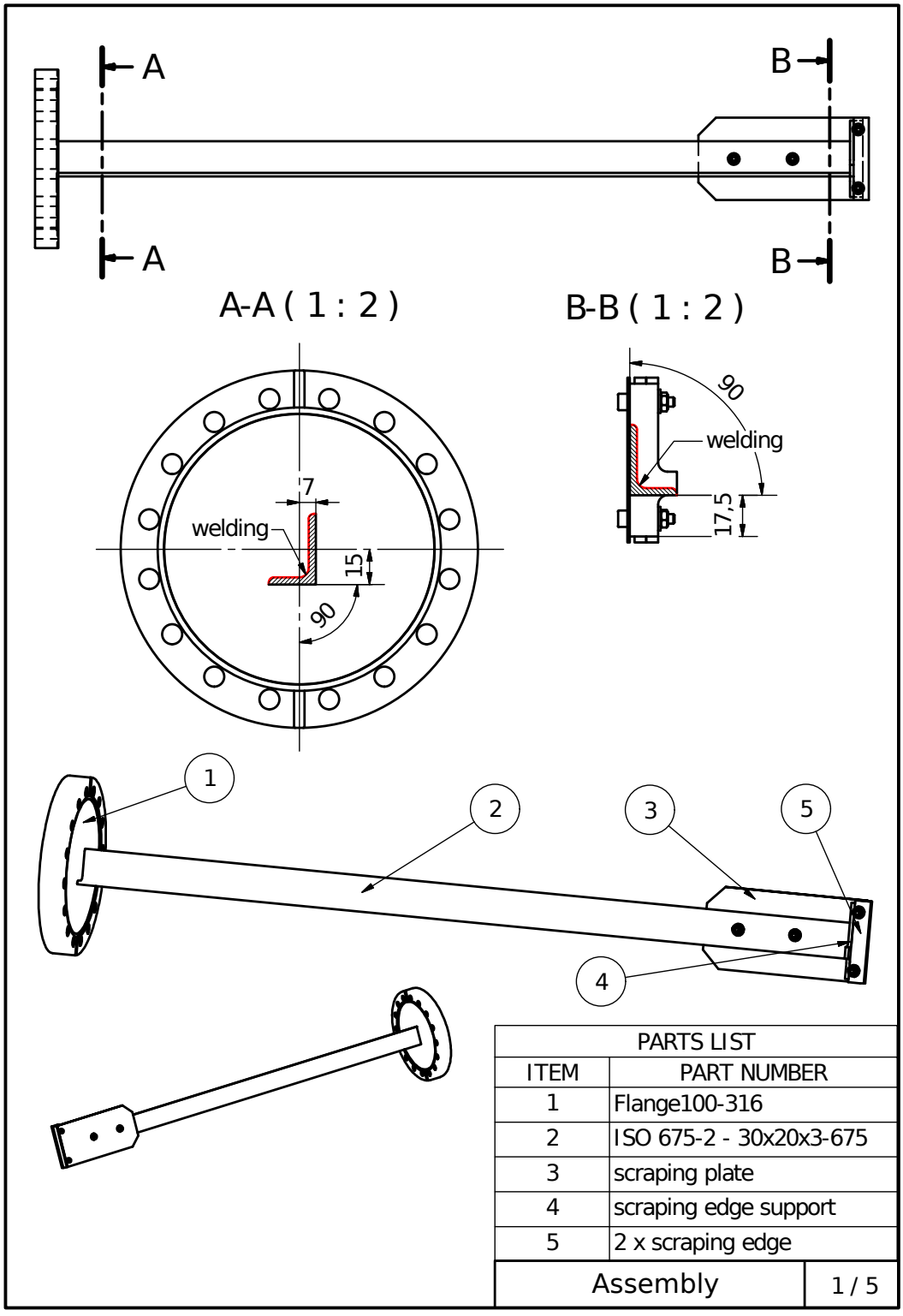

PARTS LIST	
ITEM	PART NUMBER
1	Flange100-316
2	ISO 675-2 - 30x20x3-675
3	scraping plate
4	scraping edge support
5	2 x scraping edge
Assembly	1 / 5

Figure B.1: Assembly of the scraper device

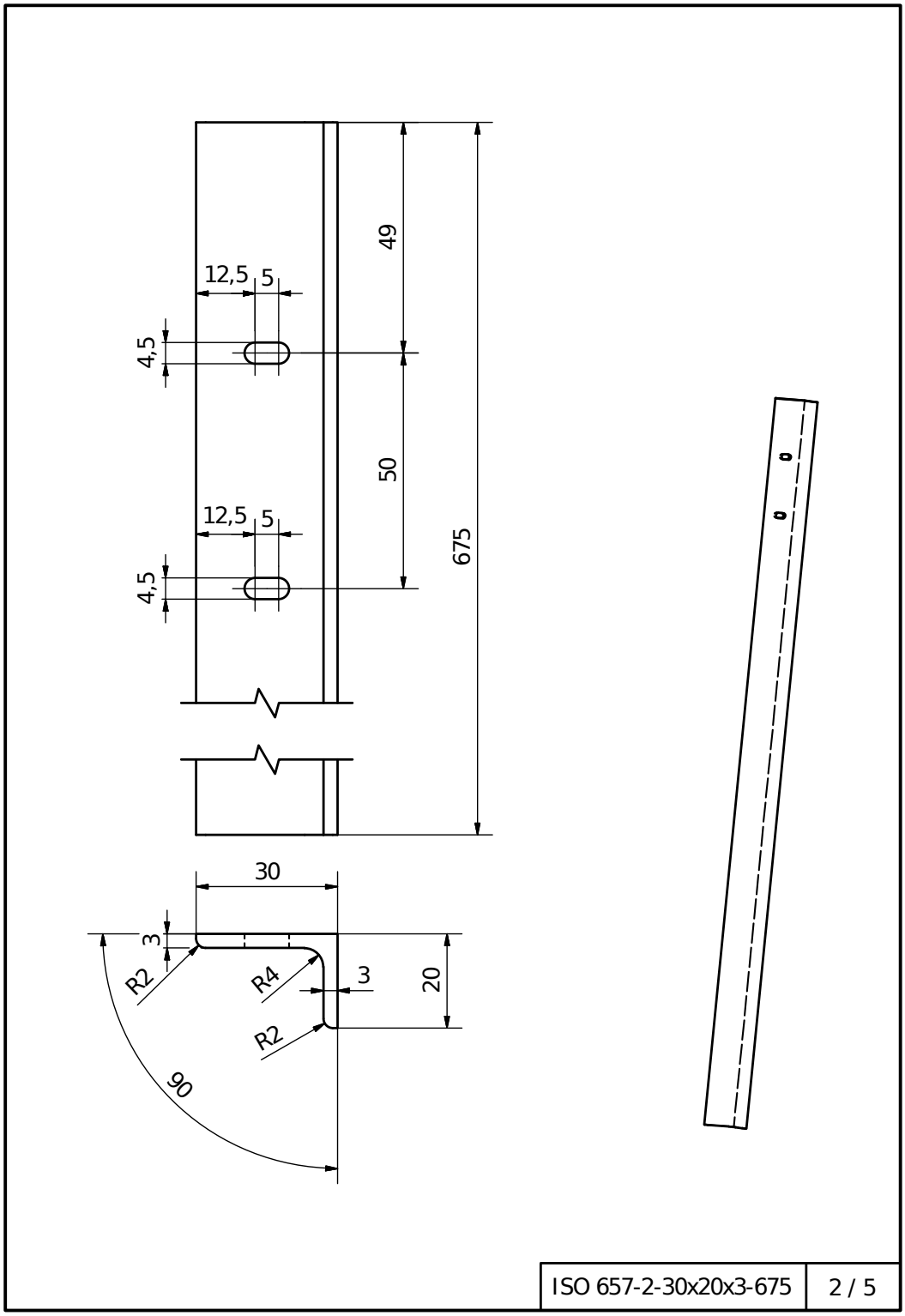

Figure B.2: The support arm of the scraper device

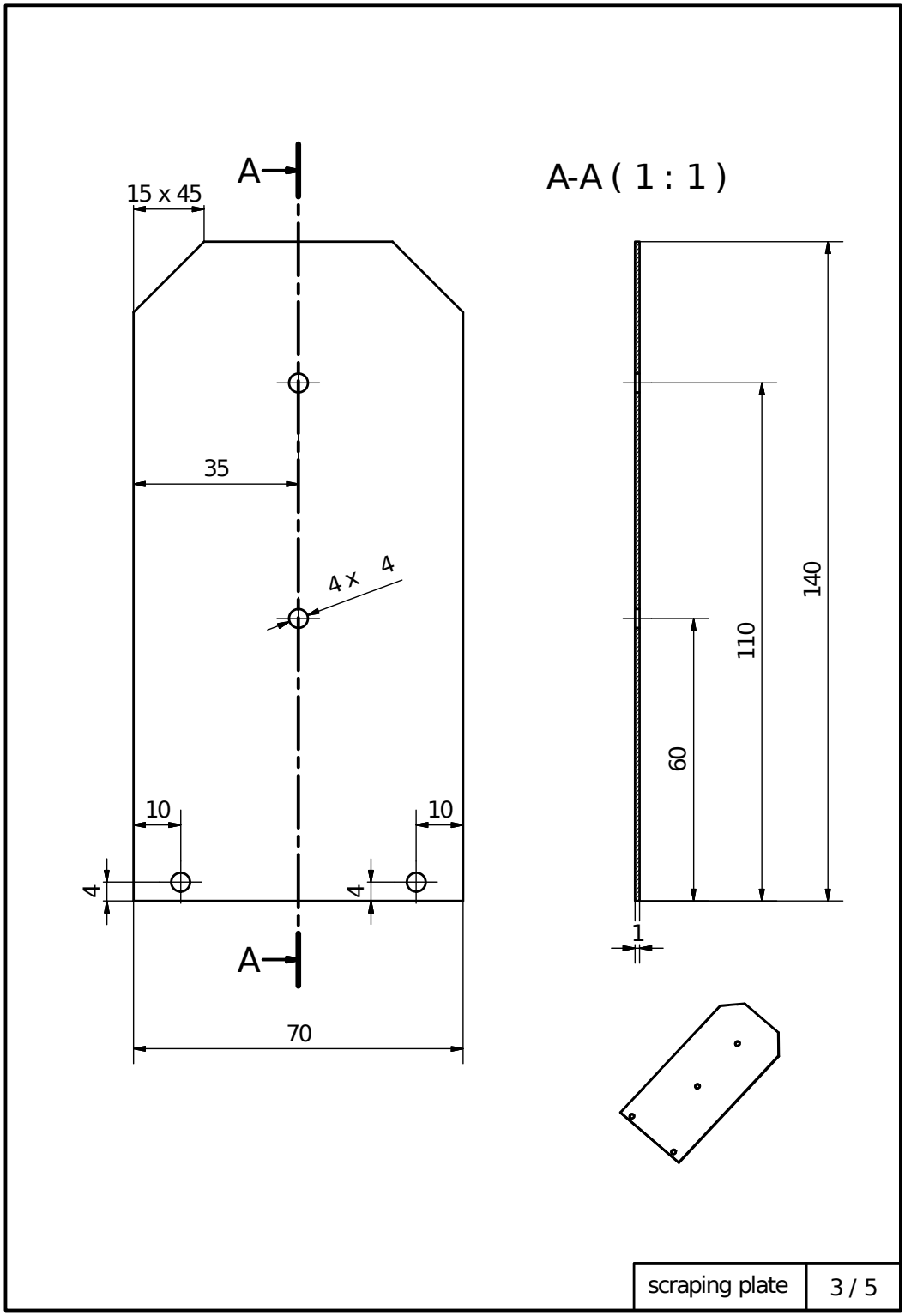

Figure B.3: The scraping plate

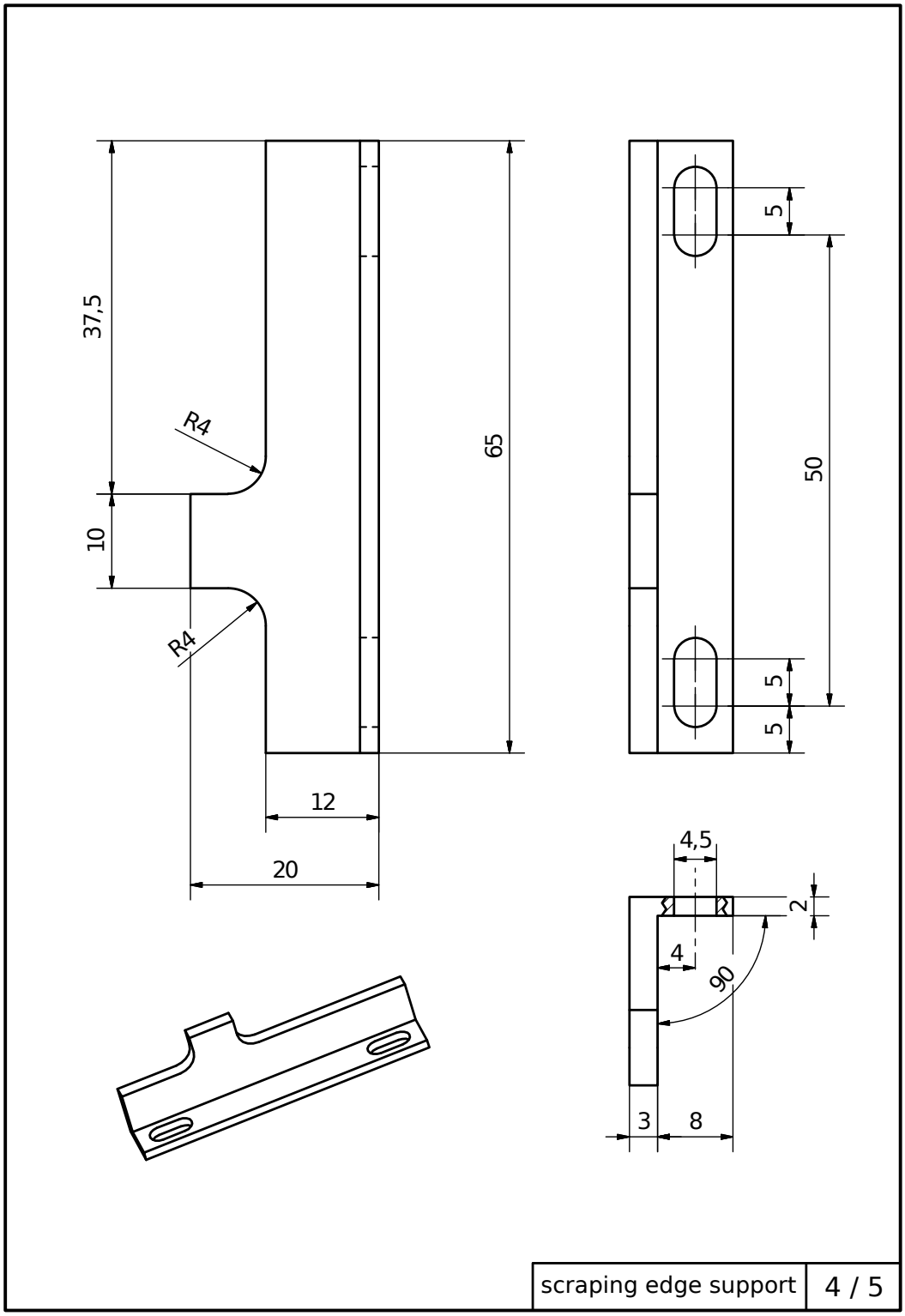

Figure B.4: The scraping edge holder

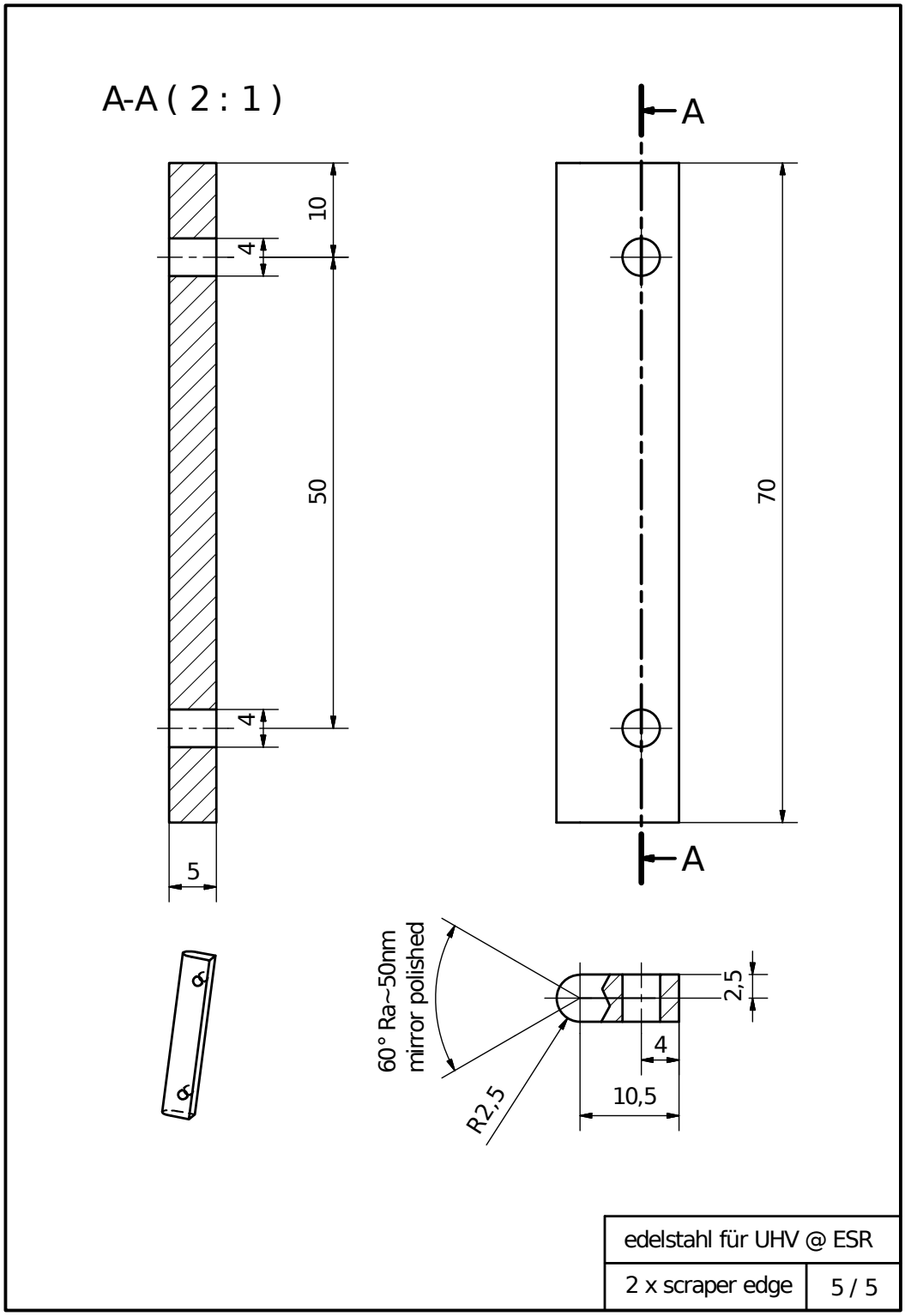

Figure B.5: The high-quality scraping edges

List of publications

1. László Varga et al 2020 Towards background-free studies of capture reaction in a heavy-ion storage ring *J. Phys.: Conf. Ser.* **1668** 012046
   cited as [147]

2. Y.M. Xing et al 2020 Determination of luminosity for in-ring reactions: A new approach for the low-energy domain *Nucl. Instrum. Methods A* **982** 164367
   cited as [134]

3. A. Henriques et al 2020 First investigation of the response of solar cells to heavy ions above 1 AMeV *Nucl. Instrum. Methods A* **969** 163941
   cited as [149]

4. Kathrin Göbel et al 2020 Coulomb dissociation of ^{16}O into ^{4}He and ^{12}C *J. Phys.: Conf. Ser.* **1668** 012016

5. J. Glorius et al 2019 Approaching the Gamow Window with Stored Ions: Direct Measurement of $^{124}\mathrm{Xe}(p,\gamma)$ in the ESR Storage Ring *Phys. Rev. Lett.* **122** 092701
   cited as [9]

In addition, Chapter 6 summarizes the new results derived in this work by the author for the first time.

References

[1] Paul Davies. *The Accidental Universe*. Cambridge University Press, 1982. ISBN: 0521242126.

[2] J. MacDonald and D. J. Mullan. Big bang nucleosynthesis: The strong nuclear force meets the weak anthropic principle. *Physical Review D*, 80(4), Aug 2009.

[3] L. A. Barnes. The fine-tuning of the universe for intelligent life. *Publications of the Astronomical Society of Australia*, 29(4):529–564, 2012.

[4] Carr, B., Rees, M. The anthropic principle and the structure of the physical world. *Nature* 278, 605-612 (1979). `https://doi.org/10.1038/278605a0`.

[5] S. M. Barr and Almas Khan. Anthropic tuning of the weak scale and of m_u/m_d in two-higgs-doublet models. *Phys. Rev. D*, 76:045002, Aug 2007.

[6] Livio, M., Hollowell, D., Weiss, A. et al. The anthropic significance of the existence of an excited state of ^{12}C. *Nature* 340, 281-284 (1989). `https://doi.org/10.1038/340281a0`.

[7] Nuclear Physics of Stars, C. Iliadis, 23 February 2007, $Wiley-VCH, Weinheim$ (2007) , `https://doi.org/10.1002/9783527618750`.

[8] Bo Mei, Thomas Aumann, Shawn Bishop, Klaus Blaum, Konstanze Boretzky, Fritz Bosch, Carsten Brandau, Harald Braeuning, Thomas Davinson, Iris Dillmann, Christina Dimopoulou, Olga Ershova, Zsolt Fueloep, Hans Geissel, Jan Glorius, Gyoergy Gyuerky, Michael Heil, Franz Kaeppeler, Aleksandra Kelic-Heil, Christophor Kozhuharov, Christoph Langer, Tudi Le Bleis, Yuri Litvinov, Gavin Lotay, Justyna Marganiec, Gottfried Muenzenberg, Fritz Nolden, Nikolaos Petridis, Ralf Plag, Ulrich Popp, Ganna Rastrepina, René Reifarth, Bjoern Riese, Catherine Rigollet, Christoph Scheidenberger, Haik Simon, Kerstin Sonnabend, Markus Steck, Thomas Stoehlker, Tamás Szuecs, Klaus Suemmerer, Guenter Weber, Helmut Weick, Danyal Winters, Natalya Winters, Philip

Woods, and Qiping Zhong. First measurement of the ^{96}Ru(p,γ)^{97}Rh cross section for the p process with a storage ring. *Phys. Rev. C*, 92:035803, Sep 2015.

[9] J. Glorius, C. Langer, Z. Slavkovská, L. Bott, C. Brandau, B. Brueckner, K. Blaum, X. Chen, S. Dababneh, T. Davinson, P. Erbacher, S. Fiebiger, T. Gaßner, K. Goebel, M. Groothuis, A. Gumberidze, G. Gyuerky, M. Heil, R. Hess, R. Hensch, P. Hillmann, P.-M. Hillenbrand, O. Hinrichs, B. Jurado, T. Kausch, A. Khodaparast, T. Kisselbach, N. Klapper, C. Kozhuharov, D. Kurtulgil, G. Lane, C. Lederer-Woods, M. Lestinsky, S. Litvinov, Yu. A. Litvinov, B. Loeher, F. Nolden, N. Petridis, U. Popp, T. Rauscher, M. Reed, R. Reifarth, M. S. Sanjari, D. Savran, H. Simon, U. Spillmann, M. Steck, T. Stoehlker, J. Stumm, A. Surzhykov, T. Szuecs, T. T. Nguyen, A. Taremi Zadeh, B. Thomas, S. Yu. Torilov, H. Toernqvist, M. Traeger, C. Trageser, S. Trotsenko, L. Varga, M. Volknandt, H. Weick, M. Weigand, C. Wolf, P. J. Woods, and Y. M. Xing. Approaching the gamow window with stored ions: Direct measurement of ^{124}Xe(p,γ) in the ESR storage ring. *Phys. Rev. Lett.*, 122:092701, Mar 2019.

[10] Professor Eric Sheldon. An Introduction to Nuclear Astrophysics, by R.N. Boyd. *Contemporary Physics*, 50(6):662–663, 2009.

[11] T Rauscher, Nicolas Dauphas, Iris Dillmann, C Fröhlich, Zs Fülöp, and György Gyürky. Constraining the astrophysical origin of the p-nuclei through nuclear physics and meteoritic data. *Reports on progress in physics. Physical Society (Great Britain)*, 76:066201, 05 2013.

[12] T. Rauscher. SENSITIVITY OF ASTROPHYSICAL REACTION RATES TO NUCLEAR UNCERTAINTIES. *The Astrophysical Journal Supplement Series*, 201(2):26, jul 2012.

[13] H. Utsunomiya, P. Mohr, A. Zilges, and M. Rayet. Direct determination of photodisintegration cross sections and the p-process. *Nuclear Physics A*, 777:459–478, 2006. Special Isseu on Nuclear Astrophysics.

[14] ROLFS, C. E., RODNEY, W. S. (1988). Cauldrons in the cosmos: nuclear astrophysics. Chicago, University of Chicago Press.

[15] G. Gamow. Zur quantentheorie des atomkernes. *Z. Physik*, 51:204–212, 1928.

[16] N. Bohr, Nature 137 (1936) 344.

[17] V. F. Weisskopf and P. H. Ewing, Phys. Rev. 57 (1940) 472.

[18] W. Hauser and H. Feshbach, Physical Review 87, 366 (1952).

[19] E. Gadioli and P. E. Hodgson, Pre-Equilibrium Nuclear Reactions (Clarendon Press,Oxford, 1992).

[20] D. G. Sargood, Phys. Rep. 93 (1982) 61.

[21] A. J. Koning, S. Hilaire, and M. C. Duijvestijn. Talys: Comprehensive nuclear reaction modeling. *AIP Conference Proceedings*, 769(1):1154–1159, 2005.

[22] THOMAS RAUSCHER and FRIEDRICH-KARL THIELEMANN. Tables of nuclear cross sections and reaction rates: An addendum to the paper "astrophysical reaction rates from statistical model calculations". *Atomic Data and Nuclear Data Tables*, 79(1):47–64, Sep 2001.

[23] THOMAS RAUSCHER. The path to improved reaction rates for astrophysics. *International Journal of Modern Physics E*, 20(05):1071–1169, May 2011.

[24] Thomas Rauscher. The Path to Improved Reaction Rates for Astrophysics. *Int. J. Mod. Phys. E*, 20:1071–1169, 2011.

[25] Katharina Lodders. Solar system abundances and condensation temperatures of the elements. *The Astrophysical Journal*, 591:1220–1247, 07 2003.

[26] Alain Coc and Elisabeth Vangioni. Primordial nucleosynthesis. *International Journal of Modern Physics E*, 26(08):1741002, 2017.

[27] E. Margaret Burbidge, G. R. Burbidge, William A. Fowler, and F. Hoyle. Synthesis of the Elements in Stars. *Rev. Mod. Phys.*, 29:547–650, Oct 1957.

[28] A. G. W. Cameron. Nuclear Reactions in Stars and Nucleogenesis. *Publications of the Astronomical Society of the Pacific*, 69:201, jun 1957.

[29] W. Rapp, J. Gorres, M. Wiescher, H. Schatz, and F. Kappeler. Sensitivity ofp-process nucleosynthesis to nuclear reaction rates in a 25M⊙supernova model. *The Astrophysical Journal*, 653(1):474–489, dec 2006.

[30] G. Audi, F. G. Kondev, Meng Wang, W.J. Huang, and S. Naimi. The NUBASE2016 evaluation of nuclear properties. *Chinese Physics C*, 41(3):030001, mar 2017.

[31] Klaus Blaum. High-accuracy mass spectrometry with stored ions. *Physics Reports*, 425(1):1–78, 2006.

[32] M. Arnould, S. Goriely, and K. Takahashi. The r-process of stellar nucleosynthesis: Astrophysics and nuclear physics achievements and mysteries. *Phys. Rept.*, 450:97–213, 2007.

[33] Anna Frebel and Timothy C. Beers. The formation of the heaviest elements. *Physics Today*, 71(1):30–37, 2018.

[34] B. P. Abbott et al. Gw170817: Observation of gravitational waves from a binary neutron star inspiral. *Phys. Rev. Lett.*, 119:161101, Oct 2017.

[35] Siegel, Daniel M. Gw170817 –the first observed neutron star merger and its kilonova: Implications for the astrophysical site of the r-process. *Eur. Phys. J. A*, 55(11):203, 2019.

[36] Hansen C.J. Selsing J. et al. Watson, D. Identification of strontium in the merger of two neutron stars. *Nature*, 574:497–500, 2019.

[37] J. Lattimer, F. Mackie, D. Ravenhall, and D. Schramm. The decompression of cold neutron star matter. *ApJ*, 213, 05 1977.

[38] Livio M. Piran T. et al. Eichler, D. Nucleosynthesis, neutrino bursts and γ-rays from coalescing neutron stars. *Nature*, 340, 1989.

[39] C. Freiburghaus, S. Rosswog, and F.-K. Thielemann. r-Process in Neutron Star Mergers. *The Astrophysical Journal*, 525(2):L121–L124, nov 1999.

[40] Arnold I. Boothroyd. Heavy Elements in Stars. *Science*, 314(5806):1690–1691, 2006.

[41] M. Pignatari, R. Gallino, M. Heil, M. Wiescher, F. Käppeler, F. Herwig, and S. Bisterzo. THE WEAKs-PROCESS IN MASSIVE STARS AND ITS DEPENDENCE ON THE NEUTRON CAPTURE CROSS SECTIONS. *The Astrophysical Journal*, 710(2):1557–1577, feb 2010.

[42] K. Wisshak R. Gallino M. Lugaro M. Busso O. Straniero C. Arlandini, F. Käppeler. Neutron capture in low-mass asymptotic giant branch stars: Cross sections and abundance signatures. *The Astrophysical Journal*, 525:886–900, 1999.

[43] C. Theis T. Belgya S. W. Yates Zs. Nemeth, F. Kaeppeler. Nucleosynthesis in the cd-in-sn region. *The Astrophysical Journal*, 426:357–365, 1994.

[44] M. Arnould and S. Goriely. The p-process of stellar nucleosynthesis: astrophysics and nuclear physics status. *Physics Reports*, 384(1):1–84, 2003.

[45] Jean Audouze and J. Truran. P-process nucleosynthesis in postshock supernova envelope environments. *The Astrophysical Journal*, 202:204–213, 10 1975.

[46] S.E. Woosley and W.M. Howard. The p-processes in supernovae. *The Astrophysical Journal*, 36:285–304, February 1978.

[47] M. Rayet, M. Arnould, and N. Prantzos. The p-process revisited. *Astronomy and Astrophysics*, 227(1):271–281, January 1990.

[48] Howard W M, Meyer B S and Woosley S E 1991 A new site for the astrophysical γ -process Astrophys. J. Lett. 373 L5.

[49] T. Rauscher, A. Heger, R. D. Hoffman, and S. E. Woosley. Nucleosynthesis in massive stars with improved nuclear and stellar physics. *The Astrophysical Journal*, 576(1):323–348, sep 2002.

[50] A. Baleisis and W. D. Arnett. A different approach to convective nucleosynthesis. *Nuclear Physics A*, 688(1):185–188, May 2001.

[51] Fujimoto S, Hashimoto M, Koike O, Arai K and Matsuba R, 2003 P-process nucleosynthesis inside supernova-driven supercritical accretion disks Astrophys. J. 585 418-428.

[52] M. Rayet, M. Arnould, M. Hashimoto, N. Prantzos, and K. Nomoto. The p-process in Type II supernovae. *Astronomy and Astrophysics*, 298:517, June 1995.

[53] Thomas Rauscher. Branchings in the γ process path revisited. *Phys. Rev. C*, 73:015804, Jan 2006.

[54] H. Schatz, A. Aprahamian, J. Görres, M. Wiescher, T. Rauscher, J.F. Rembges, F.-K. Thielemann, B. Pfeiffer, P. Möller, K.-L. Kratz, H. Herndl, B.A. Brown, and H. Rebel. rp-process nucleosynthesis at extreme temperature and density conditions. *Physics Reports*, 294(4):167–263, 1998.

[55] H. Schatz, A. Aprahamian, V. Barnard, L. Bildsten, A. Cumming, M. Ouellette, T. Rauscher, F.-K. Thielemann, and M. Wiescher. End point of the *rp* process on accreting neutron stars. *Phys. Rev. Lett.*, 86:3471–3474, Apr 2001.

[56] R. K. Wallace and S. E. Woosley. Explosive hydrogen burning. *The Astrophysical Journal Supplement*, 45:389–420, February 1981.

[57] S. E. Woosley. High energy transients in astrophysics. *AIP Conference Proceedings*, 1983.

[58] PC. Joos A. Ayasli. *Astrophys. J*, 256:637, 1982.

[59] R.E. Taam. *Ann. Rev. Nucl. Sci.*, 35:1, 1985.

[60] W.H.G. Lewin J. van Paradijs M.Y. Fujimoto, M. Sztajno. *Astrophys. J.*, 319:902, 1987.

[61] T.A. Weaver D.Q. Lamb R.E. Taam, SE. Woosley. *Astrophys. J.*, 413:324, 1993.

[62] R.E. Taam W.H.G. Lewin, J. van Paradijs. *Space Sci. Rev.*, 62:233, 1993.

[63] S. E. Woosley and Thomas A. Weaver. Sub–Chandrasekhar Mass Models for Type IA Supernovae. *The Astrophysical Journal*, 423:371, March 1994.

[64] S. Goriely, J. José, M. Hernanz, M. Rayet, and M. Arnould. P-process nucleosynthesis during he-detonation in sub-chandrasekhar CO white dwarfs. *Nuclear Physics A*, 718:596–598, 2003.

[65] C. Froehlich, G. Martínez-Pinedo, M. Liebendoerfer, F.-K. Thielemann, E. Bravo, W. R. Hix, K. Langanke, and N. T. Zinner. Neutrino-induced nucleosynthesis of A>64 nuclei: The νp process. *Phys. Rev. Lett.*, 96:142502, Apr 2006.

[66] D. H.; Hoffman R. D.; Haxton W. C. Woosley, S. E.; Hartmann. The ν-process. *Astrophysical Journal*, 356:272, June 1990.

[67] P. Tsagari, M. Kokkoris, E. Skreti, A. G. Karydas, S. Harissopulos, T. Paradellis, and P. Demetriou. Cross section measurements of the ^{89}Y(p,γ)^{90}Zr reaction at energies relevant to p-process nucleosynthesis. *Phys. Rev. C*, 70:015802, Jul 2004.

[68] S. Galanopoulos, P. Demetriou, M. Kokkoris, Sotirios Harissopulos, R. Kunz, M. Fey, J. Hammer, György Gyürky, Zs Fülöp, E. Somorjai, and S. Goriely. The ^{88}Sr(p,γ)^{89}Y reaction at astrophysically relevant energies. *Phys. Rev. C*, 67, 01 2003.

[69] György Gyürky, E. Somorjai, Zs Fulop, Sotirios Harissopulos, P. Demetriou, and T. Rauscher. Proton capture cross section of sr isotopes and their importance for nucleosynthesis of proton-rich nuclides. *Physical Review C*, 64, 09 2001.

[70] A. Spyrou, A. Lagoyannis, P. Demetriou, S. Harissopulos, and H.-W. Becker. Cross section measurements of (p,γ) reactions on pd isotopes relevant to the p process. *Phys. Rev. C*, 77:065801, Jun 2008.

[71] Gy. Gyuerky, Zs. Fueloep, E. Somorjai, M. Kokkoris, S. Galanopoulos, P. Demetriou, S. Harissopulos, T. Rauscher, and S. Goriely. Proton induced reaction cross section measurements on se isotopes for the astrophysical p process. *Phys. Rev. C*, 68:055803, Nov 2003.

[72] F.R. Chloupek, A.StJ. Murphy, R.N. Boyd, A.L. Cole, J. Görres, R.T. Guray, G. Raimann, J.J. Zach, T. Rauscher, J.V. Schwarzenberg, P. Tischhauser, and M.C. Wiescher. Measurements of proton radiative capture cross sections relevant to the astrophysical rp- and γ-processes. *Nuclear Physics A*, 652(4):391–405, 1999.

[73] Gy Gyürky, G G Kiss, Z Elekes, Zs Fülöp, E Somorjai, and T Rauscher. Proton capture cross-section of ^{106,108}Cd for the astrophysical p-process. *Journal of Physics G: Nuclear and Particle Physics*, 34(5):817–825, mar 2007.

[74] S. Harissopulos et al. Cross-section measurements of the ^{93}Nb(p,γ)^{94}Mo reaction at E(p) = 1.4MeV to 4.9MeV relevant to the nucleosynthetic p process. *Phys. Rev. C*, 64:055804, 2001.

[75] G. G. Kiss, Gy. Gyuerky, Z. Elekes, Zs. Fueloep, E. Somorjai, T. Rauscher, and M. Wiescher. ^{70}Ge(p,γ)^{71}As and ^{76}Ge(p,n)^{76}As cross sections for the astrophysical p process: Sensitivity of the optical proton potential at low energies. *Phys. Rev. C*, 76:055807, Nov 2007.

[76] R. T. Guray et al. Measurements of proton induced reaction cross sections on Te-120 for the astrophysical p-process. *Phys. Rev. C*, 80:035804, 2009.

[77] N. Özkan, A.St.J. Murphy, R.N. Boyd, A.L. Cole, M. Famiano, R.T. Güray, M. Howard, L. Şahin, J.J. Zach, R. deHaan, J. Görres, M.C. Wiescher, M.S. Islam, and T. Rauscher. Cross section measurements of the ^{102}Pd(p,γ)^{103}Ag, ^{116}Sn(p,γ)^{117}Sb, and ^{112}Sn(α,γ)^{116}Te reactions relevant to the astrophysical rp- and γ-processes. *Nuclear Physics A*, 710(3):469–485, 2002.

[78] A. Spyrou, H.-W. Becker, A. Lagoyannis, S. Harissopulos, and C. Rolfs. Cross-section measurements of capture reactions relevant to the p process using a 4π γ-summing method. *Phys. Rev. C*, 76:015802, Jul 2007.

[79] J. Bork, H. Schatz, F. Kappeler, and T. Rauscher. Proton capture cross sections of the ruthenium isotopes. *Phys. Rev. C*, 58:524–535, 1998.

[80] T. Sauter and F. Kaeppeler. (p,γ) rates of ^{92}Mo, ^{94}Mo, ^{95}Mo, ^{98}Mo: Towards an experimentally founded database for p-process studies. *Phys. Rev. C*, 55:3127–3138, Jun 1997.

[81] A. Sauerwein, J. Endres, L. Netterdon, A. Zilges, V. Foteinou, G. Provatas, T. Konstantinopoulos, M. Axiotis, S. F. Ashley, S. Harissopulos, and T. Rauscher. Investigation of the reaction ^{74}Ge(p,γ)^{75}As using the in-beam method to improve reaction network predictions for p nuclei. *Phys. Rev. C*, 86:035802, Sep 2012.

[82] E. DRAGULESCU M. PETRE M. DIMA C. PETRE I. PRECUP, C. BADITA. Proton capture cross sections measurements on N=82 nuclei ^{139}La and ^{141}Pr. *Rom. Rep. Phys*, 64:64, 2012.

[83] R. T. Gueray, N. oezkan, C. Yalcin, T. Rauscher, Gy. Gyuerky, J. Farkas, Zs. Fueloep, Z. Halász, and E. Somorjai. Measurements of ^{152}Gd(p,γ)^{153}Tb and ^{152}Gd(p,n)^{152}Tb reaction cross sections for the astrophysical γ process. *Physical Review C*, 91(5), May 2015.

[84] L. Netterdon, A. Endres, S. Goriely, J. Mayer, P. Scholz, M. Spieker, and A. Zilges. Experimental constraints on the γ -ray strength function in ^{90}Zr using partial cross sections of the ^{89}Y(p,γ)^{90}Zr reaction. *Physics Letters B*, 744:358–362, May 2015.

[85] L. Netterdon, A. Endres, G. G. Kiss, J. Mayer, T. Rauscher, P. Scholz, K. Sonnabend, Zs. Toeroek, and A. Zilges. Cross-section measurement of

the ^{130}Ba(p,γ)^{131}La reaction for γ-process nucleosynthesis. *Physical Review C*, 90(3), Sep 2014.

[86] A. Spyrou, S. J. Quinn, A. Simon, T. Rauscher, A. Battaglia, A. Best, B. Bucher, M. Couder, P. A. DeYoung, A. C. Dombos, and et al. Measurement of the ^{90,92}Zr(p,γ)^{91,93}Nb reactions for the nucleosynthesis of elements near A=90. *Physical Review C*, 88(4), Oct 2013.

[87] A. Simon, A. Spyrou, T. Rauscher, C. Froehlich, S. J. Quinn, A. Battaglia, A. Best, B. Bucher, M. Couder, P. A. DeYoung, and et al. Systematic study of (p,γ) reactions on Ni isotopes. *Physical Review C*, 87(5), May 2013.

[88] Gy. Gyuerky, Zs. Fueloep, Z. Halász, G. G. Kiss, and T. Szuecs. Nuclear physics uncertainties of the astrophysical γ-process studied through the ^{64}Zn(p,α)^{61}Cu and ^{64}Zn(p,γ)^{65}Ga reactions. *Journal of Physics: Conference Series*, 940:012005, Jan 2018.

[89] Gy. Gyuerky, M. Vakulenko, Zs. Fueloep, Z. Halász, G.G. Kiss, E. Somorjai, and T. Szuecs. Cross section and reaction rate of determined from thick target yield measurements. *Nuclear Physics A*, 922:112–125, Feb 2014.

[90] C. Nair, A. R. Junghans, M. Erhard, D. Bemmerer, R. Beyer, E. Grosse, K. Kosev, M. Marta, G. Rusev, K. D. Schilling, and et al. Dipole strength in ^{144}Sm studied via (γ,n), (γ,p), and (γ,α) reactions. *Physical Review C*, 81(5), May 2010.

[91] I. Dillmann, L. Coquard, C. Domingo-Pardo, F. Kaeppeler, J. Marganiec, E. Uberseder, U. Giesen, A. Heiske, G. Feinberg, D. Hentschel, and et al. Cross sections for proton-induced reactions on Pd isotopes at energies relevant for theγprocess. *Physical Review C*, 84(1), Jul 2011.

[92] M. Erhard, A. R. Junghans, R. Beyer, E. Grosse, J. Klug, K. Kosev, C. Nair, N. Nankov, G. Rusev, K. D. Schilling, and et al. Photodissociation of p-process nuclei studied by bremsstrahlung-induced activation. *The European Physical Journal A*, 27(S1):135–140, Mar 2006.

[93] F. Heim, P. Scholz, J. Mayer, M. Mueller, and A. Zilges. Constraining nuclear properties in ^{94}Mo via a ^{93}Nb(p,γ)^{94}Mo total cross section measurement. *Phys. Rev. C*, 101:035807, Mar 2020.

[94] F. Heim, P. Scholz, M. Koerschgen, J. Mayer, M. Mueller, and A. Zilges. Insights into the statistical γ-decay behavior of ^{108}Cd via radiative proton capture. *Phys. Rev. C*, 101:035805, Mar 2020.

[95] A. Psaltis, A. Khaliel, E.-M. Assimakopoulou, A. Kanellakopoulos, V. Lagaki, M. Lykiardopoulou, E. Malami, P. Tsavalas, A. Zyriliou, and T. J. Mertzimekis. Cross-section measurements of radiative proton-capture reactions in ^{112}Cd at energies of astrophysical interest. *Phys. Rev. C*, 99:065807, Jun 2019.

[96] A. Khaliel, T. J. Mertzimekis, E.-M. Asimakopoulou, A. Kanellakopoulos, V. Lagaki, A. Psaltis, I. Psyrra, and E. Mavrommatis. First cross-section measurements of the reactions ^{107,109}Ag(p,γ)^{108,110}Cd at energies relevant to the p process. *Phys. Rev. C*, 96:035806, Sep 2017.

[97] V. Foteinou, S. Harissopulos, M. Axiotis, A. Lagoyannis, G. Provatas, A. Spyrou, G. Perdikakis, Ch. Zarkadas, and P. Demetriou. Cross section measurements of proton capture reactions on se isotopes relevant to the astrophysical p process. *Phys. Rev. C*, 97:035806, Mar 2018.

[98] GSI-FAIR Scientific Report 2018. Technical Report GSI Report 2019-1, Darmstadt, 2019.

[99] W Barth, L Dahl, J Glatz, L Groening, S Richter, and S Yaramishev. Development of the UNILAC Towards a Megawatt Beam Injector. 2004.

[100] `https://www.gsi.de/en/work/accelerator_operations/accelerators/unilac/unilac/poststripper.htm`, October 2020.

[101] L. Groening, S. Mickat, A. Adonin, Winfried Barth, Xiaonan Du, Christoph Düllmann, Hendrik Haehnel, Ralph Hollinger, Egon Jaeger, M.S. Kaiser, Ulrich Ratzinger, A. Rubin, Paul Scharrer, Bernhard Schlitt, G. Schreiber, Anja Seibel, R. Tiede, Hartmut Vormann, Chen Xiao, and Cissce Zhang. Upgrade of the unilac for fair. 09 2015.

[102] K. Blasche and B. Franczak. The Heavy ion synchrotron SIS. In *3rd European Particle Accelerator Conference (EPAC 92)*, pages 9–13, 1992.

[103] M. Steiner, K. Blasche, H.-G. Clerc, H. Eickhoff, B. Franczak, H. Geissel, G. Münzenberg, K.-H. Schmidt, H. Stelzer, and K. Sümmerer. Preliminary measurements of sis 18 beam parameters. *Nuclear Instruments and Methods in*

Physics Research Section A: Accelerators, Spectrometers, Detectors and Associated Equipment, 312(3):420–424, 1992.

[104] `https://www.gsi.de/fileadmin/Beschleunigerbetrieb/Dokumente/nominal_intensity_2021-2022.pdf`, 01.03.2020.

[105] C. Scheidenberger and H. Geissel. Penetration of relativistic heavy ions through matter. *Nuclear Instruments and Methods in Physics Research Section B: Beam Interactions with Materials and Atoms*, 135(1):25–34, 1998.

[106] William R Leo. *Techniques for nuclear and particle physics experiments: a how-to approach; 2nd ed.* Springer, Berlin, 1994.

[107] Fritz Bosch, Yu Litvinov, and Thomas Stöhlker. Nuclear physics with unstable ions at storage rings. *Progress in Particle and Nuclear Physics*, 73:84–140, 11 2013.

[108] Yuri A Litvinov and Fritz Bosch. Beta decay of highly charged ions. *Reports on Progress in Physics*, 74(1):016301, dec 2010.

[109] H. Geissel, Th. Schwab, P. Armbruster, J.P. Dufour, E. Hanelt, K.-H. Schmidt, B. Sherrill, and G. Münzenberg. Ions penetrating through ion-optical systems and matter - non-liouvillian phase-space modelling. *Nuclear Instruments and Methods in Physics Research Section A: Accelerators, Spectrometers, Detectors and Associated Equipment*, 282(1):247–260, 1989.

[110] Bethe, H. Bremsformel für Elektronen relativistischer Geschwindigkeit. Z. Physik 76, 293-299 (1932). `https://doi.org/10.1007/BF01342532`.

[111] H. Geissel et al. The GSI projectile fragment separator (FRS): A Versatile magnetic system for relativistic heavy ions. *Nucl. Instrum. Meth. B*, 70:286–297, 1992.

[112] Bernhard Franzke. The heavy ion storage and cooler ring project ESR at GSI. *Nuclear Instruments and Methods in Physics Research Section B: Beam Interactions with Materials and Atoms*, 24-25:18–25, 1987.

[113] Markus Steck and Yuri A. Litvinov. Heavy-ion storage rings and their use in precision experiments with highly charged ions. *Progress in Particle and Nuclear Physics*, 115:103811, 2020.

[114] M. Steck, K. Beckert, F. Bosch, H. Eickhoff, B. Franzke, O. Klepper, F. Nolden, H. Reich, B. Schlitt, P. Spaedtke, and T. Winkler. Cooled heavy ion beams at the ESR. *Nuclear Physics A*, 626(1):495 – 498, 1997. Proceedings of the Third International Conference on Nuclear Physics at Storage Rings.

[115] Thomas Beier, Ludwig Dahl, H.-Jürgen Kluge, Christophor Kozhuharov, and Wolfgang Quint. Trapping ions of hydrogen-like uranium: The hitrap project at gsi. *Nuclear Instruments and Methods in Physics Research Section B: Beam Interactions with Materials and Atoms*, 235(1):473–478, 2005. The Physics of Highly Charged Ions.

[116] F Herfurth, W Barth, G Clemente, L Dahl, P Gerhard, M Kaiser, O Kester, HJ Kluge, S Koszudowski, C Kozhuharov, W Quint, A Sokolov, T Stohlker, J Pfister, U Ratzinger, A Sauer, A Schempp, and G Vorobjev. HITRAP - HEAVY, HIGHLY-CHARGED IONS AND ANTIPROTONS AT REST. *Acta physica Polonica / B*, 41(2):457 – 462, 2010.

[117] K. Abrahamsson, G. Andler, L. Bagge, E. Beebe, P. Carlé, H. Danared, S. Egnell, K. Ehrnstén, M. Engstroem, C.J. Herrlander, J. Hilke, J. Jeansson, A. Kaellberg, S. Leontein, L. Liljeby, A. Nilsson, A. Paal, K.-G. Rensfelt, U. Rosengard, A. Simonsson, A. Soltan, J. Starker, M.af Ugglas, and A. Filevich. CRYRING - a synchrotron, cooler and storage ring. *Nuclear Instruments and Methods in Physics Research Section B: Beam Interactions with Materials and Atoms*, 79(1):269 – 272, 1993.

[118] Michael Lestinsky, Norbert Angert, Ralph Bar, Ralph Becker, Mario Bevcic, Udo Blell, Walter Bock, Angela Braeuning-Demian, Hakan Danared, Oleksiy Dolinskyy, Wolfgang Enders, Mats Engstroem, Achim Fischer, Bernhard Franzke, Georg Gruber, Peter Huelsmann, Anders Kaellberg, Oliver Kester, Carl-Michael Kleffner, Yuri A. Litvinov, Carsten Muehle, Bernhard Muller, Ina Pschorn, Torsten Radon, Heinz Remakers, Hartmut Reich-Sprenger, Dag Reistad, Galina Riefert, Marcus Schwickert, Ansgar Simonson, Jan Sjoholm, Orjan Skeppstedt, Markus Steck, Thomas Stoehlker, Wolfgang Vinzenz and Horst Welker. CRYRING at ESR: A study group report. 2012.

[119] F. Herfurth et al. Commissioning of the Low Energy Storage Ring Facility CRYRING@ESR. In *Proc. of Workshop on Beam Cooling and Related Topics (COOL'17), Bonn, Germany, 18-22 September 2017*, number 11 in Workshop

on Beam Cooling and Related Topics, pages 81–83, Geneva, Switzerland, Jan. 2018. JACoW. https://doi.org/10.18429/JACoW-COOL2017-THM13.

[120] Mei Bai et al. Challenges of FAIR Phase 0. In *9th International Particle Accelerator Conference*, page THYGBF3, 2018.

[121] Horst Stoecker, Thomas Stoehlker, and Christian Sturm. FAIR - cosmic matter in the laboratory. *Journal of Physics: Conference Series*, 623:012026, jun 2015.

[122] H. Stocker. FAIR: Challenges Overcome and Still to be Met. *Conf. Proc. C*, 0806233:moycgm01, 2008.

[123] Green Paper of FAIR: The Modularized Start Version, `https://www.gsi.de/documents/DOC-2009-Nov-124-1.pdf`, October 2009.

[124] M Durante, P Indelicato, B Jonson, V Koch, K Langanke, Ulf-G Meissner, E Nappi, T Nilsson, Th Stoehlker, E Widmann, and M Wiescher. All the fun of the FAIR: fundamental physics at the facility for antiproton and ion research. *Physica Scripta*, 94(3):033001, jan 2019.

[125] Th. Stoehlker, V. Bagnoud, K. Blaum, A. Blazevic, A. Braeuning-Demian, M. Durante, F. Herfurth, M. Lestinsky, Y. Litvinov, S. Neff, R. Pleskac, R. Schuch, S. Schippers, D. Severin, A. Tauschwitz, C. Trautmann, D. Varentsov, and E. Widmann. APPA at FAIR: From fundamental to applied research. *Nuclear Instruments and Methods in Physics Research Section B: Beam Interactions with Materials and Atoms*, 365:680 – 685, 2015. Swift Heavy Ions in Matter, 18 - 21 May, 2015, Darmstadt, Germany.

[126] J. Adamczewski-Musch, P. Akishin, J. Bendarouach, C. Deveaux, M. Duerr, J. Eschke, M. Faul, J. Foertsch, J. Friese, J. Heep, C. Hoehne, D. Ivanishchev, K.-H. Kampert, L. Kochenda, P. Kravtsov, I. Kres, S. Lebedev, E. Lebedeva, S. Linev, T. Mahmoud, M. Malaev, J. Michel, N. Miftakhov, W. Niebur, J.-H. Otto, E. Ovcharenko, V. Patel, C. Pauly, D. Pfeifer, Y. Riabov, E. Roshchin, V. Samsonov, V. Schetinin, O. Tarasenkova, M. Traxler, D. Tyts, M. Vznuzdaev, A.A. Weber, and P. Zumbruch. Status of the CBM and HADES RICH projects at FAIR. *Nuclear Instruments and Methods in Physics Research Section A: Accelerators, Spectrometers, Detectors and Associated Equipment*, 952:161970, 2020. 10th International Workshop on Ring Imaging Cherenkov Detectors (RICH 2018).

[127] J. Aeystoe, K.-H. Behr, J. Benlliure, A. Bracco, P. Egelhof, A. Fomichev, S. Galès, H. Geissel, T. Grahn, L.V. Grigorenko, M.N. Harakeh, R. Hayano, S. Heinz, K. Itahashi, A. Jokinen, N. Kalantar-Nayestanaki, R. Kanungo, H. Lenske, I. Mukha, G. Muenzenberg, C. Nociforo, H.J. Ong, S. Pietri, M. Pfuetzner, W. Plaß, A. Prochazka, S. Purushothaman, T. Saito, C. Scheidenberger, H. Simon, I. Tanihata, S. Terashima, H. Toki, L. Trache, H. Weick, J.S. Winfield, M. Winkler, and V. Zamfir. Experimental program of the super-frs collaboration at fair and developments of related instrumentation. *Nuclear Instruments and Methods in Physics Research Section B: Beam Interactions with Materials and Atoms*, 376:111 – 115, 2016. Proceedings of the XVIIth International Conference on Electromagnetic Isotope Separators and Related Topics (EMIS2015), Grand Rapids, MI, U.S.A., 11-15 May 2015.

[128] M. Destefanis. The panda experiment at fair. *Nuclear Physics B - Proceedings Supplements*, 245:199 – 206, 2013. The Proceedings of the 7th Joint International Hadron Structure'13 Conference.

[129] N. Iwasa, H. Geissel, G. Münzenberg, C. Scheidenberger, Th. Schwab, and H. Wollnik. Mocadi, a universal monte carlo code for the transport of heavy ions through matter within ion-optical systems. *Nuclear Instruments and Methods in Physics Research Section B: Beam Interactions with Materials and Atoms*, 126(1):284 – 289, 1997. International Conference on Electromagnetic Isotope Separators and Techniques Related to Their Applications.

[130] Micron Semiconductor LTD, `http://www.micronsemiconductor.co.uk/strip-detectors-double-sided/`, 01.04.2021.

[131] Catima Physics Manual, A. Prochazka, 2019, `https://isotopea.com/webatima/catima.pdf`.

[132] `https://web-docs.gsi.de/~weick/atima`, 15.10.2020.

[133] Jörg Eichler and Thomas Stöhlker. Radiative electron capture in relativistic ion-atom collisions and the photoelectric effect in hydrogen-like high-Z systems. *Physics Reports*, 439(1):1 – 99, 2007.

[134] Y.M. Xing, J. Glorius, L. Varga, L. Bott, C. Brandau, B. Brückner, R.J. Chen, X. Chen, S. Dababneh, T. Davinson, P. Erbacher, S. Fiebiger, T. Gaßner,

K. Göbel, M. Groothuis, A. Gumberidze, G. Gyürky, M. Heil, R. Hess, R. Hensch, P. Hillmann, P.-M. Hillenbrand, O. Hinrichs, B. Jurado, T. Kausch, A. Khodaparast, T. Kisselbach, N. Klapper, C. Kozhuharov, D. Kurtulgil, G. Lane, C. Langer, C. Lederer-Woods, M. Lestinsky, S. Litvinov, Yu.A. Litvinov, B. Löher, N. Petridis, U. Popp, M. Reed, R. Reifarth, M.S. Sanjari, H. Simon, Z. Slavkovská, U. Spillmann, M. Steck, T. Stöhlker, J. Stumm, T. Szücs, T.T. Nguyen, A. Taremi Zadeh, B. Thomas, S.Yu. Torilov, H. Törnqvist, C. Trageser, S. Trotsenko, M. Volknandt, M. Wang, M. Weigand, C. Wolf, P.J. Woods, Y.H. Zhang, and X.H. Zhou. Determination of luminosity for in-ring reactions: A new approach for the low-energy domain. *Nuclear Instruments and Methods in Physics Research Section A: Accelerators, Spectrometers, Detectors and Associated Equipment*, 982:164367, 2020.

[135] M. Kuhnel, N. Petridis, D. F. A. Winters, U. Popp, R. Dorner, T. Stohlker, and R. E. Grisenti. Low-Z internal target from a cryogenically cooled liquid microjet source. *Nucl. Instrum. Meth. A*, 602:311–314, 2009.

[136] Thomas Rauscher. Relevant energy ranges for astrophysical reaction rates. *Phys. Rev. C*, 81:045807, Apr 2010.

[137] Mazzocco, M., Ackermann, D., Block, M. et al. Extension of the Monte-Carlo code MOCADI to fusion-evaporation reactions. Eur. Phys. J. Spec. Top. 150, 363-364 (2007). `https://doi.org/10.1140/epjst/e2007-00347-8`.

[138] `https://web-docs.gsi.de/~weick/mocadi/index.html#ref4`, 08.12.2020.

[139] Rene Brun and Fons Rademakers, ROOT - An Object Oriented Data Analysis Framework, Proceedings AIHENP'96 Workshop, Lausanne, Sep. 1996, Nucl. Inst. & Meth. in Phys. Res. A 389 (1997) 81-86.

[140] W.J. Huang, G. Audi, Meng Wang, F. G. Kondev, S. Naimi, and Xing Xu. The AME2016 atomic mass evaluation (I). Evaluation of input data; and adjustment procedures. *Chinese Physics C*, 41(3):030002, mar 2017.

[141] Meng Wang, G. Audi, F. G. Kondev, W.J. Huang, S. Naimi, and Xing Xu. The AME2016 atomic mass evaluation (II). tables, graphs and references. *Chinese Physics C*, 41(3):030003, mar 2017.

[142] G. Rodrigues, Paul Indelicato, J. Santos, P. Patté, and F. Parente. Systematic calculation of total atomic energies of ground state configurations. *Atomic Data and Nuclear Data Tables - AT DATA NUCL DATA TABLES*, 86:117–233, 03 2004.

[143] Keh-Ning Huang, Michio Aoyagi, Mau Hsiung Chen, Bernd Crasemann, and Hans Mark. Neutral-atom electron binding energies from relaxed-orbital relativistic Hartree-Fock-Slater calculations $2 \leq Z \leq 106$. *Atomic Data and Nuclear Data Tables*, 18(3):243–291, 1976.

[144] D. R. Plante, W. R. Johnson, and J. Sapirstein. Relativistic all-order many-body calculations of the n=1 and n=2 states of heliumlike ions. *Phys. Rev. A*, 49:3519–3530, May 1994.

[145] M. Steck, P. Beller, K. Beckert, B. Franzke, and F. Nolden. Electron cooling experiments at the ESR. *Nuclear Instruments and Methods in Physics Research Section A: Accelerators, Spectrometers, Detectors and Associated Equipment*, 532(1):357 – 365, 2004. International Workshop on Beam Cooling and Related Topics.

[146] Carlson, B.V. (2003). A brief overview of models of nucleon-induced reactions (INIS-XA–900). Paver, N. (Ed.). International Atomic Energy Agency (IAEA).

[147] László Varga, Thomas Davinson, Jan Glorius, Beatrix Jurado, Christoph Langer, Claudia Lederer-Woods, Yuri A. Litvinov, René Reifarth, Zuzana Slavkovská, Thomas Stöhlker, Phil J. Woods, and Yuan Ming Xing. Towards background-free studies of capture reaction in a heavy-ion storage ring. *Journal of Physics: Conference Series*, 1668:012046, oct 2020.

[148] B.E. Fischer. The heavy-ion microprobe at gsi - used for single ion micromechanics. *Nuclear Instruments and Methods in Physics Research Section B: Beam Interactions with Materials and Atoms*, 30(3):284–288, 1988.

[149] A. Henriques, B. Jurado, J. Pibernat, J.C. Thomas, D. Denis-Petit, T. Chiron, L. Gaudefroy, J. Glorius, Yu.A. Litvinov, L. Mathieu, V. Méot, R. Pérez-Sánchez, O. Roig, U. Spillmann, B. Thomas, B.A. Thomas, I. Tsekhanovich, L. Varga, and Y. Xing. First investigation of the response of solar cells to heavy ions above 1 AMeV. *Nuclear Instruments and Methods in Physics Research Section A: Accelerators, Spectrometers, Detectors and Associated Equipment*, 969:163941, 2020.

[150] L. Grassi, J. Forneris, D. Torresi, L. Acosta, A. Di Pietro, P. Figuera, M. Fisichella, V. Grilj, M. Jakšić, M. Lattuada, T. Mijatović, M. Milin, L. Prepolec, N. Skukan, N. Soić, V. Tokić, and M. Uroić. Study of the inter-strip gap effects on the response of double sided silicon strip detectors using proton micro-beams. *Nuclear Instruments and Methods in Physics Research Section A: Accelerators, Spectrometers, Detectors and Associated Equipment*, 767:99–111, 2014.

[151] M. Reese, J. Gerl, P. Golubev, and N. Pietralla. Automatic intrinsic calibration of double-sided silicon strip detectors. *Nuclear Instruments and Methods in Physics Research Section A: Accelerators, Spectrometers, Detectors and Associated Equipment*, 779:63–68, 2015.

[152] D. Torresi, D. Stanko, A. Di Pietro, P. Figuera, M. Fisichella, M. Lattuada, M. Milin, A. Musumarra, M. Pellegriti, V. Scuderi, E. Strano, and M. Zadro. Influence of the interstrip gap on the response and the efficiency of double sided silicon strip detectors. *Nuclear Instruments and Methods in Physics Research Section A: Accelerators, Spectrometers, Detectors and Associated Equipment*, 713:11–18, 2013.

[153] `https://root.cern.ch/doc/master/classTMinuit.html`, 01.03.2020.

[154] `http://seal.web.cern.ch/seal/documents/minuit/mntutorial.pdf`, 01.03.2020.

[155] `http://seal.web.cern.ch/seal/documents/minuit/mnerror.pdf`, 01.03.2020.

[156] D Torresi, J Forneris, L Grassi, L Acosta, A Di Pietro, P Figuera, L Grilj, M Jaksić, M Lattuada, T Mijatović, M Milin, L Prepolec, N Skukan, N Soić, D Stanko, V Tokić, M Uroić, and M Zadro. Study of interstrip gap effects and efficiency for full energy detection of double sided silicon strip detectors. *Journal of Physics: Conference Series*, 590:012029, apr 2015.

[157] J. Yorkston, A.C. Shotter, D.B. Syme, and G. Huxtable. Interstrip surface effects in oxide passivated ion-implanted silicon strip detectors. *Nuclear Instruments and Methods in Physics Research Section A: Accelerators, Spectrometers, Detectors and Associated Equipment*, 262(2):353–358, 1987.

[158] J.A. Duenas, D. Mengoni, M. Assie, B. Le Crom, A.M. Sánchez Benítez, B. Genolini, Y. Blumenfeld, S. Ancelin, N. de Séréville, T. Faul, F. Hammache, A. Jallat, V. Le Ven, E. Rauly, D. Suzuki, D. Beaumel, and I. Martel. Inter-strip effects influence on the particle identification of highly segmented silicon strip detector in a nuclear reaction scenario. *Nuclear Instruments and Methods in Physics Research Section A: Accelerators, Spectrometers, Detectors and Associated Equipment*, 743:44–50, 2014.

[159] G. Cavalleri, G. Fabri, E. Gatti, and V. Svelto. On the induced charge in semiconductor detectors. *Nuclear Instruments and Methods*, 21:177–178, 1963.

[160] G. Cavalleri, E. Gatti, G. Fabri, and V. Svelto. Extension of ramo's theorem as applied to induced charge in semiconductor detectors. *Nuclear Instruments and Methods*, 92(1):137–140, 1971.

[161] E. Vittone. Theory of ion beam induced charge measurement in semiconductor devices based on the gunn's theorem. *Nuclear Instruments and Methods in Physics Research Section B: Beam Interactions with Materials and Atoms*, 219-220:1043–1050, 2004. Proceedings of the Sixteenth International Conference on Ion Beam Analysis.

[162] `https://www.gsi.de/fileadmin/beamtime/2020/BTS2020_v023_all.pdf`, 29.03.2021.

[163] `https://www.mesytec.com/products/datasheets/MPR-16.pdf`, 01.04.2021.

[164] `http://www.mesytec.com/products/datasheets/MSCF16-F-V.pdf`, 01.04.2021.

[165] D. A. Gedcke and W. J. McDonald, Nucl. Instr. and Meth.55(2): 377 (1967).

[166] D. A. Gedcke and W. J. McDonald,Nucl. Instr. and Meth.58(2): 253 (1968).

[167] `https://www.caen.it/products/v775/`, 01.04.2021.

[168] J. Hoffman, VULOM4b data sheet, 2013, accessed: 25.03.2021. Available: `https://www.gsi.de/fileadmin/EE/Module/VULOM/vulom4B_3.pdf`.

[169] `http://fy.chalmers.se/~f96hajo/trloii/`, 14.04.2021.

[170] `https://www.mesytec.com/products/datasheets/MRC-1.pdf`, 01.04.2021.

[171] `http://fy.chalmers.se/~f96hajo/drasi/doc/`, 12.04.2021.

[172] `https://www.ortec-online.com/products/radiation-detectors/germanium-hpge-radiation-detectors/detector-stock-list`, 25.03.2021.

[173] Yu. Khazov, A. Rodionov, and F.G. Kondev. Nuclear data sheets for A = 133. *Nuclear Data Sheets*, 112(4):855–1113, 2011.

[174] Sanderson, C.G. Lyon, W.S. (Ed.). (1980). Comparison of Ge(Li) well and n-type coaxial detectors for low energy gamma-ray analysis of environmental samples. United States: Ann Arbor Science Publishers, Inc.

[175] B. Rosner and D. W. Mingay. Properties of intrinsic germanium detectors at low engergies by escape peak spectroscopy. *X-Ray Spectrometry*, 12(2):82–86, 1983.

[176] `http://www-ap.gsi.de/Thomas/ap_html_research/energy/index.php`, 30.03.2021.

[177] Prof. Dr. A. Surzhykov, TU Braunschweig, calculations performed in 2020.

[178] Thomas Rauscher and Friedrich-Karl Thielemann. Astrophysical Reaction Rates From Statistical Model Calculations. *Atomic Data and Nuclear Data Tables*, 75(1):1 – 351, 2000.

[179] R. Ferguson Z. Meisel K. Smith S. Warren A. Heger R. D. Hoffman T. Rauscher A. Sakharuk et al. R. H. Cyburt, A. M. Amthor. The jina reaclib database: Its recent updates and impact on Type-I x-ray bursts. *The Astrophysical Journal Supplement Series*, 189(1):240, 2010.

[180] T Rauscher, N Dauphas, I Dillmann, C Fröhlich, Zs Fülöp, and Gy Gyürky. Constraining the astrophysical origin of the p-nuclei through nuclear physics and meteoritic data. *Reports on Progress in Physics*, 76(6):066201, May 2013.

[181] Andrianov V. Aurand B. et al. Lestinsky, M. Physics book: CRYRING@ESR. *Eur. Phys. J. Spec. Top*, 225:797–882, 2016.

[182] Markus Steck and Yuri A. Litvinov. Heavy-ion storage rings and their use in precision experiments with highly charged ions. *Progress in Particle and Nuclear Physics*, 115:103811, 2020.

[183] C. Bruno. Low-energy studies for nuclear astrophysics (both above- and underground). *Journal of Physics: Conference Series*, 1643:012044, 12 2020.

[184] Technical Report For the Design, Construction and Commissioning of an In-ring Spectrometerfor Nuclear Reaction Studies at CRYRING (2018) https://fair-center.de/fileadmin/fair/experiments/APPA/documents/The_In-ring_Spectrometer_for_Nuclear_Reaction_Studies_at_CRYRING_-_UK_ISOL_WP2__31_January_2018__-_public.pdf.

[185] A. Henriques et al. Future Perspectives for Surrogate-Reaction Studies at Storage Rings. *Springer Proc. Phys.*, 254:209–215, 2021.

[186] A. Henriques et al. Indirect measurements of neutron cross-secti at heavy-ion storage rings. *J. Phys. Conf. Ser.*, 1668(1):012019, 2020.

Acknowledgements

First of all, I would like to thank Prof Dr. Yuri Litvinov as the leader of the ASTRUm group for giving me the opportunity to perform my PhD studies at GSI in association with the Heidelberg University. I am greatly proud of being a student at Heidelberg and hoping to increase the reputation of the university as its former student Baron Loránd Eötvös de Vásárosnamény, a great Hungarian physicist, did after who my university in Hungary was named. Furthermore, I would also like to highlight Yuri's key role in my professional development and his special support to gain recognition in the scientific community.

Also, I would like to acknowledge Dr. Jan Glorius for his supervising, insightful view on my research subject and straightforward opinions which helped me to progress both professionally and personally.

In addition, I would like to thank my co-supervisors, Prof. Dr. Wolfgang Quint and Prof. Dr. Klaus Blaum, who set me an excellent example as head scientists and never fail to motivate me with their kind words.

Also, I want to express my appreciation towards my previous supervisors, Dr. Eva Sicking and Dr. Ákos Horváth, for helping me to come to GSI and for their support along my path to reach the doctoral title.

I would like to emphasize my gratitude for the ESR and FSR teams, especially for Dr. Markus Steck, Dr. Helmut Weick and Dr. Sergey Litvinov, for their tireless efforts during the beam time period despite the extraordinarily difficult circumstances.

I would like to express my appreciation for the excellent company towards my closer colleagues as well, especially Dr. Rui Jiu Chen, Dr. Alexandre Gumberidze, Dr. Siegbert Hagmann, Dr. Pierre-Michel Hillenbrand, Dr. Michael Lestinsky, Dr. Nikos Petridis, Dr. Rodolfo Sánchez, Dr. Shahab Sanjari, Dr. Uwe Spillmann, Dr. Sergiy Trotsenko, Dr. Gleb Vorobyev, Dr. Yuan Ming Xing and the members of our PhD squad, Dmytro Dmytriev, Ivan Kulikov and Ragandeep Singh Sidhu. In particular, I raise my glass to my eastern friends, with whom I had many entertaining discussions and spent "zsír" times together.

Last but not least, I would like to thank my family for the lots of patience during the stressful periods and my fiancée Aida for her love and support. I feel blessed of having her being my significant other in life.
Z